# Optical anisotropy of conjugated polymer PEDPT:PSS and its effect on Photovoltaic performance of crystalline-Si/PEDOT:PSS heterojunction solar cells

# 導電性高分子 PEDOT:PSS の光学異方性と結晶 Si/PEDOT:PSS ヘテロ接合太陽電池性能

Qiming Liu

A Dissertation Presented to the Faculty

of Saitama University

in Candidacy for the Degree of Doctor of Engineering

Recommended for Acceptance by the

Department of Functional Material Science

Adviser: Hajime Shirai

January 2015

# Abstract

Solar cells based on the crystalline silicon offer high efficiency of 25.6% (latest achievement from Panasonic), but they are expensive due to the high temperatures required in their fabrication. The alternative approach using low-temperature processable organic photovoltaics (OPV) is potentially cheaper, but the organic solar cells are not very efficient. In our work, we explore if organic semiconductor can be integrated with silicon to form hybrid organic/silicon solar cells that are both efficient and low-cost. Specifically, we demonstrate that a solution-processed silicon/organic heterojunction (SOH) can replace the conventional silicon p-n junction to yield solar cells with high power conversion efficiencies (>12%).

As we known, to generate a photovoltaic in a solar cell, the photo generated carries need to be spatially separated at two electrodes of opposite polarity. In solar cells this is typically accomplished using a p-n junction. While the p-n junction technology is well understood, the fabrication of p-n junction on silicon is expensive process because it requires ultra-clean furnaces, pure precursors and high temperatures. In our work, we successfully replace the silicon p-n junction with a silicon/poly(3,4-ethylenedioxythiophene):poly(styrenesulfonate)

(PEDOT:PSS) heterojunction that can be manufactured at low temperatures (＜ 140℃) with a simple spin-coating process. The key design rules to achieve a high efficiency are discussed and experimentally demonstrated, as follows.

a). The uniform coating of PEDOT:PSS thin films on hydrophobic Si substrates

In this work, commercialized highly conductive ink (Clevios PH1000) was used as precursor to form transparent hole transport layers on n-type silicon by simple spin-coating process, and a big problem here is the uniform coating of aqueous solution on the hydrophobic H-terminated Si surface. We demonstrate the usage of 0.1wt% Zonyl fluorosurfactant (DuPont) as an additive into PEDOT:PSS improved the adhesion of precursor solution on hydrophobic c-Si wafer. The average power conversion efficiency value was 11.3%, which was superior to those of non-treated devices. The Zonyl-treated soluble PEDOT:PSS composite is promising as a hole-transporting transparent conducting layer for c-Si/organic heterojunction(SOH) photovoltaic applications.

b). Optical anisotropy in PEDOT:PSS and its effect on the photovoltaic performance of SOH solar cells

In this topic, we demonstrated the effect of uniaxial optical anisotropy on the photovoltaic performance of c-Si/organic heterojunction solar cells produced by spin coating using either a MeOH solvent or MeOH and EG

cosolvents. The systematic study of corresponding samples via spectroscopy ellipsometry implied that the use of the cosolvents led to an increase in extraordinary index of refraction and a reduction in the film thickness which promoted densification of polymer chains network in the resulted PEDOT:PSS thin films. And this improvement of PEDOT:PSS fine structure due to colsolvent addition resulted in an increased hole mobility from 1.23 $cm^2$/V.s to 3.92 $cm^2$/V.s of the resulted samples. A solar cell fabricated using such a film exhibited a relatively high efficiency of 11.23%, with a substantial fill-in factor (*FF*) value of 0.71.

c). Employment of guest materials for further improvement of SOH solar cells efficiencies

In addition, varieties of functional material like graphene oxide, molybdenum oxide flake sheet, ferroelectric polymer poly (vinylidene fluoride tetrafluoroethylene) P(VDF-TeFE) were employed as dopant to improve carrier transport properties in SOH diodes and go advantage the solar cell performance.

d). The photovoltaic performance of PEDOT:PSS/n-type poly-Si heterojucntion solar cell devices have been investigated. The high pressure $H_2O$ vapor treatment of poly-Si prior to the film deposition of organic promoted the reduction of dangling bond defects incorporated into poly-Si, resulting in the enhanced carrier collection efficiency at 850-1100 nm region. The chemical mist deposition of conductive

PEDOT:PSS combined with negative DC bias supply improved significantly the adhesion of PEDOT:PSS on hydrophilic poly-Si wafer. As a consequence, a highly efficient PEDOT:PSS/poly-Si heterojunction solar cell was obtained with the highest power conversion efficiency of 9.8% with a $J_{sc}$ of 33 mA/cm$^2$, a $V_{oc}$ of 0.54 V, and a *FF* of 0.55. Such organic/poly-Si heterojunction cells can potentially further deliver high FF and conversion efficiency combining with the creation of ohmic junction at the rear surface.

Finally we highlight the possible candidate approach which give a pathway for further improving the efficiency of c-Si/PEDOT:PSS hybrid solar cells.

# Acknowledgements

First, I would like to thank my supervisor, Professor. Hajime Shirai, for his guidance and kindly help. I am especially thankful for his encouragement, supervision and patience, without which I could not had overcame the countless paper revisions, days of fruitless hard work and moments of thinking to abandon the topics. I am also very thankful to Professor Norihiko Kamata, Masamichi Sakai, Keiji Ueno and Kenji Kamishima for taking the time to read this thesis and provide valuable comments. I am also very thankful to above professors for the many fruitful discussions we have shared over the last few years.

I have to also acknowledge the generosity of all the funding agencies. This research was partially supported by a Japan Science and Technology (JST) Agency (A-step) grant and a Grantin-Aid for Scientific Research from the Ministry of Education, Culture, Sports, Science, and Technology(MEXT) of Japan. And also I give my great thanks to MEXT for their sufficient support with MEXT Scholarship to me for my PhD Program in Saitama University.

And a special thanks to all members in Shirai group. First I must thank the senior members, Dr. Zeguo Tang, Wei Wang who helped me to spend my transition period in my beginning days in Japan. I also commend Mr.

Takashi Imamura, Ishwor Khatri, Masahiro Ono, Tomohisa Ino, Taiga Hiate, Hideto Koshino, Fumiya Watanabe, Naoto Miyauchi, Kyohei Watanabe, Kyohei Ishikawa, Tatsuya. Ohki, Hiroyuki Sugawara and Mrs. Ayo Hoshino, for their excellent camaraderie and cooperation. In the wider Department community, I shall show my thanks to members from Ueno Group for their very kindness help.

My gratitude also goes to the staffs in the Department of Functional Material Science who work tirelessly in the background. I am especially indebted to Dr. Ryo Ishikawa and Dr. Ishwor Khatri for always giving the excellent advises to me, and also their fruitful discussion. Ms. Hisayama Mr. Saito and Mr. Koken, I thank you all for your helpful technician and secretary work during my researching and studying in Saitama University. Finally, a special note of thanks to all the office staffs in Saitama University - There never were trouble or disturb during our conductance while maintaining an infectious smile.

At last, I want to thank my family. First, very much thanks for my parents. They have always supported me, cared for me, and have never shied away from showing their own happiness for my even tiny achievement and infinity warm for my sorts of false. Dear my Mom and Father, this is to you. My older brother, Qisheng, has always overlooked my failings and has been there for me. He keeps me honest and grounded, and for that I am eternally grateful. I was fortunate to grow up in a large

and very loving family and a lot of my character has been molded by my aunts and uncles. Finally, I shall express my gratitude to my grandparents. For all practical purposes, I was raised by my grandparents and I can honestly say that no one shall ever love me as unconditionally they do. In all my academic pursuits, including the PhD, I have been following in the route of my grandparents. They were my most important teachers.

To my grandparents

# Contents

## List of Tables

## List of Figures

co-solvent modified PEDOT:PSS films.

2.7 Conductivity of PEDOT:PSS films fabricated by spincoat using either MeOH, EG alone, or MeOH and EG as co-solvents measured for four different ~100nm thick samples. The results for pristine PEDOT:PSS are also shown as a reference.

2.8 *J-V* curves for c-Si/PEDOT:PSS hybrid solar cells with pristine, MeOH-modified, and co-solvent modified PEDOT:PSS buffer layers (a) in the dark and (b) under simulated AM1.5G illumination. (c) EQE spectra for the corresponding c-Si hybrid solar cells.

3.1 SEM images (a)~(c) and EDX maps (d)~(f) (corresponding to the circled region in Fig 3.1(a)) of $MoO_3$ particle in PEDOT:PSS. Inset illustrates schematics for the possible intercalation of PSS chains into layered $MoO_3$, where red and gray spheres denote O and Mo atoms, respectively; (d)~(f) are EDX maps for Mo, O and S. respectively, in $MoO_3$ doped PEDOT:PSS.

3.2 PL and PLE spectra of $MoO_3$ doped PEDOT:PSS film. The optical micrographs of PEDOT:PSS with and without 10wt.% $MoO_3$ doping are shown as well.

3.3 (a) $J_d$-$V$ and (b) $J_p$-$V$ curves for c-Si/PEDOT:PSS:$MoO_3$ composite hybrid solar cells with different $MoO_3$ concentrations. Inset shows schematic of the device structure of c-Si/PEDOT:PSS: $MoO_3$ composite

solar cells. (c) EQE and (d) DEQE spectra for corresponding c-Si/PEDOT:PSS:$MoO_3$ composite hybrid solar cells. DEQE values are relative to that of a pristine device.

3.4 Reflectance spectra for c-Si/PEDOT:PSS:$MoO_3$ composite solar cells with different $MoO_3$ doping concentrations. All PEDOT:PSS:$MoO_3$ layer thickness were ~100nm

3.5 Device schematic and the molecular structure of PEDOT:PSS and P(VDF-TeFE) ferroelectric polymer

3.6 (a) XRD patter and (b) FTIR spectra of a 100nm thick P(VDF-TeFE) layer in three states: as-grown, annealed at 140℃ for 30min, annealed and poling under a reverse DC bias of $5*10^4$k*V*/cm for 30min. The spectra are shown as a different spectra referred to those of as-grown and the annealed states. (c) Plane and cross-sectional SEM images of a 3nm thick P(VDF-TeFE) later after thermal annealing at 140℃ for 30min.

3.7 J-V curves in the dark and under exposure of AM1.5G simulated solar light for as-deposited c-Si/FE/PEDOT:PSS diodes with different FE layer thicknesses.

3.8 (a) J-V curves in the dark and under exposure of AM1.5G simulated solar light for c-Si/FE(3nm thick)/PEDOT:PSS diodes after poling of the FE layer under a reverse DC bias of $5*10^4$ k*V*/cm for different periods. The inset shows the poling conditions. (b) *J-V* curves for the corresponding device after poling under a forward DC bias of $2*10^3$

k*V*/cm for different periods. (c) photo *J-V* curves for a pristine device without an inserted FE layer under a reverse DC bias of $5*10^4$ k*V*/cm for different periods.

3.9 (a) Capacitance hysteresis loop of c-Si/FE/PEDOT:PSS junction solar cell with a 3nm thick FE layer measured at 1MHz for different poling periods. (b) A schematic of the remanent polarization of FE dot array at the c-Si/PEDOT:PSS interface.

4.1 Schematic of the PEDOT:PSS/poly-Si heterojunction solar cells. Inset shows the SEM image of 100-nm-thick CMD PEDOT:PSS on poly-Si. Scale bar in the inset is 1μm

4.2 Schematic of the conversional CMD setup

4.3 shows FTIR spectra of poly-Si wafer after high-pressure $H_2O$ vapor treatment and subsequent 5% HF treatment

4.4 $1/C^2$-V plot at 1 MHz (top) and *C-f* (*f*: measurement frequency) characteristics of Ag(1mmΦ)/PEDOT:PSS/poly-Si diode using spin-coated and CMD, respectively

4.5 The 2D-dimensional map within $2\times2$ $cm^2$ area of (a) short-circuit current density $J_{sc}$ and (b) external quantum efficiency EQE at 950 nm of corresponding PEDOT:PSS/poly-Si heterojunction solar cells

4.6 Optical micrograph and 2D Raman map combination of (a) spin-coated and (b) CMD deposited PEDOT:PSS films on high-pressure

# Chapter 1

# Introduction

## 1.1 Motivation

As is it well known, there is an emerging need to reduce human energy consumption dependence on non-renewable fuels and shift to renewable energy. Among them, Solar photovoltaic (PV) devices, are very a promising candidate to convert solar energy into electricity. Thus, PV industry increased markedly in recent decades. Nevertheless, as of 2012, solar PV accounted is still not sufficient in the total human energy consumption [1]. The most important reason for the low energy consumption share is high costs of typical PV productions. Compared to conventional power sources, PV-generated electricity is expensive, mostly due to the high costs of manufacturing and installing solar modules.

Among the PV market, there are many kinds of technologies which show different price and performance. To allow absolute comparison between the competing PV technologies, PV panels are quoted in terms of “U.S dollar per watt-peak” ($/Wp). This ratio takes into account that one needs fewer numbers of more efficient modules to generate the same

amount of total power. “Watt-peak” simply refers to the fact that, solar panels are rated for power produced at the peak light intensity, even though the actual power output varies during the day.

Table 1.1: Cost estimate of various components of a photovoltaic module in 2010 (without cell and module manufacturer's margin) [2]

| Component | Cost ($/Wp) |
|---|---|
| **Silicon** | **0.54** |
| Raw materials (Si feedstock, saw slurry, saw wire) | 0.36 |
| Utilities, maintainance, labor | 0.04 |
| Equipment, tooling, building, cost of capital | 0.06 |
| Margin | 0.08 |
| **Cell** | **0.26** |
| Raw materials (eg. metallization, SiNx, dopants, chemicals) | 0.18 |
| Utilities, maintainence, labor | 0.04 |
| Equipment, tooling, building, cost of capital | 0.04 |
| **Module** | **0.36** |
| Raw materials (eg. Glass, EVA, metal frame, j-box) | 0.26 |
| Utilities, maintainence, labor | 0.01 |
| Equipment, tooling, building, cost of capital | 0.01 |
| Shipping | 0.08 |
| **Total** | **1.16** |

Crystalline silicon solar cell is the dominant technology with 80% of the PV market share. Silicon cells are efficient (13-20 % average efficiencies in case of modules), but they are still little expensive. As of 2010, average manufacturing costs of silicon-based PV modules were 1.16 $/Wp [2], not only because crystalline silicon wafer is expensive, but also because fabrication process of an efficient cell requires several high-temperature steps, complicated equipments, and expensive materials [3, 4, 5] (Table 1.1). [6].

In order to improve PV energy installation, the key point is reduction of solar cell cost, like compromise on efficiency and use cheaper

materials: easier-fabricated thin-film semiconductors instead of more expensive crystalline Si. The lower raw material costs, low-temperature processing, simpler capital equipments, and higher throughput manufacturing allow these “thin-film” technologies to achieve substantial reductions in cost. Among them, composite semiconductor like Cadmium Telluride (CdTe), Cooper Indium Gallium Selenide (CIGS) and amorphous-Si (a-Si) technologies are prominent examples (Fig. 1.1).

Another approach is organic solar cells. Organic molecules with conjugated π-electron systems are also a class of thin-film semiconductors. Different with typical valence and conduction bands in inorganic materials, they have intra-molecular filled and empty energy levels, referred to as the highest-occupied-molecular-orbital (HOMO) and lowest-unoccupied-molecular-orbital (LUMO), respectively [7]. The energy gap of organic materials, both donors and acceptors, are typically ~2-3 eV, which is larger than that of crystalline silicon (1.12 eV). The clear advantage with organic materials is their manufacture process - organic thin-films can be deposited using low-cost methods, such as spin-coating, spray-coating or transfer printing [8]. Due to the cost advantages, many types of organic-based solar cells have been proposed [9]. However efficiency of these devices is still poor [6] and their reliability is also a problem [10, 11].

## 1.2 Silicon-based Hybrid Solar Cells

In this work, a hybrid approach is demonstrated, where organic polymers are combined with silicon wafer to yield a silicon/organic diode which shows the cost improvement of thin-film organic materials and outstanding performance of silicon [12, 13, 14].

Like organic solar cells, this hybrid devices use only low-temperature (<140℃) processing and are very simple to fabricate - an organic semiconductor is spin-coated or mist deposited on top of crystalline silicon substrates, followed by electrode fabrication. Another advantage of hybrid devices is the possibility of higher throughput – unlike dopant diffusion which is a slow step, organic solutions can be deposited on silicon at very high rates.

In this Si-based solar cell, similar as traditional Si solar cells, light absorption and photocurrent in hybrid devices generated predominately in silicon, so losses of light absorption and photogenerated carrier recombination are relative low. Theoretically, very high efficiencies, rivaling crystalline silicon solar cells, can be achieved in such hybrid photovoltaic devices.

## 1.3 Solar Cells: Principles and Fundaments

Generally, solar cells are diodes that have been optimized for absorbing light while generating low dark-current. Like a typical diode, there is a built-in electric field inside a solar cell which allows current to flow in only forward-bias. In the dark, the current-voltage characteristics are similar to that of a diode: low leakage in the reverse-bias and an exponential turn-on in the forward bias. The current density ($J$) depends on the voltage across the device ($V$) as

$$J(V) = J_0 \left(e^{qV/nkT} - 1\right) \qquad (1.1)$$

where $k$ is the Boltzmann constant, $T$ is the temperature, $n$ is the ideality factor, and $J_0$ is the saturation current density of the diode. In the case of low-level minority carrier injection and dominance of the Shockley-Read-Hall recombination, $n$ is unity, and $J_0$ is given by

$$J_0 = q\frac{D_p}{L_p}\frac{n_i^2}{N_D} + q\frac{D_n}{L_n}\frac{n_i^2}{N_A} \qquad (1.2)$$

$n_i$ is the intrinsic carrier density, $N_D$ and $N_A$ are the doping concentrations in the n- and p-type regions, $D_n$ and $D_h$ are diffusion coefficients of electrons and holes in silicon, and $L_n$ and $L_h$ are the diffusion lengths of minority carriers. This equation assumes the long-base approximation is valid.

Under illumination, photons get absorbed in silicon, generating electron and hole pairs. The built-in electric field separates these charges

and forces them towards opposing electrodes, causing a photocurrent (*JL*). The current voltage characteristics in this case are given by

$$J(V) = J_0\left(e^{qV/nkT} - 1\right) - J_L$$
$$P_{generated}(V) = \left(J_0\left(e^{qV/nkT} - 1\right) - J_L\right)V \qquad (1.3)$$

The generated power (*P*), given by the product of voltage and current (negative values represent generated power), has a global maximum, called the peak power point. To extract maximum energy from a solar cell, it should be biased near the peak power point.

The performance of solar cells is typically measured in terms of three figures of merit: the short-circuit current ($J_{SC}$), the open-circuit voltage ($V_{OC}$), and the fill in factor (*FF*). For the case when the series resistance ($R_s$) is zero, Eq.(1.3) gives

$$J_{SC} = J_L$$
$$V_{OC} = \frac{nkT}{q} ln\left(\frac{J_{SC}}{J_0} + 1\right)$$
$$FF = \frac{P_{max}}{V_{OC}J_{SC}}$$
$$\eta = \frac{V_{OC}J_{SC}FF}{P_{in}} \qquad (1.4)$$

where $\eta$ is the power conversion efficiency. The peak power output is generated at some intermediate point between $J_{SC}$ and $V_{OC}$.

## 1.4 Efficiency of Silicon Solar Cells

To increase the efficiency of a solar cell, enhancement of either $J_{SC}$, $V_{OC}$, or $FF$, needs to be achieved. The record efficiencies published in the literature of various solar cell technologies are given in Table 1.2 [6]. To better compare the different technologies the implied $J_0$ of the diodes, calculated from the solar cell parameters using Eq. (1.4), is also shown.

### 1.4.1 Short-Circuit Current

In case of constant generation across the whole depth of a solar cell, the $J_{SC}$ is given by

$$J_{SC} = qG(L_n + L_p) \qquad (1.5)$$

where $G$ is the generation rate due to illumination and $L_p$ and $L_n$ are the hole and electron diffusion lengths, respectively. The relation assumes that the depletion width in both *n* and *p* regions is much less than the diffusion lengths, $L_p$ and $L_n$. The relation also doesn't consider the effect of surface recombination. For a solar cell in which the diffusion lengths are longer than the wafer thickness ($L_p$, $L_n$ >W), the diffusion term drops off and the short-circuit current depends only on the photon-flux of the incident light.

Table 1.2: Performance of different solar cell technologies at AM1.5 conditions [6]. Reported values of solar cell parameters: Efficiency ($\eta$), $V_{OC}$, $J_{SC}$ and FF. Implied value of $J_0$ was calculated using Eq. (1.4).

| Cell Type | $\eta$ (%) | $V_{OC}$ (V) | $J_{SC}$ (mA/cm$^2$) | FF (%) | Area (cm$^2$) | $J_0$[a] (A/cm$^2$) |
|---|---|---|---|---|---|---|
| Single-crystalline Si | 25.0±0.5 | 0.706 | 42.7 | 82.8 | 4.00 | $6.9\times10^{-14}$ |
| HIT (c-Si/a-Si) | 23.0±0.6 | 0.729 | 39.6 | 80.0 | 155.1 | $2.6\times10^{-14}$ |
| Multi-crystalline Si | 20.4±0.5 | 0.664 | 38.0 | 80.9 | 1.002 | $3.1\times10^{-13}$ |
| Thin film transfer Si | 16.7±0.4 | 0.645 | 33.0 | 78.2 | 4.017 | $5.6\times10^{-13}$ |
| Amorphous Si | 10.1±0.3 | 0.886 | 16.75 | 67.0 | 1.036 | $2.6\times10^{-17}$ [b] |
| Single-crystalline GaAs | 27.6±0.8 | 1.107 | 29.6 | 84.1 | 0.9989 | $9.6\times10^{-21}$ |
| CIGS | 19.6±0.6 | 0.713 | 34.8 | 79.2 | 0.996 | $4.3\times10^{-14}$ |
| CdTe | 16.7±0.5 | 0.845 | 26.1 | 75.5 | 1.038 | $2.0\times10^{-16}$ |
| Organic | 8.3±0.3 | 0.816 | 14.46 | 70.2 | 1.031 | $3.4\times10^{-16}$ [b] |

[a] Extracted from given parameters using Eq. (1.4)
[b] Due to low FF, extracted value is inaccurate.

Solar insolation spectrum closely matches the broadband spectrum of a 5777°K blackbody [15], but due to atmospheric absorption, the actual spectrum reaching earth is strongly confined between the far infrared and near ultraviolet. Solar cell efficiencies are normally quoted against the ASTM AM 1.5G standard illumination [16]. The incident power at AM 1.5G illumination is 100 mW/cm$^2$.

A semiconductor with a certain bandgap ($E_G$) extensively absorbs photons with energies greater or equal to EG. Some phonon-mediated absorption does occur at lower energies but the absorption lengths are very long (around 1mm in case of silicon) that not many carriers are generated by this process in a 200-500 μm thick silicon wafer. Assuming each photon generates an electron-hole pair, i.e. an internal quantum efficiency of 1, the maximum possible photocurrent at a given wavelength cutoff could be calculated. In case of silicon, which has a

bandgap of 1.12eV, only wavelengths below ~1110nm could be absorbed and the theoretically maximum photocurrent is 43.8mA/cm$^2$ [17]. Actually crystalline solar cells reach very close to this value ($J_{SC}$ > 42mA/cm$^2$) by clever use of light-trapping structures and anti-reflection coatings [18].

### 1.4.2 Fill-Factor

Fill factors decrease with increase in the internal series resistance. Usually, the top metal grid covers only ~10% of the top surface, so photogenerated carriers need to travel large lateral distances before they are collected at the metal contact, in case of these carries fortunately had not been recombinated among diode interfaces. If the conduct of the top semiconductor layer is not high enough, the resulted ohmic contact reduce the fill-factor [19].

Table 1.3: Ideality factors ($n$) resulting from different recombination mechanisms that may have been observed in solar cells.

| Recombination Type | $n$ | Description |
|---|---|---|
| SRH in quasi-neutral region (low-level injection) | 1 | Minority carrier limited. |
| Band to band (low-level injection) | 1 | Minority carrier limited. |
| SRH in quasi-neutral region (high-level injection) | 2 | Both carriers needed. |
| Band to band (high-level injection) | 2 | Both carriers needed. |
| SRH in depletion region | 2 | Both carriers needed. |
| Auger | $\frac{2}{3}$ | Two majority and one minority carriers needed. |

Fill factors also reduce if the ideality factor (n) of the solar cells

increases. The ideal diode-characteristics (Eq. (1.1)) assume that current flows only due to low-level minority-carrier injection (into quasi-neutral regions) and carrier recombination only via the Shockley-Read-Hall (SRH) mechanism [20]. In a practical cell, current can be caused by several other mechanisms (Table 1.3), e.g high-level minority carrier injection ($n$=2) [21], Auger recombination ($n$=2/3) [22], recombination in the depletion region of the diode ($n$=2) [23, 24]. Non-uniformity in the doped layers is also reported to cause higher ideality factors [25]. Current contribution of these non-ideal processes has different voltage dependence than the ideal case of Eq. (1.1) and consequently ideality factors of real devices is different from unity.

Both increased ideality and higher fill in factors can be a big problem in typical thin-film devices, because the mobilities and diffusion lengths of carriers in amorphous materials are usually poor. However, in the case of high-quality crystalline silicon solar cells fill-factors that are very close to the theoretical maximum (>80 %) could be easily obtained.

### 1.4.3 Open-Circuit Voltage

Since $J_{SC}$ and $FF$ are already near the theoretical maximum in practical silicon solar cells, at this stage, the only parameter available for further improvement is $V_{OC}$. Enhancements in $V_{OC}$ need a reduction in $J_0$

(according to Eq. (1.4)).To understand the intuitive reasoning behind the relationship between $J_0$ and $V_{OC}$, we have to first understand the physical meaning what $J_0$ represents.

Theoretically, $J_0$ of the device depends on the minority carrier diffusion lengths and bulk doping as presented in Eq. (1.2) [20]. At equilibrium state, the diffusion current (due to carrier density gradient) equals the drift current (due to the built-in field), and the total current is zero. When a forward-bias is externally applied across the *p*-*n* junction the built-in field id suppressed, breaking the drift-diffusion balance. The more dominant diffusion current injects minority-carriers through the junction into the quasi-neutral region, where they recombine. Holes are injected from p-type Si to n-type Si, electrons are injected from n-type Si to p-type Si, resulting in a positive current flow from anode to cathode. The higher the injected minority-carrier current, the higher $J_0$ could be observed. So $J_0$ is simply a symbol of minority carrier recombination in the diodes.

In case of under illumination, excess carriers are created in the quasi-neutral regions of silicon due to photogeneration. The built-in field demands to maintain establish equilibrium by forcing out the photogenerated carriers, electrons towards the cathode and holes towards the anode, thereby results in a photocurrent with the direction opposite to the minority carrier current and a positive photovoltage. However, due to

a positive photovoltage and resulted reduction in built-in field, some of the minority carriers can't cross the potential, they are injected across the junction and lose to recombination. The amount of current lose to recombination is precisely the value of the dark-current at that voltage. By decreasing $J_0$, we can reduce the amount of carriers lose to recombination, and thus a lower $J_0$ should lead to a higher $V_{OC}$.

## 1.5 Outline

In this work, hybrid silicon/organic heterojunctions (SOH) are investigated for photovoltaic applications. The goal in this topic was to integrate low-cost organic semiconductors on high-performance crystalline silicon to demonstrate low-cost high-performance solar cells.

In chapter 2, modification of conductive PEDOT:PSS was been exhibited via flurosurfactant addition and co-solvent treatment. At first, we demonstrate the usage of 0.1wt% Zonyl fluorosurfactant (DuPont) as an additive into PEDOT:PSS improved the adhesion of precursor solution on hydrophobic c-Si wafer. The average power conversion efficiency value was 11.3%, which was superior to those of non-treated devices. The Zonyl-treated soluble PEDOT:PSS composite is promising as a hole-transporting transparent conducting layer for c-Si/organic heterojunction(SOH) photovoltaic applications. Next, optical anisotropy

in PEDOT:PSS and its effect on the photovoltaic performance of SOH solar cells. In this topic, we demonstrated the effect of uniaxial optical anisotropy on the photovoltaic performance of c-Si/organic heterojunction solar cells produced by spin coating using either a MeOH solvent or MeOH and EG cosolvents. The systematic study of corresponding samples via spectroscopy ellipsometry implied that the use of the co-solvents led to an increase in extraordinary index of refraction and a reduction in the film thickness which promoted densification of polymer chains network in the resulted PEDOT:PSS thin films. And this improvement of PEDOT:PSS fine structure due to co-solvent addition resulted in an increased hole mobility from 1.23 $cm^2$/V.s to 3.92 $cm^2$/V.s of the resulted samples. A solar cell fabricated using such a film exhibited a relatively high efficiency of 11.23%, with a substantial fill-in factor (FF) value of 0.71.

In chapter 3, employment of guest materials, like molybdenum oxide flake sheet ($MoO_3$), ferroelectric polymer poly(vinylidene fluoridetetrafluoroethylene) P(VDF-TeFE), for further improvement of SOH solar cells efficiencies have been shown. In this work, molybdenum oxide flake sheet, ferroelectric polymer poly(vinylidene fluoridetetrafluoroethylene) P(VDF-TeFE) were employed as dopant to improve carrier transport properties in SOH diodes and go advantage the solar cell performance.

In chapter 4, the photovoltaic performance of PEDOT:PSS/n-type poly-Si heterojucntion solar cell devices have been investigated. The high pressure $H_2O$ vapor treatment of poly-Si prior to the film deposition of organic promoted the reduction of dangling bond defects incorporated into poly-Si, resulting in the enhanced carrier collection efficiency at 850-1100 nm region. The chemical mist deposition of conductive PEDOT:PSS combined with negative DC bias supply improved significantly the adhesion of PEDOT:PSS on hydrophilic poly-Si wafer. As a consequence, a highly efficient PEDOT:PSS/poly-Si heterojunction solar cell was obtained with the highest power conversion efficiency of 9.8% with a $J_{sc}$ of 33 mA/cm$^2$, a $V_{oc}$ of 0.54 V, and a *FF* of 0.55.

In chapter 5, a summary of all the results and some ideas for future work are presented.

# Chapter 2

# Silicon/PEDOT:PSS Heterojunctions Solar Cells with Modified Fine Structure of PEDOT:PSS

## 2.1 Introduction

To date, crystalline silicon (c-Si) based heterojunction solar cells with an intrinsic hydrogenated amorphous silicon (a-Si:H) thin layers (HIT), Ntype (n-) c-Si/i-a-Si:H/p-a-Si:H/ITO multilayered structure offer high efficiency with an efficiency of 22~23% [26-28]. The a-Si:H layers, in general, is fabricated by a low-pressure plasma-enhanced chemical vapor deposition (PE-CVD) of a $SiH_4$ and $H_2$ mixture. Indium tin oxide (ITO) films as the transparent conductive oxide (TCO) layer are also prepared by low-pressure rf magnetron sputtering. As an alternate approach using c-Si/organic heterojunction solar cells is potentially cheaper due to low-temperature processing. To date, n-Si/poly-$(CH_3)_3$Sicyclooctate -traaniline, n-Si/polyaniline, and p-Si/4-tricyanovinyl-N,N-diethylaniline have been investigated and shown up to 3.5% [29-31]. Several approaches have been also attempted to improve the device performance

with carbon nanotubes (CNTs) and Si nanowires (SNWs) to increase the conductivity of polymer [32, 33]. J. C. Strum et al. has reported an improved efficiency of 10.1% in planer n-Si/poly(3-hexylthiophene-2,5-dily) (P3HT) junction solar cells [34]. More recently, relatively high efficiency c-Si/poly(ethylene dioxythiophene):poly(styrenesulfonate) (PEDOT:PSS) junction solar cells with a η of 10-11% have been reported [35, 36]. PEDOT:PSS is well known as a hole transport layer of organic thin-film solar cells (OSCs). It is also used as a transparent conductive layer by secondary doping of inert solvents such as glycerol, sorbitol, dimethyl sulfoxide (DMSO), N,N'-dimethyl formamide (DMF), tetrahydrofuran (THF), and graphene oxide (GO) [37-41].

Here, we demonstrate a solution-processed organic/silicon heterojunction can replace the conventional silicon p-n junction to yield solar cells with high power conversion efficiencies (over 10%).

As the schematic diagram of the conversional SOH device shown in Fig2.1, conjugated polymer Poly(3,4-ethylenedioxythiophene) poly(styrenesulfonate) (PEDOT:PSS) thin film plays an important role both in transparent conductive layer and emmiter layer to yield a typical photovoltaic junction . It is well known PEDOT:PSS is a polymer mixture of two ionomers. One component in this mixture is made up of sodium polystyrene sulfonate which is a sulfonated polystyrene. Part of

the sulfonyl groups are deprotonated and carry a negative charge. The other component PEDOT is a conjugated polymer and carries positive charges and is based on polythiophene. The properties of this polymer, like conductivity, transparence and mobility, are mainly determined by the component ratio and phase separation of PEDOT/PSS polymer chains. Thus, the fine structure modification of PEDOT:PSS polymer also plays an key factor for high efficiency c-Si/PEDOT:PSS hybrid solar cell devices. Here as following, several approaches of fine structure modification of conductive PEDOT:PSS are been presented.

## 2.2 Highly efficient SOH device with Zonyl fluorosurfactant treatment

As mentioned above, the alternate spin coating was attempted to improve the film uniformity on hydrophobic c-Si(100) wafer. But these products were still inhomogeneous frequently. The usage of the electrospray deposition (ESD) made possible the uniform coating, although the film deposition rate was very slow of 0.2 nm/s. [29] Simple coating technique with high film uniformity, therefore, is strongly required on hydrophobic c-Si wafer. Recently, Vosgueritchian et al. revealed that the Zonly fluorosurfactant-treated PEDOT:PSS film showed lower sheet resistance compared to untreated films, and it is a possible

material for indium tin oxide (ITO)-free organic photovoltaics as stretchable and flexible transparent electrodes. [30, 31] These findings will be also expected for the uniform spin coating of PEDOT:PSS on hydrophobic c-Si wafer without any complicate processes.

In this session, we demonstrate the highly efficient c-Si/Zonyl-treated PEDOT:PSS heterojunction solar cells showing a high efficiency of 10%–11%.

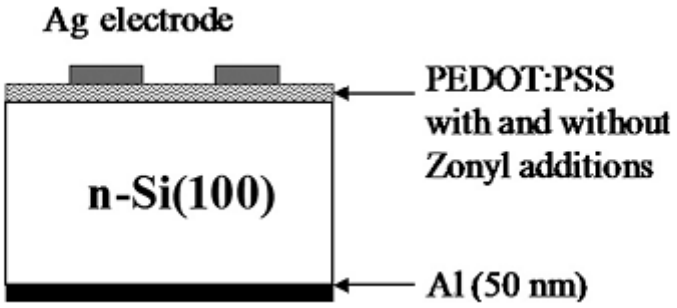


FIG 2.1 Schematic of c-Si/PEDOT:PSS hybrid photovoltaic device

Figure 2.1 shows the schematic of the c-Si/PEDOT:PSS hybrid solar cells. One-side-polished with N-type CZ Si(100) with resistivity of 3–5Ω.cm and thickness of 300 μm was used as a substrate. The c-Si wafers were cleaned in acetone, ethanol, and deionized water for 10min each. Following that they were dipped in 5% hydrofluoric (HF) acid to remove any native oxide. Highly conductive 5% by weight dimethyl sulfoxide (DMSO) added PEDOT:PSS (Clevios PH1000) mixed with different amounts of Zonyl fluorosurfactant was then spin coated onto the RCA H-terminated c-Si wafer with 1000rpm for 60s followed by thermal

annealing at 140℃ for 30min. Finally, the top ring electrode (5mm *5mm in inner size, 0.1mm width) was formed using silver paste by pattern printer. The outer area of the silver electrode was covered with an opaque mask to eliminate the incident light. The silver electrode has resulted in a power loss of 5%–7% of the incident light due to shadowing.

The PEDOT:PSS composite films were characterized by atomic force microscopy (AFM; Seiko Instruments SPA-300/SPI-3800), spectroscopic ellipsometry (SE), current density-voltage (J-V) in the dark and under illumination of AM1.5G, 100mW/cm$^2$ simulated solar light (Bunkoukeiki CEP-25BX), and capacitance-voltage (C-V) measurements.

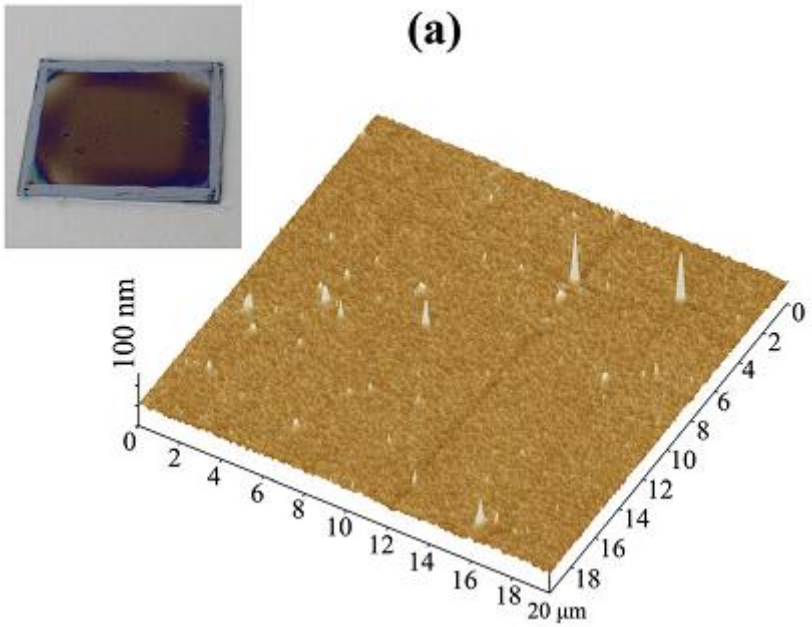

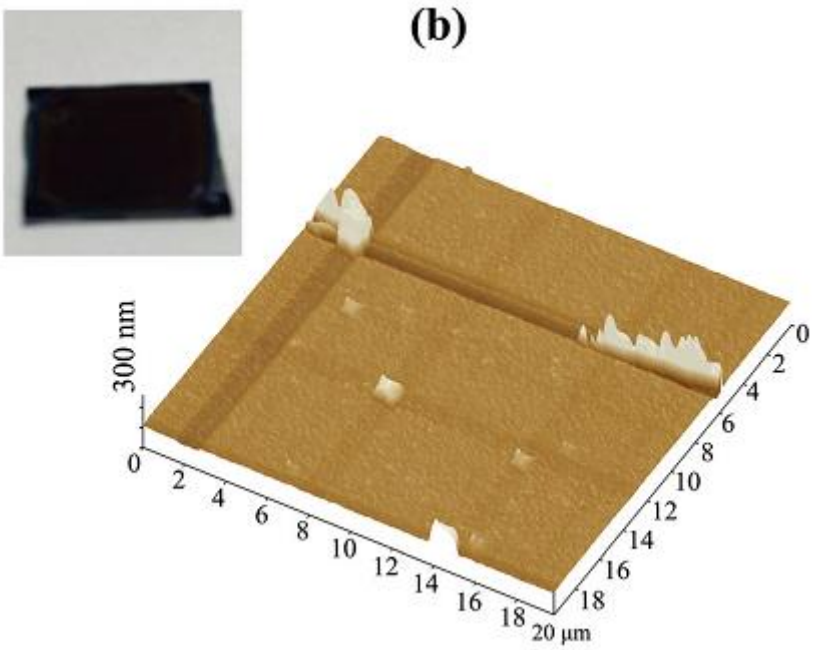


FIG 2.2 AFM and photo images of (a) pristine and (b) 0.1% Zonyl added PEDOT:PSS thin films on c-Si wafer. The former was for the alternate spincoat with 1000 and 2000rpm after dropping few shots of pristine PEDOT:PSS solution. The latter was prepared by spincoat with 1000rpm for 60s and subsequent dry at 140℃ for 30min. Both film thickness were around 100nm.

In Figure 2.2, the AFM and photo images of 100 nm-thick PEDOT:PSS films on flat c-Si(100) wafer are shown with and without adding a 0.1% Zonyl fluorosurfactant. The former was prepared by alternate spin coating with 1000 and 2000rpm after dropping few shots of pure PEDOT:PSS solution to improve the film uniformity rather than the single spin coating. The latter was prepared by the spin coating with 1000rpm for 60s and subsequent dry at 140℃ for 30min. Both film

thicknesses were around 100nm. It is clear that the surface uniformity of spin-coated PEDOT:PSS composite is improved markedly despite of the 0.1% Zonyl addition. The root-mean-square roughness (RMS) values were 2.6 and 3.3nm for the films with and without a 0.1% Zonly addition, respectively, in the 20*20 $\mu m^2$ area.

Figure 2.3 shows the J-V characteristics in the dark and under illumination of AM1.5G 100mW/$cm^2$ simulated solar light, and external quantum efficiency (EQE) spectra for the PEDOT:PSS/c-Si hybrid devices with and without a 0.1% Zonyl addition. The photovoltaic parameters, i.e., open circuit voltage $V_{oc}$, short circuit current density $J_{sc}$, an fill factor *FF*, and η, are summarized for the devices with different Zonyl weight percents in Table 2.1. It is seen that dark current density $J_d$ is suppressed significantly for the 0.1% Zonyl added device [Fig. 2.3(a)].

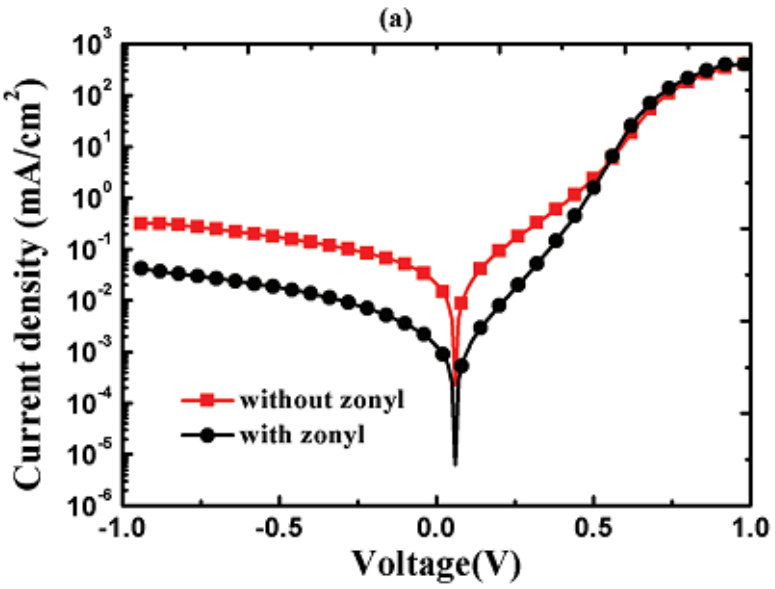

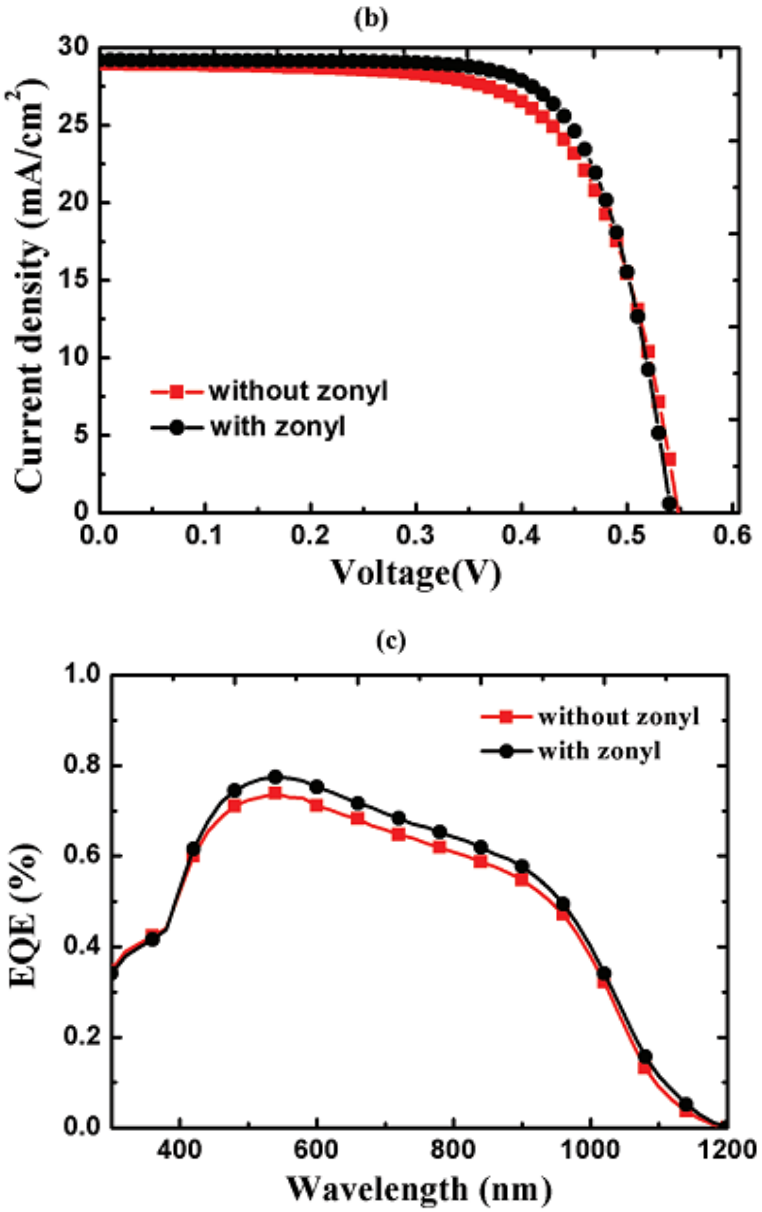


FIG 2.3 *J-V* curves of c-Si hybrid solar cells for PEDOT:PSS composite buffer layers with and without an addition of a 0.1% Zonyl fluorosurfactant (a) in the dark and (b) under illumination of a simulated AM 1.5G 100mW/cm$^2$ light. (c) EQE spectra of corresponding c-Si hybrid solar cells.

The calculated series resistance Rs showed a minimum of 0.75 Ω*cm$^2$

with a highest shunt resistance Rsh of $1.2*10^4$ Ω*$cm^2$ for the 0.1% Zonyl added PEDOT:PSS diode. The reduction in the dark current is clear evidence for reduced electron current and the suppression of electron recombination.

| Zonly concentrations | $J_{sc}$ (mA/$cm^2$) | $V_{oc}$ (V) | *F.F.* | Eff (%) | $R_s$ (Ω $cm^2$) |
|---|---|---|---|---|---|
| Pristine | 29.02 | 0.527 | 0.669 | 10.23 | 0.99 |
| 0.1% | 29.20 | 0.541 | 0.718 | 11.34 | 0.75 |
| 0.5% | 31.10 | 0.550 | 0.631 | 10.80 | 1.46 |
| 1% | 30.10 | 0.539 | 0.545 | 8.85 | 3.89 |
| 10% | 3.65 | 0.235 | 0.162 | 0.148 | 8.54 |

TABLE 2.1 Performance detail of the c-Si/PEDOT:PSS hybrid solar cells with different Zonyl concentrations.

These imply that the junction property is improved by the 0.1% Zonly treatment without creating additional defects at the junction interface. The devices for the pristine PEDOT:PSS buffer layer exhibited an average η of 9.5%–10.2%. This maximum g value was achieved of a η of 10.2% with a $J_{sc}$ of 29.0mA/$cm^2$, a $V_{oc}$ of 0.527V, and a *FF* of 0.669. Once 0.1% Zonyl was added in conductive PEDOT:PSS, the average η value increased to 10.8%–11.34%. The best performance was achieved with a η of 11.34%, a $J_{sc}$ of 29.2mA/$cm^2$, a $V_{oc}$ of 0.541V, and a *FF* of 0.718 [Fig. 2.3(b)]. Obviously, the improvement in the device performance can be attributed to the usage of the 0.1% Zonly addition. In particular, the FF value improved from 0.669 to 0.718 by the 0.1% Zonly addition. The

EQE improved markedly in the visible and near-infrared region for the 0.1% Zonly added devices compared to that of pristine PEDOT:PSS [Fig. 2.3(c)]. Further increases of the Zonly content deteriorated the cell performance (Table 2.1).

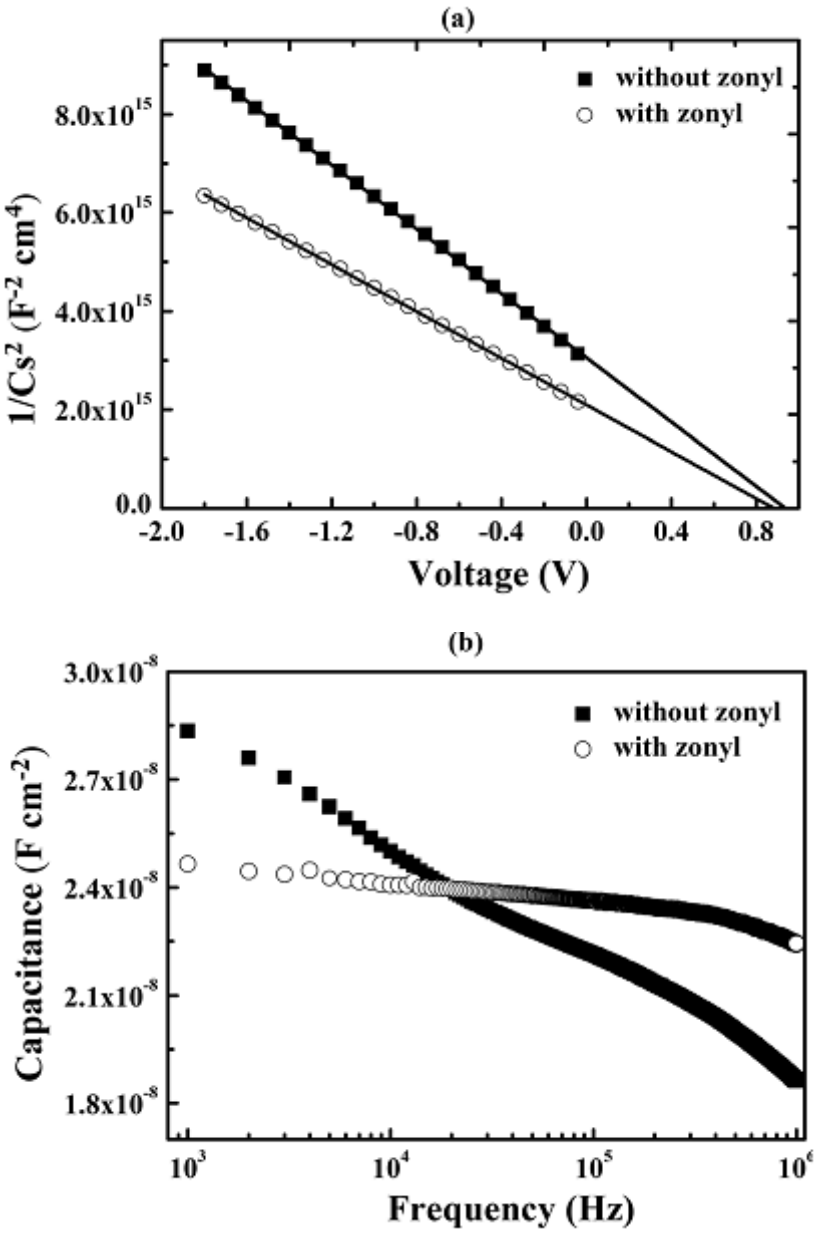


FIG 2.4 (a) $1/C^2$-V and (b) *C-f* plots of c-Si/PEDOT:PSS hybrid diodes with and without an addition of a 0.1% Zonyl fluorosurfactant.

Figure 2.4 shows the $1/C^2$-V plot at 1MHz and *C-f* (*f*: measurement frequency) characteristics of c-Si/PEDOT:PSS composite junction solar cells with and without a 0.1% Zonyl addition. The built-in potential $V_b$ and donor density $N_d$ were 0.87~0.94V and $5.82*10^{15}$ /cm$^3$ for the pristine PEDOT:PSS diode, whereas $V_b$ and $N_d$ were 0.88–0.96V and $7.99*10^{15}$ /cm$^3$, respectively, for the 0.1% Zonly added diode [Fig. 2.4(a)]. The slope of the $1/C^2$-V plot relating to ($1/N_d + 1/N_a$: $N_a$ accepter density) was lower for the 0.1% Zonyl added PEDOT:PSS diode than that of pristine PEDOT:PSS, suggesting that the $N_a$ in the organic increased.

In addition, the junction capacitance was almost independent of *f*, and it was suppressed to be lower for the lower measurement-frequency range in the 0.1% Zonyl added PEDOT:PSS [Fig. 2.4(b)]. These imply the lower interface defect density. [32] Thus, the role of the 0.1% Zonly addition into conductive PEDOT:PSS is considered as the suppression of electron recombination, and/or promote the hole current by enhancing the carrier mobility. [33] This is achieved by inserting PEDOT:PSS with wider energy gap than 1.1 e*V* such that the lowest unoccupied molecular orbital (LUMO) of the organic is higher than the conduction minimum ($E_c$) of c-Si, the lower space charge density at the interface and/or the enhanced hole mobility by the lowering the highest occupied molecular orbital (HOMO) of the organic-valence band maximum ($E_v$) offset. In general, the $V_{oc}$ is described through the relation $V_{oc} = nkT*\ln(J_{sc}/J_0)/q$.

[34] Thus, large LUMO-$E_c$ offset results in a lower $J_0$ and, hence, a larger $V_{oc}$. However, the SE characterization revealed that the HOMO-LUMO gap energy in PEDOT:PSS was almost same for both samples. Both $V_{oc}$ and $J_{sc}$ were 0.52~0.54V and 28~30mA/cm$^2$, respectively, and they were almost independent of the Zonly content up to 0.5% by weight. Thus, the improvement of *FF* value by the 0.1% Zonyl treatment can be attributed to the lowering of space charge layer at the c-Si/PEDOT:PSS interface. It is also well known that the spin-coated PEDOT:PSS exhibit the prominent anisotropic optical property, i.e., the ordinary optical component showing the metallic property and the extraordinary component exhibiting a dielectric behavior. [35] This property also promotes the role of the hole transporting layer as well as the highly transparent conductive layer by adding the 0.1% Zonly. Thus, the improved adhesion of PEDOT:PSS conjugated polymer on hydrophobic c-Si wafer results in the efficient suppression of defect generation at the c-Si/organic interface, resulting in the higher device performance in addition to a native $SiO_x$ layer. [36-39]

In conclusion, we have studied the role of Zonyl fluorosurfactant addition to conductive PEDOT:PSS on the performance of c-Si/PEDOT:PSS hybrid heterojucntion devices. The 0.1% Zonly addition to conductive PEDOT:PSS improved significantly the adhesion on hydrophobic c-Si wafer. As a consequence, a highly efficient

c-Si/organic hybrid solar cell was obtained with the highest power conversion efficiency of 11.34% with a Jsc of 29.2mA/cm$^2$, a Voc of 0.541V, and an *FF* of 0.718. Such Si/organic hybrid cells can potentially further deliver high conversion efficiency combining with the textured structure and the creation of ohmic junction at the rear surface.

## 2.3 Optical anisotropy in co-solvent modified PEDOT:PSS and its effect on the photovoltaic performance of crystalline silicon/organic heterojunction solar cells

Poly(3,4-ethylenedioxythiophene):poly(styrenesulfonic acid) (PEDOT: PSS) has attracted considerable attention as a conducting polymer because of its high electrical conductivity, transparency, structural stability, and other desirable properties. [40-43] Several attempts have been made to further improve the conductivity of PEDOT:PSS by adding polar solvents such as water, methanol (MeOH), dimethyl sulfonate (DMSO), graphene oxide (GO), ZnO nanoparticles, or ethylene glycol (EG). [44-49] These solvents modify the fine structure of the random PEDOT:PSS coils. The addition of EG has been found to enhance the electrical conductivity due to phase separation of the hydrophilic conductive PEDOT and the hydrophobic insulating PSS, which leads to an increase in the hole mobility. [50] In general, PEDOT:PSS exhibits

strong uniaxial optical anisotropy, i.e., the ordinary index of refraction $n_o$ and extinction coefficient $k_o$ indicate metallic behavior, while the extraordinary index of refraction $n_e$ and extinction coefficient $k_e$ indicate a more dielectric behavior. [51, 52] Recently, solar cells based on a crystalline Si (c-Si)/PEDOT:PSS heterojunction structure have been reported to have a power conversion efficiency g of 10%–11%.[53, 54] However, the effect of uniaxial optical anisotropy on the photovoltaic performance of c-Si/ PEDOT:PSS heterojunction solar cells remains an open question.

In the present session, we demonstrate the effect of uniaxial optical anisotropy on the carrier transport properties and photovoltaic performance of c-Si/PEDOT:PSS heterojunction solar cells fabricated by spin coating using either a MeOH solvent alone or MeOH and EG as co-solvents. One-side-polished n-type c-Si(100) wafers with a resistivity of 1–5 Ω*cm and a thickness of 300 μm were used as substrates. The c-Si wafers were RCA cleaned using SC-1 and SC-2 treatments, and then dipped in 5% hydrofluoric (HF) acid to remove any native oxide.

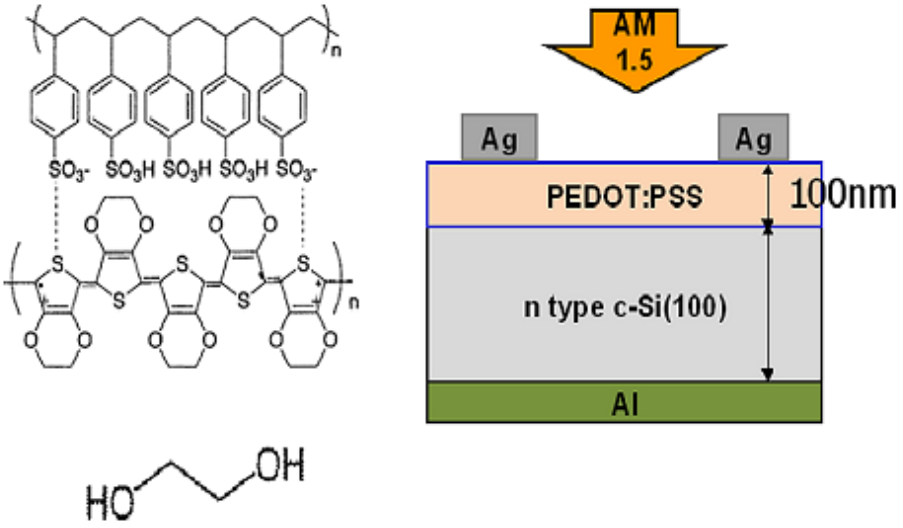


FIG 2.5 Chemical structure of PEDOT:PSS and EG. Also shown is a schematic of c-Si/PEDOT:PSS hybrid solar cells used in this study.

Figure 2.5 shows the chemical structure of PEDOT:PSS and EG, together with a schematic of the c-Si/PEDOT:PSS solar cells used in this study. DMSO (5wt%) was added to filtered (pore size 0.45 μ m) PEDOT:PSS (Clevios PH1000) to render it conductive. Blended solutions were then prepared using MeOH alone or MeOH and EG as co-solvents with different weight ratios. Thin films were formed by spin coating these solutions onto the Si substrates at 1000rpm for 60s, followed by thermal annealing at 140℃ for 30min. Finally, a top electrode (5mm square, thickness 0.1mm) was formed using silver paste and a pattern printer. The outer edge of each silver electrode was covered with an opaque mask to block incident light.

The electronic, structural, and morphological properties of the

PEDOT:PSS films were investigated using spectroscopic ellipsometry (SE: Jobin Yvon UVISEL), atomic force microscopy (AFM: SII nanotechnology, SPA-300/SPI-3800), X-ray diffraction (XRD), and X-ray photoelectron spectroscopy (XPS: ULVAC-PH1). The solar cell performance was characterized using current density-voltage (J-V) measurements in the dark and under AM1.5G illumination with 100mW/cm$^2$ of simulated solar light (Bunkoukeiki CEP-25BX). The optical properties of several PEDOT:PSS films with different solvent treatments were determined using ellipsometric measurements at an angle of incidence of 70°, in the energy region of 0.8 to 5.0eV.

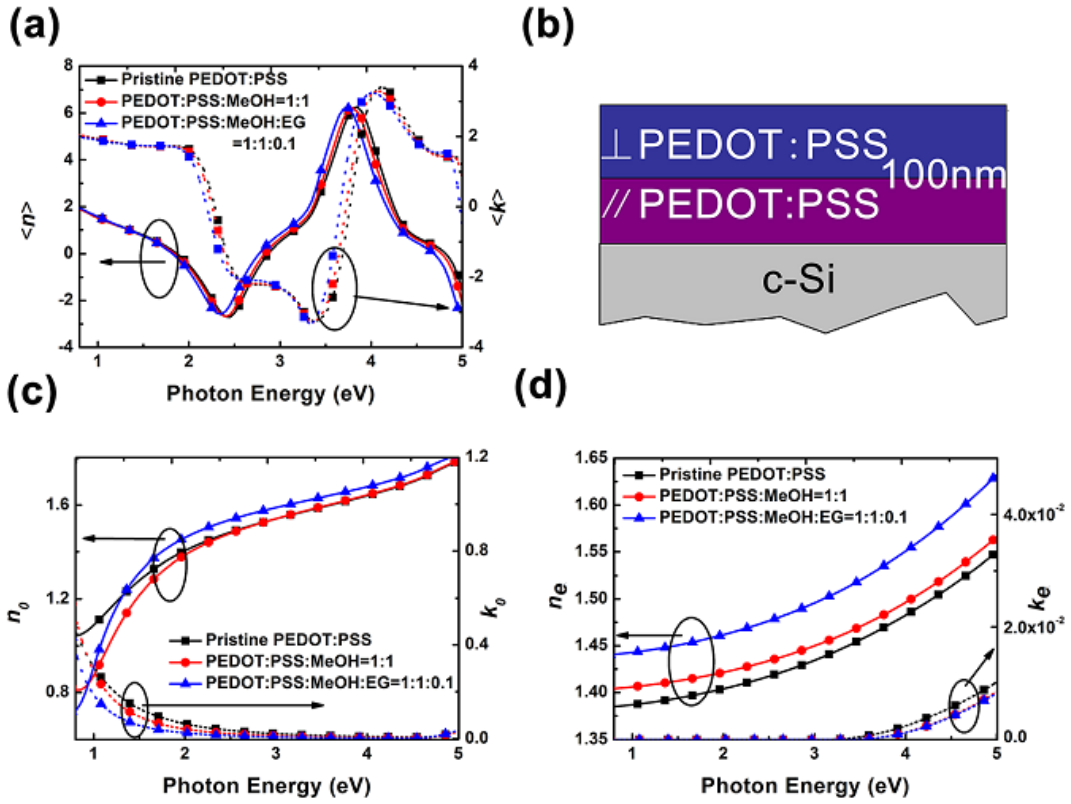


FIG 2.6 (a) Spectra of <*n*> and <*k*> for c-Si/PEDOT:PSS films: pristine,

MeOH-modified, and co-solvent modified films on c-Si, measured at 70°. (b) Optical model used for spectral analysis. (c) $n_o$ and $k_0$ spectral components and (d) $n_e$ and $k_e$ spectral components for the corresponding co-solvent modified PEDOT:PSS films.

Figure 2.6(a) shows measured spectra for the index of refraction <*n*> and extinction coefficient <*k*> for ~100nm thick pristine, MeOH-modified, and co-solvent modified PEDOT:PSS films. No marked differences in the <*n*> or <*k*> spectra were observed for different incident directions of the probe light, suggesting the absence of in-plane optical anisotropy. The measured spectra were analyzed using a Tauc-Lorentz (TL) oscillator and Drude model, taking optical anisotropy into consideration. The optical model used in this study is shown in Fig. 2.6(b), and consists of a single layer with uniaxial optical anisotropy: //PEDOT:PSS (ordinary $n_o$, $k_o$) and ⊥PEDOT:PSS (extraordinary $n_e$, $k_e$). The best fits to the ($n_o$, $k_o$) and ($n_e$, $k_e$) spectra for the pristine, MeOH-modified, and co-solvent modified PEDOT:PSS films are shown in Figs. 2.6(c) and 2.6(d), respectively. For all samples, the $n_0$ and $k_0$ spectra indicate metallic behavior, and are almost independent of the concentration of MeOH or EG. In particular, the $k_0$ spectra in the infrared region of 0.8–1.0 eV, corresponding to free carrier absorption, are very similar, which implies that the free carrier concentration *N* is almost

unchanged by solvent addition.[55, 56] On the other hand, dielectric behavior is more dominant for the ne and $k_e$ spectra. In contrast, $n_e$ is seen to increase significantly by co-solvent addition, whereas $k_e$ remains almost unchanged. A quantitative analysis of the XPS spectra (S2p) of PEDOT:PSS with or without co-solvent addition revealed that the relative concentration of PEDOT to PSS was higher near the surface for the co-solvent modified films. Furthermore, it was found that the addition of MeOH or MeOH/EG led to an increase in the intensity of an XRD peak at around $2\theta = 26^\circ$, which is associated with the (020) planes in the orthorhombic unit cell of PEDOT.[57] This indicates an improvement in crystallinity compared to the pristine film. It has been reported that the addition of a polar organic solvent with a high dielectric constant can introduce a screening effect that suppresses the electrostatic interaction between PEDOT and PSS, and thus promotes interactions among PEDOT molecules that lead to crystallization.[58] These findings imply that the addition of EG causes enhanced phase separation of PEDOT and PSS polymer chains and improves the crystallinity of the PEDOT phase. This leads to densification of the PEDOT:PSS network, which can effect the optical anisotropy of the resulting thin films.[48,59]

The carrier transport parameters for the films used in the present study, i.e., the free carrier concentration $N$ and the carrier mobility $\mu$, were also determined from $k_0$ spectra in the infrared region using the plasma

frequency $\omega_p = (Ne^2/\varepsilon_0 m^*)^{0.5}$ and $\mu = e/m^*\Gamma_d$ relations, where $\Gamma_d = 1/\tau$ is a damping factor determined by the dielectric constant $\varepsilon(E) = \varepsilon\infty - [A_d/(E^2+\Gamma_d^2)]$. Here, $\mu$ represents the average hole mobility within a typical grain.[60, 61] Thus, $\mu$ is proportional to $1/\Gamma_d$ and the influence of scattering at grain boundaries is not considered. $\varepsilon\infty$ and $A_d$ are the dielectric constant e in the high-frequency region and a constant, respectively. Here, an effective mass m* of $0.82m_0$ was used, where $m_0$ is the free-electron mass. [61] The values for $\omega_p$, *N*, and $\mu$ were found to be 1.41 e*V*, $1.18*10^{21}cm^{-3}$, and $1.23cm^2/Vs$ for the pristine film, 1.38 e*V*, $1.13*10^{21}cm^{-3}$, and $2.14cm^2/Vs$ for the MeOH-modified film, and 1.44 e*V*, 1.23 $cm^2/Vs$, and $3.92cm^2/Vs$ for the co-solvent modified film, respectively. Thus, the SE results provide information on both the optical constants and the carrier transport parameters for conductive PEDOT:PSS polymers.

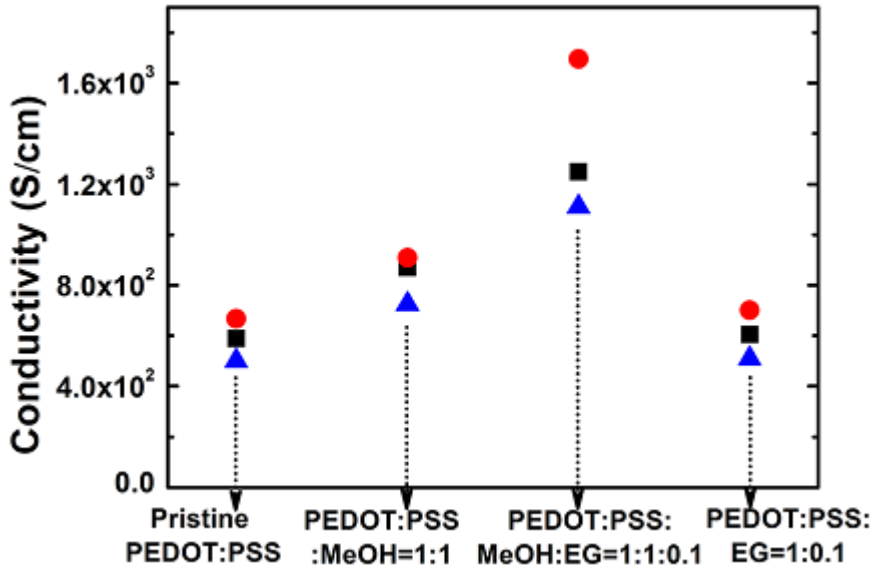


FIG 2.7 Conductivity of PEDOT:PSS films fabricated by spincoat

using either MeOH, EG alone, or MeOH and EG as co-solvents measured for four different ~100nm thick samples. The results for pristine PEDOT:PSS are also shown as a reference.

| | $\Gamma_d$ /e*V* | $\tau$ /fs | $\mu$ /cm$^2$/Vs | $\omega_p$ /e*V* | *N*/ $10^{21}$cm-$^3$ | $R_{sh}$ Ω/□ |
|---|---|---|---|---|---|---|
| Pristine | 1.15 | 9.2 | 1.23 | 1.41 | 1.18 | 335 |
| MeOH | 0.66 | 16.1 | 2.14 | 1.38 | 1.13 | 250 |
| MeOH+EG | 0.36 | 29.5 | 3.92 | 1.44 | 1.23 | 149 |

TABLE 2.2 Carrier transport parameters of corresponding resulted PEDOT:PSS thin films use different solvent addition.

Figure 2.7 shows the conductivity for pristine, MeOH-modified, EG-modified, and co-solvent modified PEDOT: PSS films. For each type of film, three different samples were measured, and the conductivity was evaluated using $\sigma = 1/R_{sh}d$, where $R_{sh}$ is the sheet resistance determined from four-point probe measurements, and *d* is the film thickness obtained from SEM observations. The conductivity is seen to be markedly enhanced by the use of the co-solvent, compared to the case for MeOH or EG alone. It has previously been reported that the electrical conductivity of PEDOT:PSS can be increased by the addition of polyethylene glycol solvents, depending on their concentration and molecular weight. [48]

The increase in conductivity seen in Fig. 2.7 for the MeOH and co-solvent modified films is in reasonable agreement with the change in mobility determined from the SE spectra. Figure 2.8 shows the *J-V* characteristics determined in the dark and under AM1.5G illumination with 100mW/cm$^2$ simulated solar light, in addition to external quantum efficiency (EQE) spectra for the three types of films. The open circuit voltage $V_{oc}$, short-circuit current density $J_{sc}$, fill factor *FF*, and η are summarized in Table 2.2 for the pristine device and devices modified with different amounts of MeOH and EG.

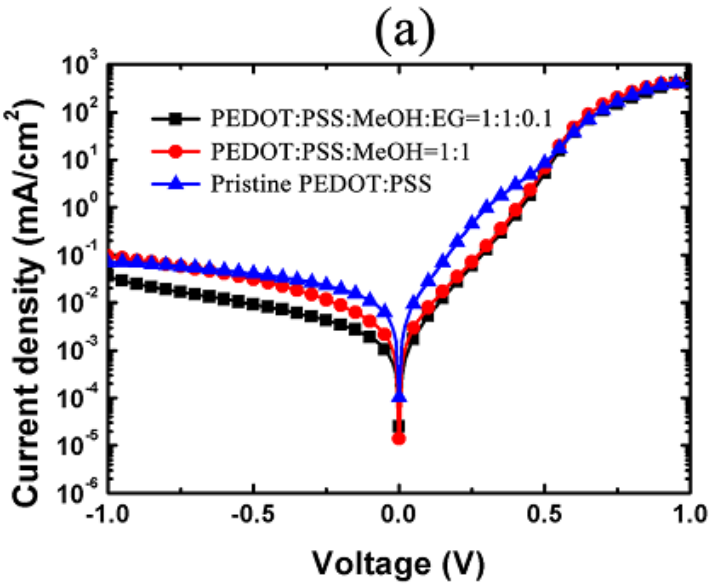

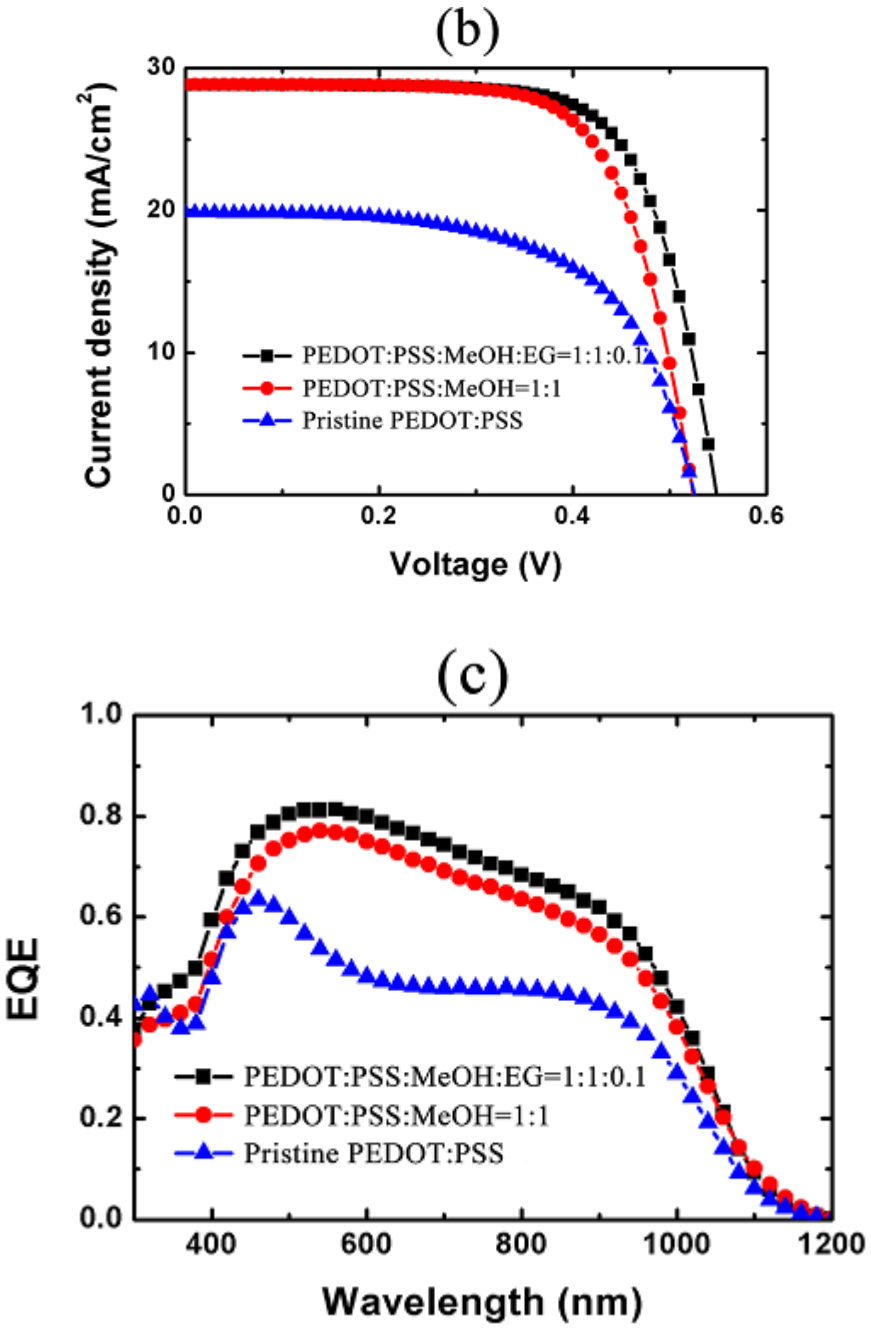


FIG 2.8 *J-V* curves for c-Si/PEDOT:PSS hybrid solar cells with pristine, MeOH-modified, and co-solvent modified PEDOT:PSS buffer layers (a) in the dark and (b) under simulated AM1.5G illumination. (c) EQE spectra for the corresponding c-Si hybrid solar cells.

As seen in Fig. 2.8(a), the dark current density $J_d$ is significantly

reduced under forward and reverse conditions by the addition of MeOH, which is clear evidence for the suppression of electron recombination. This implies that by using MeOH as a solvent, the carrier transport properties can be improved without creating additional defects at the junction interface.

| Conc. | $J_{sc}$ (mA/cm$^2$) | $V_{oc}$ (V) | $FF$ | $\eta$ (%) | $R_s$ ($\Omega$ cm$^2$) | $R_{sh}$ (k$\Omega$ cm$^2$) |
|---|---|---|---|---|---|---|
| 1:0:0 | 19.85 | 0.525 | 0.612 | 6.38 | 0.72 | 13.0 |
| 1:1:0 | 29.02 | 0.527 | 0.669 | 10.23 | 0.77 | 16.7 |
| 1:1:0.1 | 28.79 | 0.548 | 0.711 | 11.23 | 0.64 | 56.3 |
| 1:0:0.1 | 4.71 | 0.355 | 0.453 | 0.76 | 7.06 | 3.9 |
| 1:1:0.3 | 13.88 | 0.459 | 0.612 | 4.20 | 1.12 | 10.2 |
| 1:1:0.5 | 3.45 | 0.480 | 0.644 | 1.07 | 1.38 | 10.6 |

TABLE 2.3 Performance parameters for c-Si/PEDOT:PSS hybrid solar cells with different MeOH and EG concentrations. The concentration is shown as the wt.% ratio of (PEDOT:PSS):MeOH:EG.

The devices with a pristine PEDOT:PSS layer exhibited an average η of 6.38%, whereas a co-solvent modified device exhibited a value of 11.23% with a $J_{sc}$ of 28.79mA/cm$^2$, a $V_{oc}$ of 0.548*V*, and an FF of 0.711. As seen in Fig. 2.8(b), under optical illumination, the use of MeOH leads to a large improvement in the device performance. However, the highest performance is obtained by the use of the MeOH/EG co-solvent. If the photovoltaic performance is governed by *N*, the EQE at wavelengths of 1000~1200nm, where free carrier absorption is dominant, should be most strongly suppressed by an increase in *N*. [55, 56] However, as seen in Fig.

2.8(c), the EQE was enhanced over the entire wavelength region by the addition of the MeOH/EG co-solvent. Since the increase in photovoltaic performance was achieved for devices that also exhibited higher electrical conductivity, as shown in Fig. 2.7, it can be concluded that the improvement was the result of an increase in $\mu$ rather than a change in $N$.

In summary, we demonstrated the effect of uniaxial optical anisotropy on the photovoltaic performance of c-Si/PEDOT:PSS heterojunction solar cells produced by spin coating using either a MeOH solvent or MeOH and EG co-solvents. It was found that the use of the co-solvents led to an increase in $n_e$ and a reduction in the film thickness that promoted densification of the PEDOT:PSS network. This resulted in an increase in $\mu$ in the films. A solar cell fabricated using such a film exhibited a relatively large $\eta$ of 11.23%, with a $J_{sc}$ of 28.79mA/cm$^2$, a $V_{oc}$ of 0.548$V$, and an $FF$ of 0.71.

## 2.4 Summary

In this chapter, we demonstrate a highly efficient hybrid crystalline silicon (c-Si) based photovoltaic devices with hole-transporting transparent conductive poly-(3,4-ethlenedioxythiophene): poly(styrenesufonic acid) (PEDOT:PSS) films, incorporating a Zonyl

fluorosurfactant as an additive, compared to nonadditive devices. The usage of a 0.1% Zonly treated PEDOT:PSS improved the adhesion of precursor solution on hydrophobic c-Si wafer without any oxidation process. The average power conversion efficiency η value was 10.8%-11.3%, which was superior to those of non-treated devices. Consequently, c-Si/Zonyl-treated PEDOT:PSS heterojunction devices exhibited the highest η of 11.34%. The Zonyl-treated soluble PEDOT:PSS composite is promising as a hole-transporting transparent conducting layer for c-Si/organic photovoltaic applications.

In the next session, an investigation was carried out into the effect of uniaxial optical anisotropy in poly(3,4-ethylenedioxythiophene): poly(styrenesulfonic acid) (PEDOT:PSS) on the photovoltaic performance of crystalline Si/PEDOT:PSS heterojunction solar cells fabricated by spin coating using either a methanol (MeOH) solvent alone or using MeOH and ethylene glycol (EG) as co-solvents. Spectroscopic ellipsometry revealed that the extraordinary index of refraction increased by the use of the co-solvents. In contrast, the ordinary index of refraction indicated metallic properties and was almost independent of the concentration of MeOH or EG. The highest conductivity was found for a (PEDOT:PSS):(MeOH):(EG) weight ratio of 1:1:0.1, and this sample exhibited a relatively high power conversion efficiency of 11.23%. These findings suggest that the increase in the extraordinary index of refraction

leads to an enhancement of the hole mobility in PEDOT:PSS, resulting in improved photovoltaic performance.

# Chapter 3

# Employment of Guest Materials to Enhance the c-Si/PEDOT:PSS Hybrid Solar Cell Efficiency

## 3.1 Introduction

There has been tremendous interest in developing next generation photovoltaics based on advanced materials such as quantum dots, semiconducting nanostructures, and conjugated polymers.[62-64] Crystalline silicon (c-Si) remains the basic material for high-efficiency stable photovoltaics, and it has recently been demonstrated that Si nanowire junctions and Si wire arrays from catalytic growth or electrochemical etching can improve light absorption.[65-67] On the other hand, the integration of different nanostructures or polymers into Si-based photovoltaics has been explored widely, and many heterojunction structures have been reported, such as GaN nanorods epitaxially grown on n-type c-Si, InAs nanorods grown on p-type Si, and multiwalled nanotube (CNT) arrays grown in an anodized alumina template on Si substrates.[68-70] Highly conductive

poly(3,4-ethylenedioxythiophene):poly (stylenesulfonate) (PEDOT:PSS) is often used to modify indium tin oxide (ITO) electrodes owing to its superior injection/collection properties by secondary doping of special reagents such as graphene, graphene oxide (GO), CNTs, and metal oxide particles.[71-74]

## 3.2 Effects of Molybdenum Oxide Molecular Doping on the Chemical Structure of PEDOT:PSS and on Carrier Collection Efficiency of c-Si/PEDOT:PSS Heterojunction Solar Cells

Followed with above demonstration, it is also reported that PEDOT:PSS, GO, and metal oxide such as molybdenum trioxide ($MoO_3$) are good candidates for solution-processable hole-transporting materials that exhibits an intense photoluminescence (PL) emission in the 325~550nm region and is expected to find application as a light wavelength conversion layer.[75-78] Furthermore, the $MoO_3$ layer would presumably generate a strong inversion in Si by electrostatic repulsion, as in the cases of dielectric $SiO_x$ and $Al_2O_3$.[79-81] Thus, a high built-in voltage, $V_{bi}$, can be expected at the c-Si/PEDOT:PSS: $MoO_3$ composite interface.

Here in this session, we demonstrate the effect of luminescent $MoO_3$

molecular doping to conductive PEDOT:PSS on the chemical structure and external quantum efficiency (EQE) of n-type c-Si(100)/PEDOT:PSS heterojunction solar cells.

The c-Si wafer (CZ, 3~5Ω*cm, 300 μm thickness) was cleaned by the RCA1 and RCA2 procedures. Highly conductive PEDOT:PSS (Clevios PH1000) with 5wt.% dimethyl sulfonate (DMSO) was used as a starting solution. $MoO_3$ (Kanto Kagaku Ltd. 99.99%) powder flakes with an average size of 1.7 μm were used as a dopant. PEDOT:PSS:$MoO_3$ composite solutions with different $MoO_3$/(PEDOT:PSS: $MoO_3$) 1, 3, 10, and 30 wt.% were stirred for 1 h. Here, as the PEDOT:PSS solid content of PH1000 is around 1%, the dry weight ratios of $MoO_3$/PEDOT:PSS composite thin films were much higher than the values reported in present paper, for example, in the case of the 1wt.% composite, the real dry weight ratio of $MoO_3$/PEDOT:PSS was almost unity. A thin film was formed by spin-coating the precursor solution on RCA-cleaned c-Si wafers at 1000rpm for 60s, followed by thermal annealing at 140℃ for 30min. After that, a top Ag grid electrode was fabricated by pattern printing. Finally, InGa eutectic layer was used as a rear electrode to form an ohmic contact. The PEDOT:PSS:$MoO_3$ composite films were characterized using scanning electron microscopy (SEM), energy dispersive X-ray spectroscopy (EDX), X-ray photoelectron spectroscopy (XPS), and spectroscopic ellipsometry (SE). The PL spectra were

measured using FluoroMax-3 (Horiba Jovin- Yvon) spectrophotometer.

Figure 3.1(a) shows the SEM image of $MoO_3$ particles in conductive PEDOT:PSS. The inset shows the crystal structure of $MoO_3$. $MoO_3$ exhibits a layered structure consisting of vertex-sharing chains of distorted $MoO_6$ octahedra that share edges with two similar chains to form layers. The distortion gives rise to very short "$Mo_{¼}O$" bonds at the apical octahedral positions that terminate the top and bottom of the double octahedral oxide sheets. The resultant two-dimensionally bonded

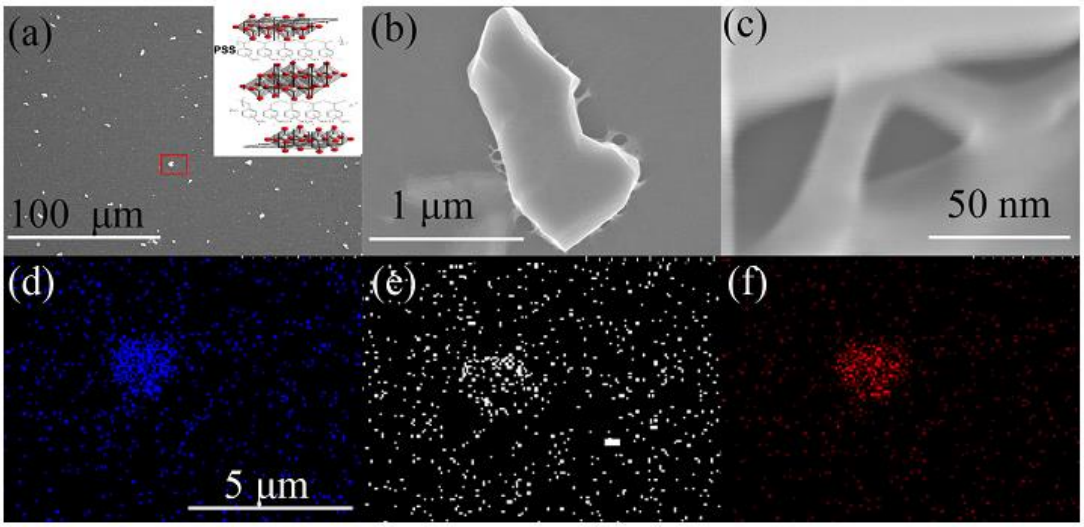


FIG 3.1 SEM images (a)~(c) and EDX maps (d)~(f) (corresponding to the circled region in Fig 3.1(a)) of $MoO_3$ particle in PEDOT:PSS. Inset illustrates schematics for the possible intercalation of PSS chains into layered $MoO_3$, where red and gray spheres denote O and Mo atoms, respectively; (d)~(f) are EDX maps for Mo, O and S. respectively, in $MoO_3$ doped PEDOT:PSS.

layers are stacked in a staggered arrangement and held together by weak Van Der Waals forces. A variety of large guest species can be intercalated into the interlayer Van Der Waals gap.[82] The SEM image shows hair-like projections around the $MoO_3$ flake sheets with an average diameter of 15~20 nm, which is much smaller than the typical mean size of PEDOT particles embedded in PSS chains.[83] EDX maps of Mo, O, and S for the PEDOT:PSS:$MoO_3$ (3wt.%) composite are shown in Figs. 3.1(d)–1(f). Notably, the EDX image of Mo was almost consistent with that of S despite the use of $MoO_3$, and even though S was distributed homogeneously. This implies that the sulphur in PEDOT and/or PSS is coordinated preferentially in $MoO_3$ particle. In addition, the average d spacing of the collected composite powder, as calculated from the four *0k0* reflections in the XRD spectra, was 0.9~1.1nm, i.e., larger than that of pristine $MoO_3$ (0.6nm). Furthermore, XPS revealed that the 3*d* binding energy corresponding to S＝O in PSS decreased less for higher $MoO_3$ concentrations. These findings suggest that the concentration ratio of PEDOT to PSS increased. Thus, the PSS chain was intercalated into the $MoO_3$ flake sheet, modifying the chemical structure of PEDOT:PSS conjugated polymer.

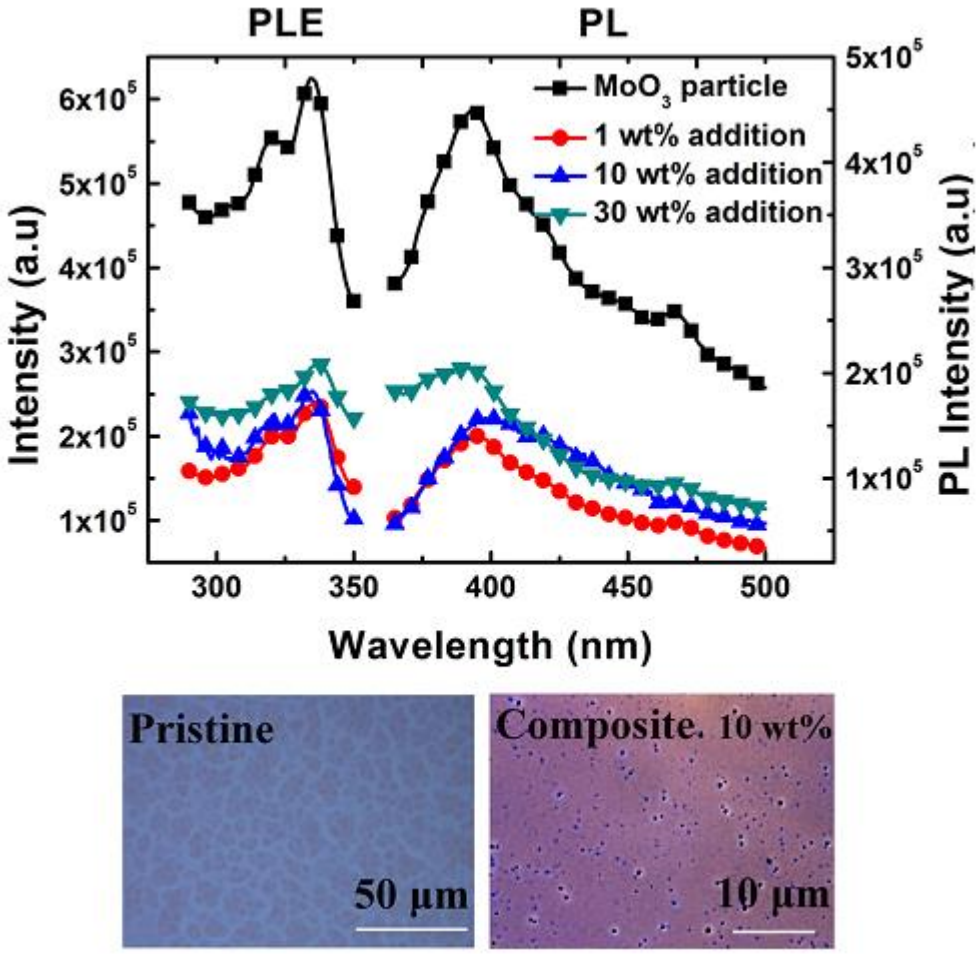


FIG 3.2 PL and PLE spectra of $MoO_3$ doped PEDOT:PSS film. The optical micrographs of PEDOT:PSS with and without 10wt.% $MoO_3$ doping are shown as well.

Figure 3.2 shows the PL spectra of pristine $MoO_3$ and PEDOT:PSS: $MoO_3$ composite films at room temperature and the excitation PL (PLE) spectra for the 400 nm emission. Optical micrographs of PEDOT:PSS with and without $MoO_3$ doping are shown as well. An intense broad band PL emission at 350~500nm having a maximum peak at around 390~400nm was observed, and its intensity increased with $MoO_3$ doping

concentration. Thus, the UV light at 310~345nm was absorbed and efficiently showed an intense broadband PL emission at 350~500nm range. The PL spectra at 350~500nm can be ascribed to the intense near-band-edge (NBE) emission due to the free-exciton recombination and visible light emission by transitions of excited optical centers in the deep levels (DLs). In fact, the $MoO_3$-doped PEDOT:PSS micrograph was deep purple, owing to the intense PL emission at 350~550nm from $MoO_3$. These results suggest that $MoO_3$ may potentially be used for absorbing light at short wavelengths and then emitting at longer wavelengths (350~550nm), which would enhance the carrier collection efficiency of c-Si/PEDOT:PSS solar cells.

Figure 3.3(a) shows the dark current density-voltage ($J_d$-$V$) curves for c-Si/PEDOT:PSS:$MoO_3$ composite heterojunction solar cells with different $MoO_3$ doping concentrations. The inset is a schematic of c-Si/PEDOT:PSS heterojunction solar cell. The effective area of each cell was 5*5$mm^2$. These $J_d$-$V$ curves exhibited a typical p-n junction rectification behavior with the ideality factor $n$ value around 3 (see in Table 3.1). These high values of $n$ indicate that the charge traps in PEDOT:PSS effect the electronic conduction through the diode.[84] The reverse and forward dark currents were suppressed lower than that of a

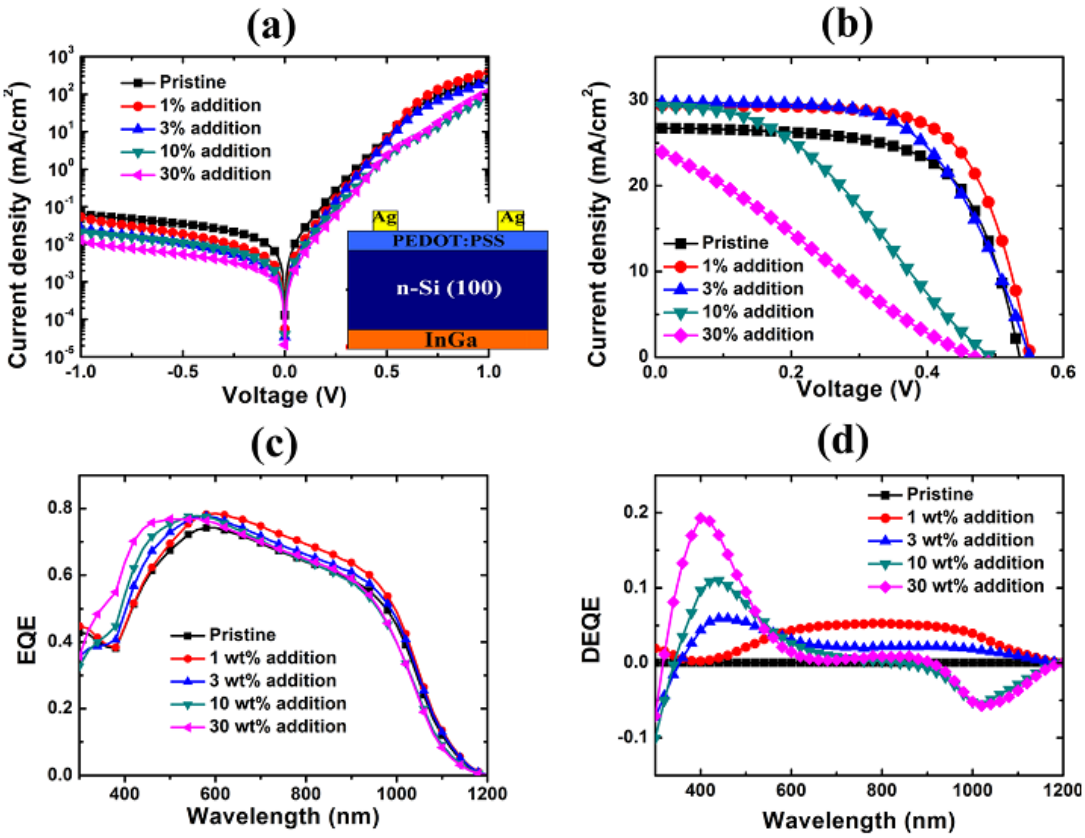


FIG 3.3 (a) $J_d$-$V$ and (b) $J_p$-$V$ curves for c-Si/PEDOT:PSS:$MoO_3$ composite hybrid solar cells with different $MoO_3$ concentrations. Inset shows schematic of the device structure of c-Si/PEDOT:PSS: $MoO_3$ composite solar cells. (c) EQE and (d) DEQE spectra for corresponding c-Si/PEDOT:PSS:$MoO_3$ composite hybrid solar cells. DEQE values are relative to that of a pristine device.

pristine PEDOT:PSS diode by $MoO_3$ addition. The photocurrent density-voltage ($J_p$-$V$) curves obtained under AM1.5G 100mW/cm$^2$ simulated solar light (Bunkoukeiki CEP-25BX) for corresponding c-Si/PEDOT:PSS:$MoO_3$ composite heterojunction solar cells are also shown in Fig. 3.3(b). η was calculated via $\eta = V_{oc}J_{sc}FF/P_{in}$, where $V_{oc}$ is

the open-circuit voltage, $J_{sc}$ is the short-circuit current density, *FF* is the fill factor, and $P_{in}$ is the incident light power. *FF* is determined via $FF = (V_m J_m)/(V_{oc} J_{sc})$, where $V_m$ and $J_m$ are the voltage and current density in the maximum power in the fourth quadrant of the J-V curves, respectively. The photovoltaic performance is summarized in Table 3.1. $J_{sc}$ increased with $MoO_3$ doping concentration up to 3wt.%, and decreased

| Conc. | $J_{sc}$ (mA/cm$^2$) | $V_{oc}$ (V) | *F.F.* | $\eta$ (%) | $R_s$ ($\Omega$ cm$^2$) | $R_{sh}$ ($\Omega$ cm$^2$) | *n* |
|---|---|---|---|---|---|---|---|
| Pristine | 27.20 | 0.538 | 0.656 | 9.89 | 1.09 | $1.0 \times 10^5$ | 3.03 |
| 1 wt. % | 29.4 | 0.552 | 0.683 | 11.01 | 1.26 | $5.1 \times 10^5$ | 2.70 |
| 3 wt. % | 29.7 | 0.551 | 0.610 | 9.86 | 2.35 | $5.7 \times 10^5$ | 2.86 |
| 10 wt. % | 29.3 | 0.495 | 0.381 | 5.48 | 3.64 | $2.8 \times 10^5$ | 3.07 |
| 30 wt. % | 24.3 | 0.470 | 0.252 | 2.90 | 5.39 | $1.6 \times 10^5$ | 3.12 |

TABLE 3.1 Performance details of the c-Si/PEDOT:PSS solar cells with different $MoO_3$-doping concentrations.

markedly with further increase in $MoO_3$ concentration, whereas $V_{oc}$ and *FF* shown the similar tendency as well. Here, the improved photovoltaic parameter should mainly attributed to the addition of $MoO_3$ particles which act the following effects, (1): modified chemical structure of PEDOT:PSS with improved conduction path network; (2): frequency down-conversion centers in the near-*UV* region for more sufficient carrier collection efficiency. Although higher $MoO_3$ concentration would intensify the above effects, as $MoO_3$ is poorly conductive, photovoltaic

performance was suppressed due to increased series resistance, $R_s$. η increased to 11.01% with a $J_{sc}$ of 29.4mA/cm$^2$, a $V_{oc}$ of 0.552V, and an *FF* of 0.683 at a $MoO_3$ concentration of 1wt.%. The $1/C^2$-*V* plot at 1MHz also showed a relatively high $V_{bi}$ of 0.9-1e*V*, resulting in a higher $V_{oc}$ than that of pristine PEDOT:PSS. The EQE and difference EQE (DEQE) spectra for solar cells with different $MoO_3$ doping concentrations are shown in Figs. 3.3(c) and 3.3(d). Here, the DEQE values are relative to that of a pristine c-Si/PEDOT:PSS solar cell, DEQE was found to be positive over the entire wavelength region of 350~1200nm for a $MoO_3$ concentration of 1–3wt.%. At high $MoO_3$ doping concentrations of up to 10~30wt.%, DEQE was markedly enhanced in the 350~550nm regions, with a shorter wavelength shift. It has been reported that polar solvent such as MeOH and ethylene glycol modify the chemical structure of PEDOT:PSS and that the phase separation of PEDOT-PSS enhances the hole mobility of PEDOT:PSS by increasing conduction path network of PEDOT chains.[85, 86] These findings suggest that the increased EQE in the 350~550nm region of c-Si/PEDOT:PSS:$MoO_3$ composite heterojunction solar cells is due to the PL emission of $MoO_3$. Nevertheless, the DEQE values in the infrared region of 900~1200nm were negative.

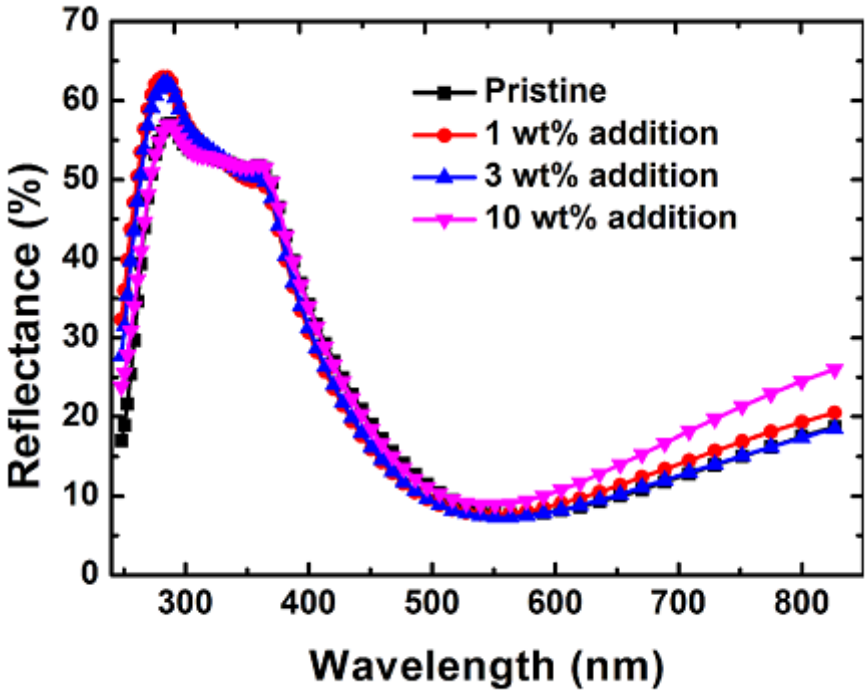


FIG 3.4 Reflectance spectra for c-Si/PEDOT:PSS:$MoO_3$ composite solar cells with different $MoO_3$ doping concentrations. All PEDOT:PSS:$MoO_3$ layer thickness were ~100nm.

The reflectance spectra for PEDOT:PSS:$MoO_3$ composite films, as determined by SE spectra analysis, are shown in Fig. 3.4. The reflectance spectra in the *UV* region corresponding to the absorption of c-Si decreased slightly by $MoO_3$ doping, but no significant changes were observed. AFM revealed that the degree of RMS roughness was 3~9nm (5*5 $\mu m^2$), which is less than that of typical light trapping structure. Thus, the improved EQE in the 350~550nm region does not result from $MoO_3$ acting as an anti-reflection layer, but from the enhanced optical absorption in this region owing to the PL emission from $MoO_3$. The RMS

roughness of the thin film examined by AFM was around 9nm, up to a $MoO_3$ doping concentration of 10wt.%, which is negligibly small for a light-harvesting structure, as compared with that of textured Si(100). However, the EQE in the infrared region of 900~1200nm deteriorated at a $MoO_3$ doping concentration above 10wt.% due to the increased optical reflectivity.

In conclusion, we studied the effect of $MoO_3$ molecular doping to conductive PEDOT:PSS on the chemical structure and photovoltaic properties of c-Si/PEDOT:PSS heterojunction solar cells. The $MoO_3$ molecular doping modified the chemical structure of PEDOT:PSS by the intercalation of PSS into the Van Der Waals gap of $MoO_3$ sheets. These changes enhanced the photovoltaic performance of the c-Si/ PEDOT:PSS solar cells. η increased up to 11.0%. The *UV* absorption and intense PL emission at 350~550nm increased the carrier collection efficiency in c-Si/PEDOT:PSS heterojunction solar cells.

## 3.3 Improved Photovoltaic Performance of c-Si/PEDOT:PSS Hybrid Junction Solar Cells Using Ferroelectric Polymers

It is well known, the Schottky barrier, fabricated by depositing a metal with a high work function on n-type c-Si, may be an alternative to p-n junctions. As is the case for p-n junctions, the Schottky barrier has a built-in electric field that can separate electrons and holes, generating a high photocurrent. However, the barrier that impedes the recombination of electrons at the anode is relatively low, resulting in a saturation current density that is typically much higher than that of p-n junction diodes. This is due to an insufficient electric field at the c-Si/organic interface and poor charge extraction. As a result, the open-circuit voltage $V_{oc}$ is limited to 520~550 mV, which corresponds to half the band gap energy of c-Si. To further increase $V_{oc}$, a higher built-in field at the interface is required. To date, improvement of the photovoltaic performance of Schottky barrier devices has been attempted using poly(3-hexylthiophene) (P3HT), graphene oxide (GO), or perfluorinated ionomer (PFI) due to their high electron affinity that reduces electron recombination at the anode.[97-99] These devices were achieved by inserting an organic semiconductor layer with an energy gap wider than 1.1 eV between the silicon and the metal

such that the lowest unoccupied molecular orbital (LUMO) of the organic is much higher than the conduction band minimum ($E_c$) of Si. In addition, to minimize resistive losses, the valence band maximum ($E_v$) should be as close as possible to the lowest occupied molecular maximum orbital (HOMO) and the hole mobility in the organic layer should be higher. However, these effects have not yet surpassed the $V_{oc}$ of ~700mV obtained by c-Si/hydrogenated amorphous silicon (a-Si:H) heterojunction (HIT) solar cells.[100, 101] To this end, the use of a ferroelectric layer (FE) is one possible method of enhancing the photovoltaic parameters. Significant improvement of photovoltaic performance and several specific features have been reported for poly(3-hexylthiophene): (phenyl-C61-butyric acid methyl ester)(P3HT/PCBM) organic thin-film solar cells by inserting an FE layer.[102, 103] However, few studies have been performed using c-Si/organic Schottky junction photovoltaic devices.

In the present session, we demonstrate the improved photovoltaic performance of c-Si/PEDOT:PSS Schottky junction solar cells with a vinylidene fluoride-tetrafluoroethylene copolymer P(VDF-TeFE) FE layer using a large internal electric field provided by a permanent electrical polarization.

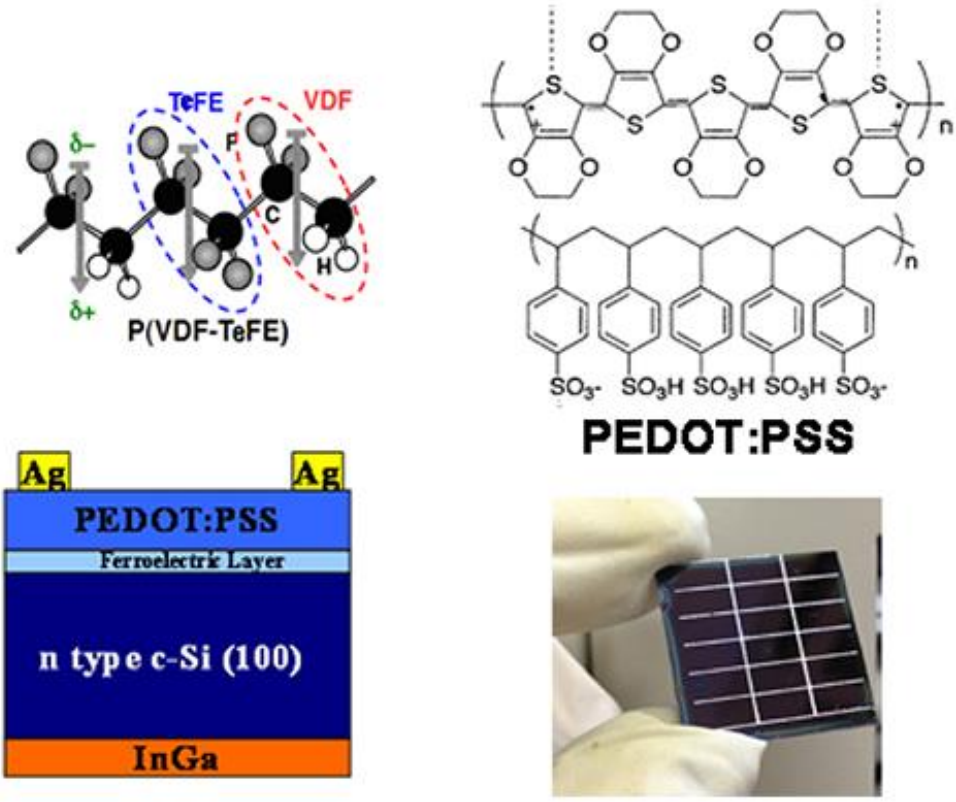


FIG 3.5 Device schematic and the molecular structure of PEDOT:PSS and P(VDF-TeFE) ferroelectric polymer

Figure 3.6 shows a schematic of the photovoltaic devices used in this study, along with the molecular structures of P(VDF-TeFE) and PEDOT:PSS. P(VDF-TeFE) is a random copolymer consisting of $-((-CF2-CH2)_x-(-CF2-CF2-)_{1-x})_n$ chains with a regular intra-chain period of 2.6Å, controlled by the C-C bonds between fluorine pairs. The arrows in the figure indicate the direction of the net dipole moments, which point from the fluorine side to the hydrogen side of the chains.[104] In the ferroelectric phase, the all-trans chains are arranged in parallel rows as quasi-hexagonal close packing with an orthorhombic *mm2* structure.

0.05–1wt.% P(VDF-TeFE) dissolved in acetone was spin-coated at 1000rpm for 1min followed by thermal annealing at 130℃ for 10min. Subsequently, ~100nm thick DMSO (5wt.%) and Zonyl (0.1wt.%) doped PEDOT:PSS (Clevios PH1000) was spin coated.[94] All devices were fabricated from commercial high-conductive grade PEDOT:PSS spin-coated on FE/n-type CZ c-Si(100) wafers (1~5 Ω*cm, 300 μm thick) at 1000rpm for 1min, followed by thermal annealing at 140℃ for 30min. The solar cell structure was a Ag/PEDOT:PSS (100nm thick)/P(VDF-TeFE)/c-Si/InGa with FE layers of different thicknesses. The solar cell performance was characterized by current density-voltage (J-V) measurements in the dark and under illumination of AM1.5G, 100mW/cm$^2$ simulated solar light (Bunkoukeiki CEP-25BX). The active area of the device, as defined by the top silver grid electrode, was 5*5 mm$^2$. The P(VDF-TeFE) films were characterized using X-ray diffraction (XRD), scanning electron microscopy (SEM), Fourier-transform infrared reflection absorption spectroscopy (FTIR), and atomic force microscopy (AFM). The capacitance hysteresis loop was also measured using a standard FE capacitor and c-Si/FE/PEDOT:PSS/Ag solar cell structures. The poling of the FE layer was performed under forward and reverse DC bias conditions at an electric field E of +2V (2*10$^3$ k*V*/cm) and -15V (5*10$^4$ k*V*/cm), respectively, for different periods.

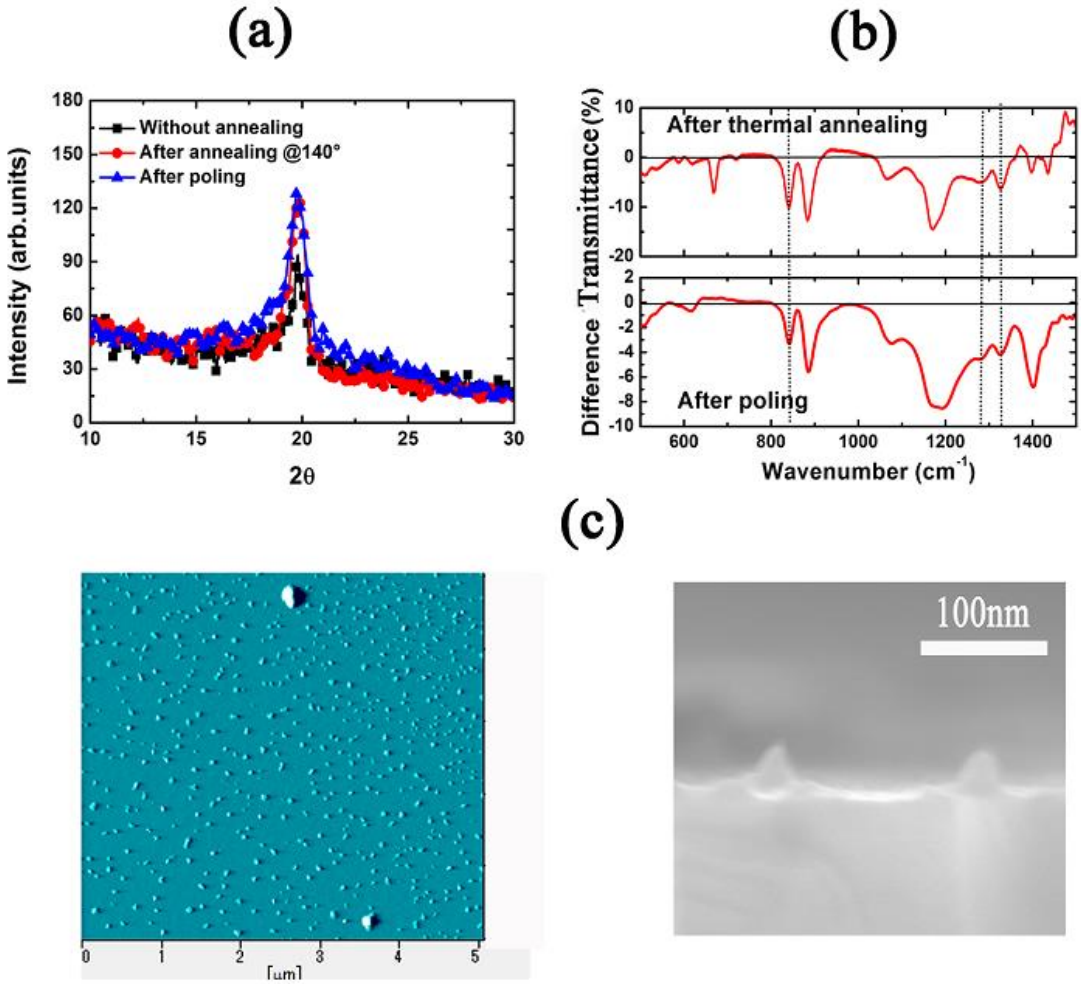


FIG 3.6 (a) XRD patter and (b) FTIR spectra of a 100nm thick P(VDF-TeFE) layer in three states: as-grown, annealed at 140℃ for 30min, annealed and poling under a reverse DC bias of $5*10^4$k*V*/cm for 30min. The spectra are shown as a different spectra referred to those of as-grown and the annealed states. (c) Plane and cross-sectional SEM images of a 3nm thick P(VDF-TeFE) later after thermal annealing at 140℃ for 30min.

Figures 3.7(a) and 3.7(b) show an XRD pattern and a difference transmittance FTIR spectra from ~100nm thick P(VDF-TeFE) in three

states: as-grown, annealed at 140℃ for 30min, and annealed and poled by reverse DC bias poling at $5*10^4$ k*V*/cm for up to 1h. The P(VDF-TeFE) films generated a strong and sharp combined (110)-(020) XRD diffraction peak at a $2\theta = 20^\circ$, and their intensities increased after thermal annealing at 140℃ and subsequent poling. The different FTIR spectra shown are referred to those of as-grown and annealed states. Here, the IR absorption peaks at 840, 1279, and 1324 $cm^{-1}$ corresponding to the trans conformation (Fig. 3.7(b)) were enhanced after thermal annealing and subsequent poling.[105, 106] Therefore, the film crystallinity correlates with the degree of trans conformation. Figure 3.7(c) shows AFM and cross-sectional SEM images of an ultra-thin spin-coated 3nm thick P(VDF-TeFE) layer after thermal annealing at 140℃ for 30min. The as-grown film was a continuous network, but the film became discontinuous and rougher after thermal annealing. SEM and AFM roughness measurements that were <5nm before thermal annealing increased to a diameter of 10~40 nm and a height of ~30 nm after thermal annealing. Poling did not significantly affect the morphology of FE dots. Similar results were obtained in case of the FE films formed by Langmuir-Blodgett (LB) deposition. Therefore, the P(VDF-TeFE) layer was discontinuous and contained a self-assembled dot structure after thermal annealing.

Figures 3.8(a) and 3.8(b) show J-V curves obtained in the dark and

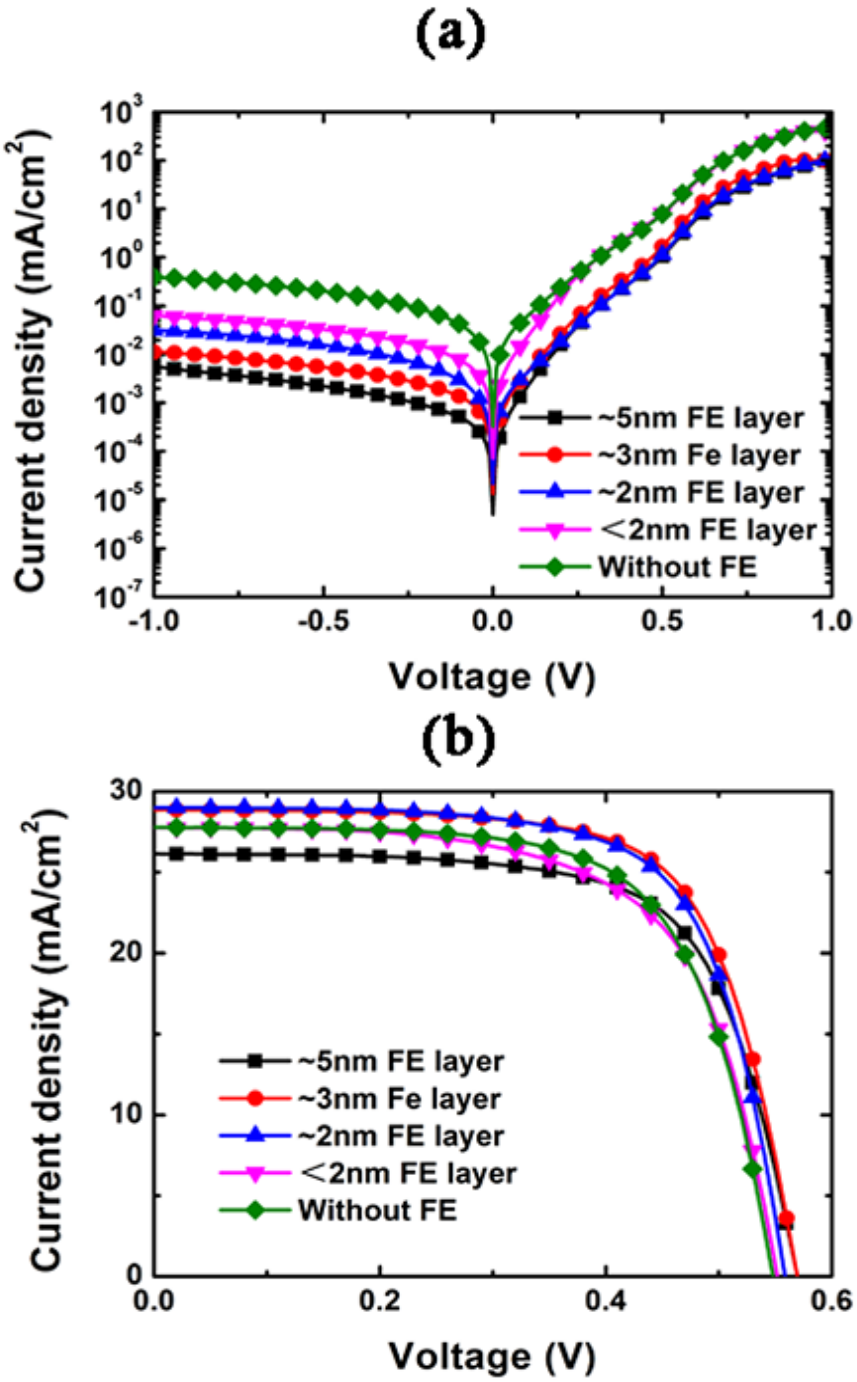


FIG 3.7 J-V curves in the dark and under exposure of AM1.5G simulated solar light for as-deposited c-Si/FE/PEDOT:PSS diodes with different FE layer thicknesses.

under AM1.5G, 100mW/cm$^2$ simulated solar light exposure for

as-deposited c-Si/FE/PEDOT:PSS Schottky junction devices with different FE layer thicknesses. The photovoltaic performance is summarized in Table 3.2. The reverse and forward dark currents were suppressed and fell below the values for a pristine PEDOT:PSS diode. η increased to 11.4% with a short circuit current density $J_{sc}$ of 28.85mA/cm$^2$, an open circuit voltage $V_{oc}$ of 0.57V, and a fill factor *FF* of 0.692 for a 3nm thick FE layer diode. A thicker P(VDF-TeFE) layer can introduce a stronger electric field into c-Si. However, the increased FE layer thicknesses also enhance the contact resistance, which reduces device efficiency. Therefore, the FE layer thickness was kept well below ~10 nm so that the carriers could conduct through it to the PEDOT:PSS and the electrodes. The influence of the induced electric field on device performance is evident in c-Si/PEDOT:PSS devices with an FE active layer. The insertion of a 3nm thick P(VDF-TeFE) layer leads to a considerable increase in all photovoltaic parameters, i.e., g, $J_{sc}$, $V_{oc}$, and *FF*.

| FE thickness | $J_{sc}$ (mA/cm$^2$) | $V_{oc}$ (V) | *F.F.* | $\eta$ (%) |
|---|---|---|---|---|
| ~5 nm | 26.12 | 0.57 | 0.684 | 10.2 |
| ~3 nm | 28.85 | 0.57 | 0.692 | 11.4 |
| ~2 nm | 28.99 | 0.56 | 0.689 | 11.2 |
| <2 nm | 27.76 | 0.55 | 0.645 | 9.9 |
| Without FE | 27.77 | 0.54 | 0.68 | 10.2 |

TABLE 3.2 Performance details of c-Si/PEDOT:PSS hybrid devices with thin FE layers of different thicknesses.

Figure 3.9(a) shows *J-V* curves of a c-Si/FE(3nm thick)/PEDOT:PSS photovoltaic device at the c-Si/PEDOT:PSS interface after poling under a negative DC bias of $5*10^4$ k*V*/cm, as shown in the inset. The photovoltaic parameters are summarized in Table 3.3. For comparison, *J-V* curves for the corresponding solar cell after forward bias poling of $2*10^3$ k*V*/cm and for the pristine PEDOT:PSS device without an FE layer after applying negative DC bias of $5*10^4$ k*V*/cm are also shown in Figs. 3.9(b) and 3.9(c), respectively. The influence of the electric field induced by the negative DC bias poling on device performance is evident in the c-Si/PEDOT:PSS Schottky junction, as shown in Fig. 3.9(a). The addition of several monolayers (ML) FE layers led to a small increase in $J_{sc}$, even before poling, probably because of partial poling of the P(VDF-TeFE) film during thermal annealing. After poling of the FE layer by applying a large positive voltage to the Ag electrode, an extra electric field was added to the PEDOT:PSS layer, which had the same direction as the electric field induced by the electrode work-function difference. After poling, $J_{sc}$ increased from 27.2 to 29.7mA/cm$^2$, which is evident enough, although there was often a small variation in the maximum $J_{sc}$ caused by the PEDOT:PSS thickness and the variation of remanent P(VDF-TeFE) polarization under different experimental conditions.

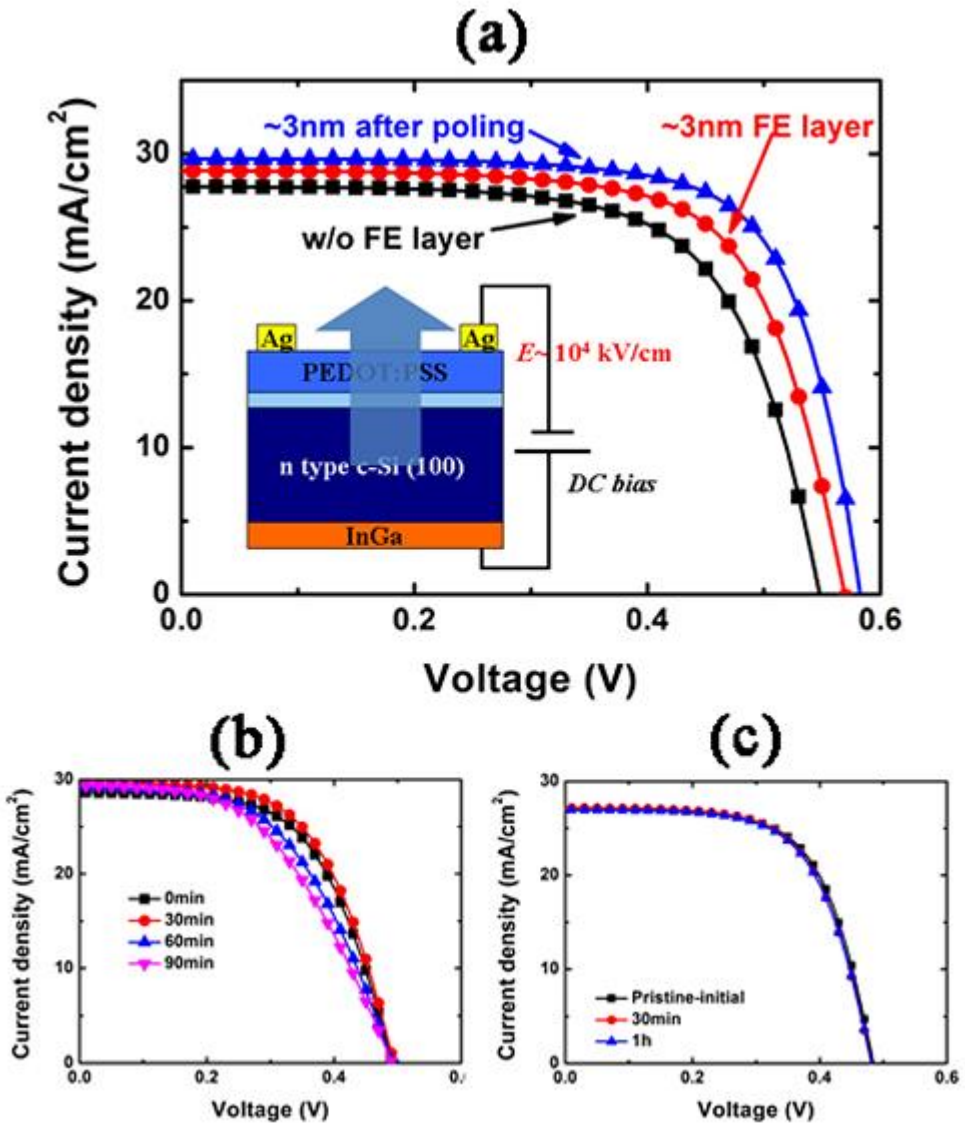


FIG 3.8 (a) J-V curves in the dark and under exposure of AM1.5G simulated solar light for c-Si/FE(3nm thick)/PEDOT:PSS diodes after poling of the FE layer under a reverse DC bias of $5*10^4$ k*V*/cm for different periods. The inset shows the poling conditions. (b) *J*-*V* curves for the corresponding device after poling under a forward DC bias of $2*10^3$ k*V*/cm for different periods. (c) photo *J*-*V* curves for a pristine device without an inserted FE layer under a reverse DC bias of $5*10^4$ k*V*/cm for different periods.

| Device | $J_{sc}$ (mA/cm$^2$) | $V_{oc}$ (V) | *F.F.* | $\eta$ (%) |
|---|---|---|---|---|
| w/o FE layer | 27.8 | 0.54 | 0.68 | 10.2 |
| 3 nm FE layer | 28.9 | 0.57 | 0.69 | 11.4 |
| 3 nm after poling | 29.7 | 0.58 | 0.71 | 12.3 |

TABLE 3.3 Performance details of c-Si/PEDOT:PSS solar cell with a 3nm thick FE layer before and after poling

The electric field induced by the FE layer increases the $V_{oc}$ of the c-Si/PEDOT:PSS devices as well. This increase in $V_{oc}$ can be understood by considering the photovoltage loss mechanism of the c-Si/PEDOT:PSS Schottky junction devices. First, the field-assisted e-h dissociation process increases the photocurrent generation by reducing recombination while preserving the high quasi-Fermi energy of the electrons, which then contribute to increasing $V_{oc}$. Second, the voltage loss in the photovoltaic devices is also related to the saturated dark current of the device. The saturated dark current of the poled FE copolymer film was reduced by two orders of magnitude, as shown in Fig. 3.8(b). The reduced saturated dark current can be ascribed to a high carrier injection barrier under the reverse bias introduced by the FE dipole layer. The pole FE layer also controls the dark current of the device. Whereas photovoltaic parameters, i.e., g, $J_{sc}$, $V_{oc}$, and *FF* decreased by poling under the lower forward bias

stress of $2*10^3$ k*V*/cm. No significant changes of the *J-V* curve were observed after poling the FE layer in the pristine PEDOT:PSS device without inserted FE layer for up to 1h. Therefore, poling the FE layer under a negative DC bias significantly increased the photovoltaic performance. The electric field induced by the 3nm thick FE polymer films significantly increased the carrier collection ability and device efficiency, from 10.2% without the FE film to 12.3% after poling the FE layer. The electric field induced by inserting a 3nm thick FE layer between the c-Si and the PEDOT:PSS layer increased η to 12.3% with a $V_{oc}$ of 0.58V, a $J_{sc}$ of 29.7mA/cm$^2$, and an an *FF* of 0.71 after 30min of poling under a negative DC bias.

Figure 3.10(a) shows a capacitance hysteresis loop for c-Si/FE/PEDOT:PSS device with a 3nm thick FE layer at different poling periods under a DC reverse bias of -15V ($5*10^4$k*V*/cm). The built-in electric field introduced by the P(VDF-TeFE) layer into the PEDOT:PSS was derived to be $E=d\sigma_p/\varepsilon_0\varepsilon_{FE}L$, where $\sigma_p$ is the polarization charge density, *d* is the thickness of the P(VDF-TeFE) layer, *L* is the thickness of the PEDOT:PSS layer, and $\varepsilon_{FE}$ is the relative dielectric constant of the P(VDF-TeFE) fims.[102] The ultrathin FE layer has a high surface charge density, which raises the electrostatic potential at the surface of the c-Si. The FE polymer was assumed to uniformly cover the entire surface and be polarized in a direction nearly perpendicular to the plane.

Assuming

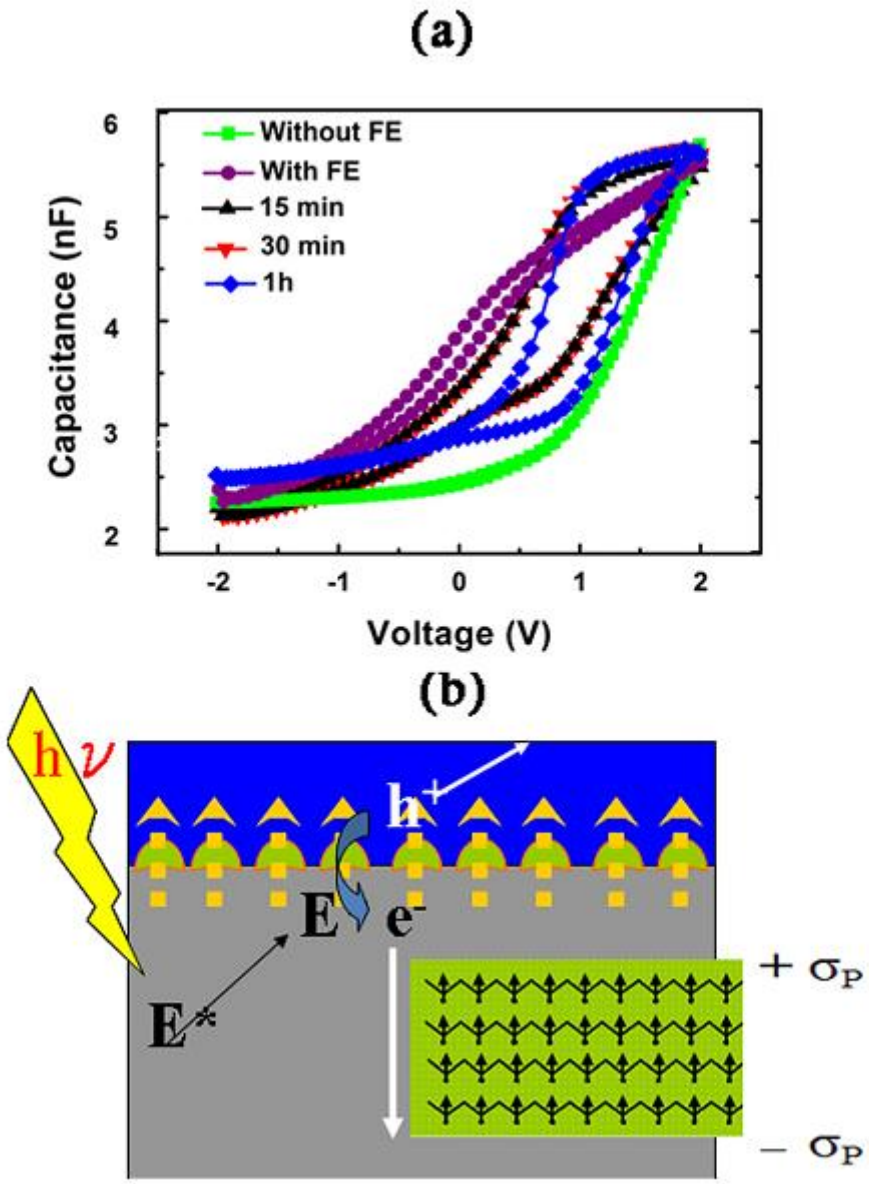


FIG 3.9 (a) Capacitance hysteresis loop of c-Si/FE/PEDOT:PSS junction solar cell with a 3nm thick FE layer measured at 1MHz for different poling periods. (b) A schematic of the remanent polarization of FE dot array at the c-Si/PEDOT:PSS interface.

that the DC bias stress is mostly supplied to the 3nm thick insulating FE

layer, the hysteresis loop becomes prominent and the memory window of the annealed state was increased from 0.4V to 0.8V ($2.6*10^3$ kV/cm) after poling. This value is significantly higher than the barrier height of the c-Si/PEDOT:PSS Schottky junction (0.5~0.55V).

Using the nominal remnant polarization of $100mC/m^2$ for P(VDF-TeFE), the electric field induced by 3 ML of P(VDF-TeFE) in 100nm thick PEDOT:PSS was calculated to be approximately 50 V/ μ m. Therefore, the 3 ML of FE P(VDF-TrFE) can induce an electric field in the PEDOT:PSS layer that is sufficient to transport holes and suppress non-radiative recombination. However, the actual induced electric field might be less than the model predicts, because of factors such as charge screening, possible incomplete coating, and poling of the FE layer. The non-continuous morphology of P(VDF-TeFE) allows efficient charge extraction to the electrodes and mitigates the buildup of photogenerated charges at the c-Si/PEDOT:PSS interface, as shown in Fig. 3.10(b).

In summary, we report the effect of inserting a ultrathin P(VDF-TeFE) layer at the c-Si/PEDOT:PSS interface on the photovoltaic performance of a c-Si/PEDOT:PSS Schottky junction solar cell. The electric field induced by the 3nm thick FE polymer films significantly increased the device efficiency, from 10.3% without the FE layer to 12.3% after thermal annealing followed by poling of the FE layer. This layer insertion, annealing, and poling process also increased the $V_{oc}$ of the device.

## 3.4 Summary

In this chapter, we invested the effects of guest material application in c-Si/PEDOT:PSS hybrid solar cells. At first, the effects of $MoO_3$ molecular doping in poly(3,4-ethylenedioxythiophene): poly(stylenesulfonate) (PEDOT:PSS) on the chemical structure and, in turn, on the carrier collection efficiency of c-Si/PEDOT:PSS heterojunction solar cells are demonstrated. Scanning electron microscopy revealed that the hydrophilic PSS polymer chain was intercalated into the interlayer Van Der Waals gap of $MoO_3$ flake sheets, which modified the chemical structure of PEDOT:PSS. $MoO_3$ exhibited intense photoluminescence in the 350~550nm region, which enhanced the carrier collection efficiency of c-Si/PEDOT:PSS heterojunction solar cells with no significant changes. These findings suggest that the intense photoluminescence of $MoO_3$ and its light wavelength conversion contribute to the increased carrier collection efficiency.

In the latter part, the effect of inserting an ultrathin layer of ferroelectric (FE) poly(vinylidene fluoridetetrafluoroethylene) P(VDF-TeFE) at the crystalline c-Si/PEDOT:PSS interface of a c-Si/PEDOT:PSS Schottky junction solar cell is demonstrated.

P(VDF-TeFE) is a highly resistive material that exhibits a large, permanent, internal polarization electric field by poling of molecular dipole among the polymer chains. Because of these properties, performance can be enhanced by adjusting the thickness of the FE layer and subsequent poling process. Inserting a 3nm thick FE layer increases the power conversion efficiency g from 10.2% to 11.4% with a short-circuit current density $J_{sc}$ of 28.85mA/cm$^2$, an open-circuit voltage $V_{oc}$ of 0.57V, and a fill factor *FF* of 0.692. Subsequent poling of the FE layer under a reverse DC bias stress increased η up to 12.3% with a $J_{sc}$ of 29.7mA/cm$^2$, a $V_{oc}$ of 0.58V, and an FF of 0.71. The obtained results confirm that the spontaneous polarization of the FE layers is responsible for the enhancement of η, and that the polarization-based enhancement works if the FE layer is highly crystalline. These findings originate from efficient charge extraction to the electrodes and a suppression of non-radiative recombination at the c-Si/PEDOT:PSS interface.

# Chapter 4

# Efficient Poly-crystalline Silicon/PEDOT: PSS Hybrid Solar Cells

## 4.1 Motivation

Solar cells based on the crystalline silicon offer high efficiency of 25.6%, but they are expensive due to the high temperatures required in their fabrication. The alternative approach using low-temperature processable organic photovoltaics (OPV) is potentially cheaper, but the organic solar cells are not very efficient. In our former work, we explore if organic semiconductor can be integrated with silicon to form hybrid organic/silicon solar cells that are both efficient and low-cost. Specifically, we demonstrate that a solution-processed organic/silicon heterojunction can replace the conventional silicon p-n junction to form solar cells with high power conversion efficiencies (>12%).

On the other hand, we exhibit the employment of poly-crystalline silicon (p-Si) which is more cost-effective, instead of expensive c-Si substrates. Here the big problem for application of p-Si is high defect density due to lots of grain boundaries, thus, initial device which employed the pristine p-Si substrates did achieved efficiencies below 6%.

To overcome this, defect passivation is needed to suppress trap states density like dangling bond at grain bound interface. In this chapter, we demonstrate efficient photovoltaic performance of conductive PEDOT:PSS/n-type poly-Si heterojunction solar cells showing a relatively high η of 9.8% in terms of defect termination of poly-Si wafer and the uniform deposition of PEDOT:PSS on poly-Si using CMD.

## 4.2 Passivation of Defects in Grain Boundaries Using High Pressure Water Vapor Treatment for Enhanced Device Efficiency

As it is mentioned before, the big problem for application of p-Si is high defect density due to lots of grain boundaries, thus, initial device which employed the pristine p-Si substrates did achieved low efficiencies resulted by terrible fill-in factor value. To overcome this, surface passivation is needed to suppress defect density like dangling bond at grain bound interface.

Figure 4.1 shows the schematic of the PEDOT:PSS/poly-Si heterojunction solar cells. Inset shows the SEM image of 100-nm-thick CMD PEDOT:PSS on poly-Si. N-type poly-Si wafer with a resistivity of 1-3 Ω·cm and a thickness of 180 μm was used in this study. Poly-Si wafers were pre-treated by high-pressure $H_2O$ vapor at 1.6 GPa, 200 ℃

for 2h to terminate dangling bond defects by oxygen at the grain boundary . Following that they were dipped in 5% hydrofluoric (HF)

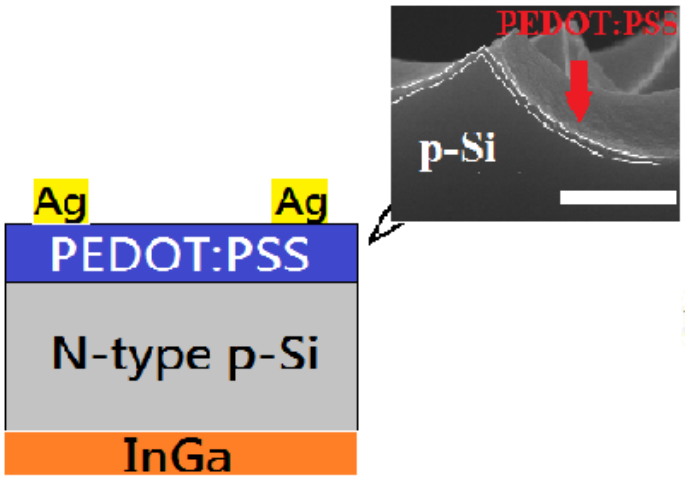


FIG 4.1 Schematic of the PEDOT:PSS/poly-Si heterojunction solar cells. Inset shows the SEM image of 100-nm-thick CMD PEDOT:PSS on poly-Si. Scale bar in the inset is 1μm

acid to remove surface oxidized layer. Highly conductive 5% by weight dimethyl sulfoxide (DMSO) and 0.1wt% Zonyl fluorosurfactant added commercialized PEDOT:PSS (Clevios PH1000) was used as a starting material. Films were deposited by two different methods, i.e, spin coating and CMD. Figure 4.2 shows a schematic of the experimental setup for the CMD. It consists of ultrasonic atomization reactor, quartz tube, mesh electrode to supply DC bias for charging mist deposition precursor, and substrate stage. Aqueous solution of PEDOT:PSS was sealed in the

reactor set on the ultrasonic vibrator of 3 MHz. Aqueous solution of 5 wt% dimethyl sulfonate (DMSO) added conductive PEDOT:PSS with DI

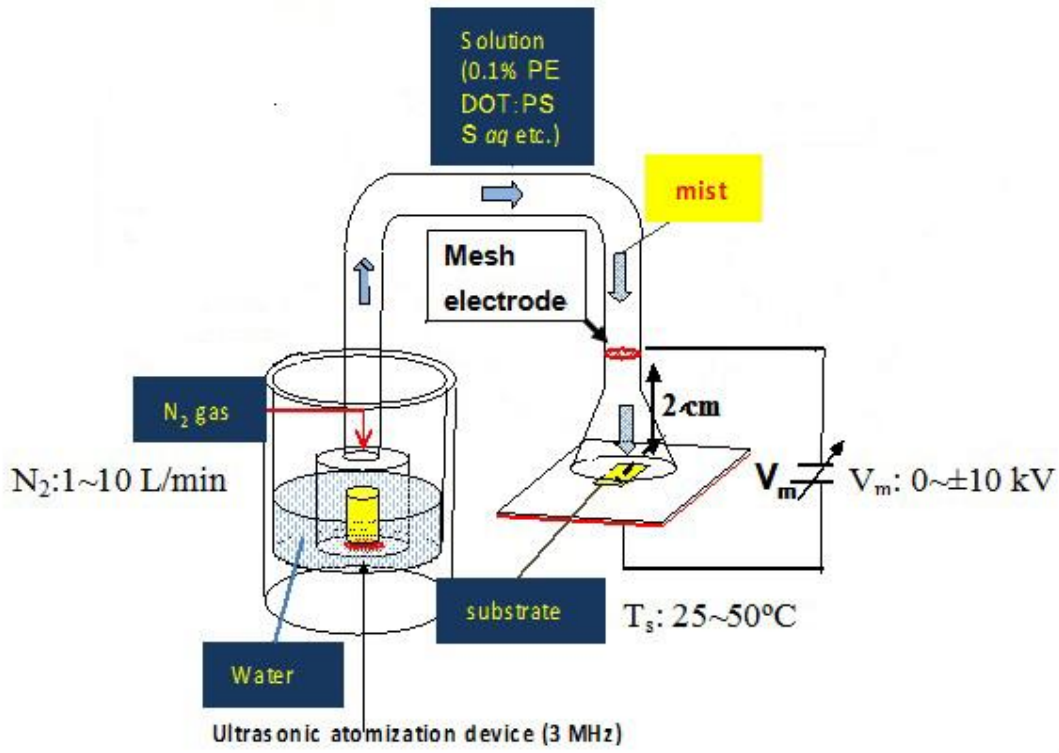


FIG 4.2 Schematic of the conversional CMD setup.

water and ethylene glycol (10 wt%) mixture using water and EG as co-solvents were set on the ultrasonic vibrator for the mist generation followed by thermally annealed to remove residual solvent at 140˚C for 30 min. The mist of PEDOT:PSS transported to the quartz tube using a $N_2$ as a carrier gas of 2 SLM and pass through the mesh electrode set 3cm away from substrate stage. The film deposition was performed with mesh DC bias of -5kV and a substrate temperature $T_s$ of 40 ℃. The film deposition rate was around 10nm/min. After that, the top Ag grid

electrode (0.1mm finger, 1mm bas bar) was formed using silver paste by screen printer. Finally, InGa alloy was used to make an ohmic contact as a rear electrode. As a comparison, spin-coated device was also fabricated by using 0.01% Zonyl fluorosurfactant added PEDOT:PSS onto HF-treated poly-Si wafer at 1000rpm for 60s and subsequent annealing at 140℃ for 30min. PEDOT:PSS films were characterized by atomic force microscopy (AFM/DFM: Seiko Instruments SPA-300/SPI-3800), micro Raman imaging spectroscopy (Renishaw), Fourier-transform infrared spectroscopy (FTIR). The current density-voltage (*J*-V) characteristics in the dark and under illumination of AM1.5G, 100mW/cm$^2$ simulated solar light (Bunkoukeiki CEP-25BX) was measured using solar cell device structure. The capacitance-voltage (*C*-V) and *C-f* (*f*: measurement frequency) were also measured to understand the carrier transport property at the PEDOT:PSS/poly-Si interface. In addition, the 2-dimensional map of photovoltaic parameters, $J_{sc}$ and external quantum efficiency (EQE) for devices (~2×2cm$^2$) were measured using line illumination scan and computer tomography calculation (MAP Lasertec Co Ltd).

Figure 4.3 shows FTIR spectra of poly-Si wafer after high-pressure $H_2O$ vapor treatment and subsequent 0.5% HF treatment. The spectra are shown referred to that of non-treated wafer as a reference. The Si-O-Si and SiO related peaks appeared at 800-1250 cm$^{-1}$ region, implying that

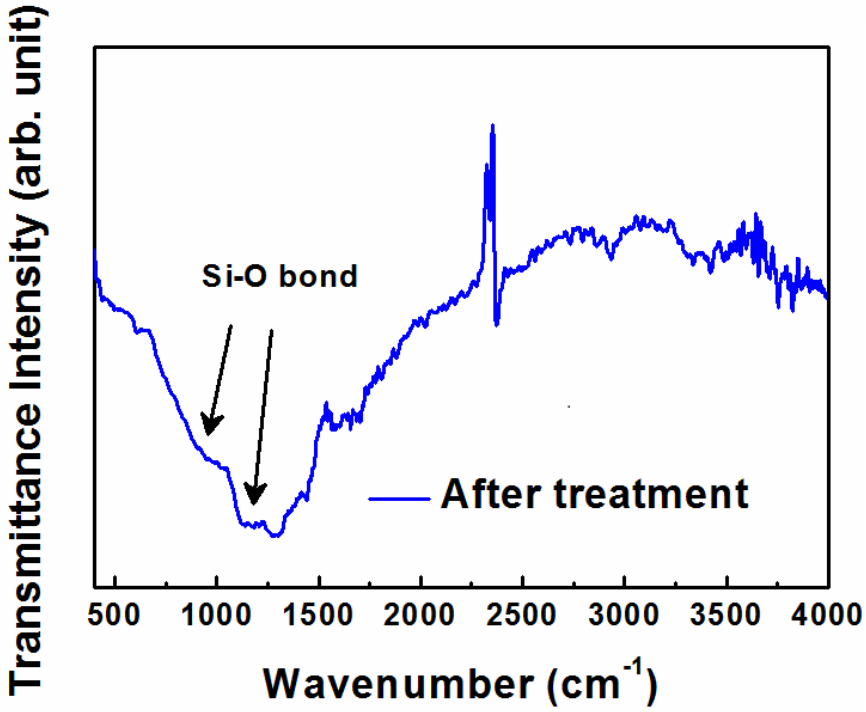


FIG 4.3 shows FTIR spectra of poly-Si wafer after high-pressure $H_2O$ vapor treatment and subsequent 5% HF treatment

the oxygen is incorporated into film and some of them contribute to the termination of dangling bond at the grain boundary in poly-Si. In Fig 4.4, the $1/C^2$-V plot at 1 MHz and *C-f* (*f*: measurement frequency) characteristics of Ag(1mmΦ)/PEDOT:PSS/poly-Si diode are shown using spin-coated and CMD, respectively. It was found $1/C^2$-V plot of the device yielded by non-treated p-Si substrates couldn't align the typical lineal relationship due to large trap states resulted by defect around grain boundaries region. The built-in potential $V_b$ and donor density $N_d$ were over 3V and $4\times10^{17}$ $cm^{-3}$ for the pristine diode, whereas $V_b$ and $N_d$ were 0.7-1.1 V and $\sim1\times10^{16}$ $cm^{-3}$, respectively for the high pressure water

vapor treated device, despite of spin coating or CMD fabrication process. The slope of the $1/C^2$-V plot relating to ($1/N_d+1/N_a$: $N_a$ accepter density) was lower for the high-pressure $H_2O$ vapor treated diode than that of non-treated one suggesting that the $N_a$ in the organic increased.

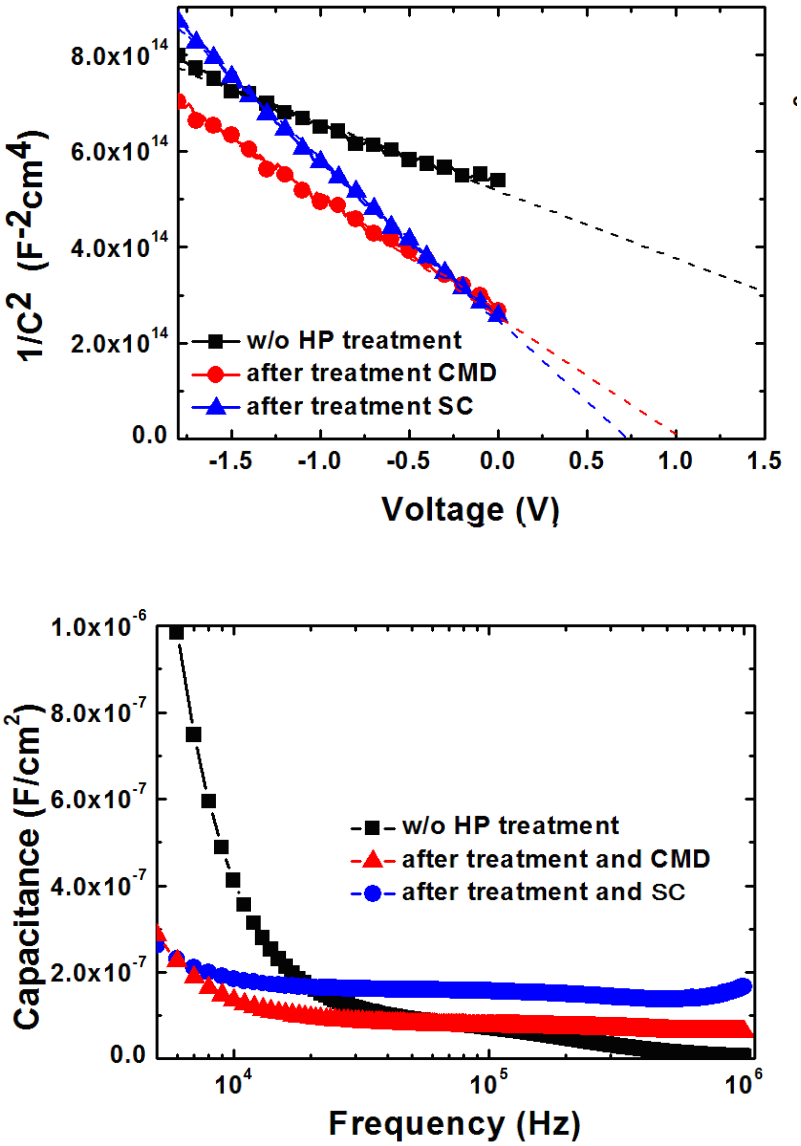


FIG 4.4 $1/C^2$-V plot at 1 MHz (top) and $C$-$f$ ($f$: measurement frequency) characteristics of Ag(1mmΦ)/PEDOT:PSS/poly-Si diode using

spin-coated and CMD, respectively

In addition, the junction capacitance was almost independent of *f* and it was suppressed to be lower for the lower measurement-frequency range for the high-pressure $H_2O$ vapor treated diode. These imply the dangling bond defect is terminated by oxygen as Si-O-Si.[7]

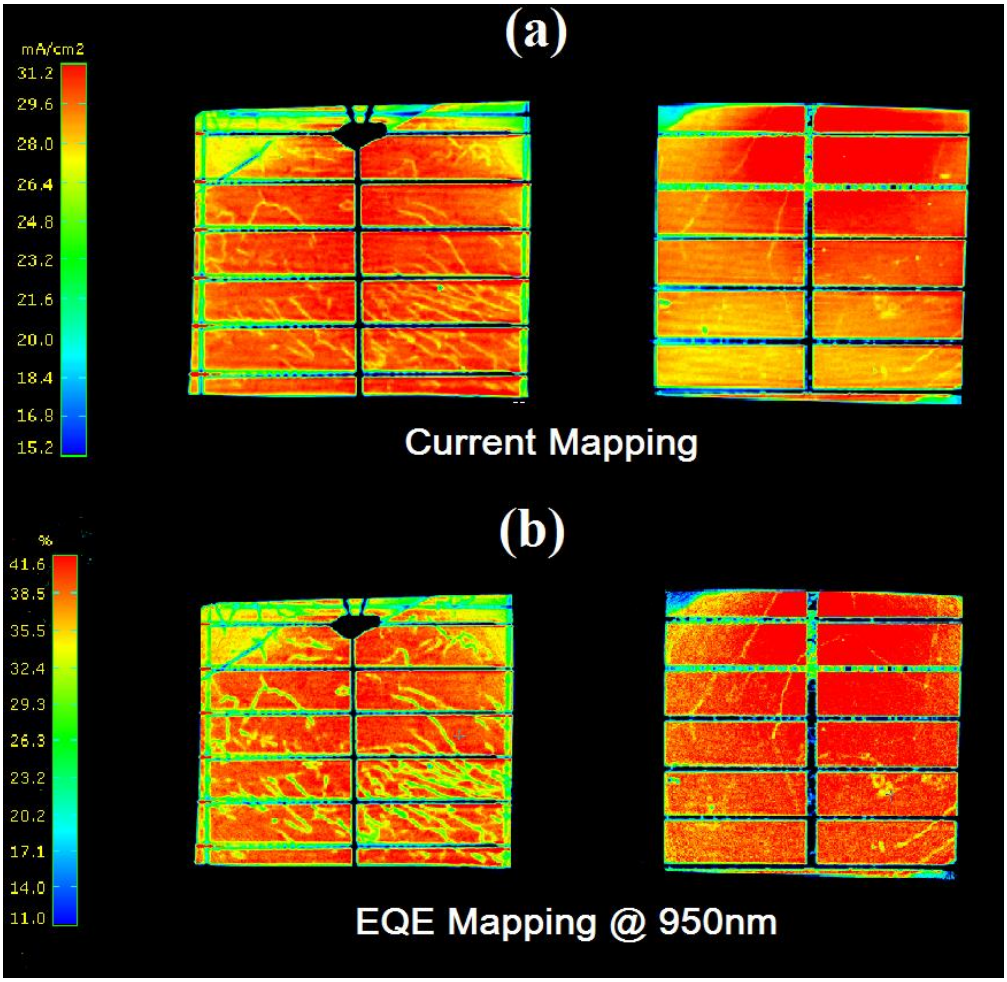


FIG 4.5 The 2D-dimensional map within 2×2 $cm^2$ area of (a) short-circuit current density $J_{sc}$ and (b) external quantum efficiency EQE at 950 nm of corresponding PEDOT:PSS/poly-Si heterojunction solar cells

Figure 4.5 shows the 2D-dimensional map within $2 \times 2$ $cm^2$ area of short-circuit current density $J_{sc}$ and external quantum efficiency EQE at 950 nm of corresponding PEDOT:PSS/poly-Si heterojunction solar cells. The fine structures attributed to the defect of poly-Si wafer such as twin boundary, dislocation, and screw transition in poly-Si wafer was clearly observed for non-treated poly-Si wafer, whereas such fine structures disappeared for the treated one. These findings imply that high-pressure $H_2O$ vapor treatment is a possible method to suppress defect density of poly-Si wafer.

## 4.3 poly Si/PEDOT:PSS hybrid solar cells using CMD deposition to yield uniform coating

As it was been discussed previously, simple spincoat process is unable to yield an uniform deposition of PEDOT:PSS thin films on rough Si surface like textured/nano-pillar substrates. In this study, p-Si wafer we employed was been treated by conventional chemical wet-etching process, thus roughness around μm was been formed. This resulted in the nonuniform deposition of PEDOT:PSS thin film on such p-Si wafers. To overcome this issue, CMD deposition technic have been employed to investigate the p-Si/PEDOT:PSS hybrid solar cell performance with uniform coating of PEDOT:PSS.

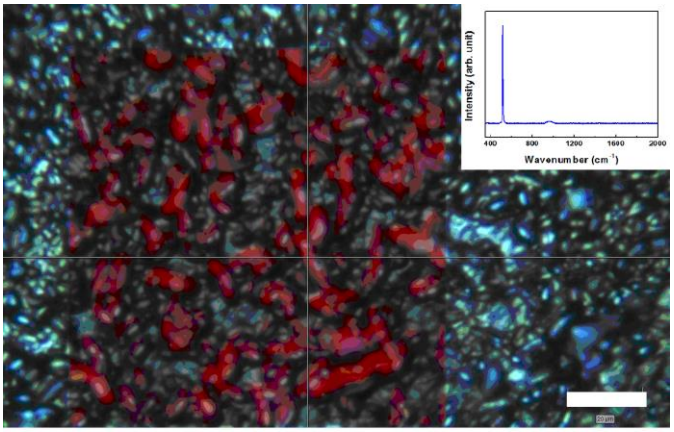


(a)

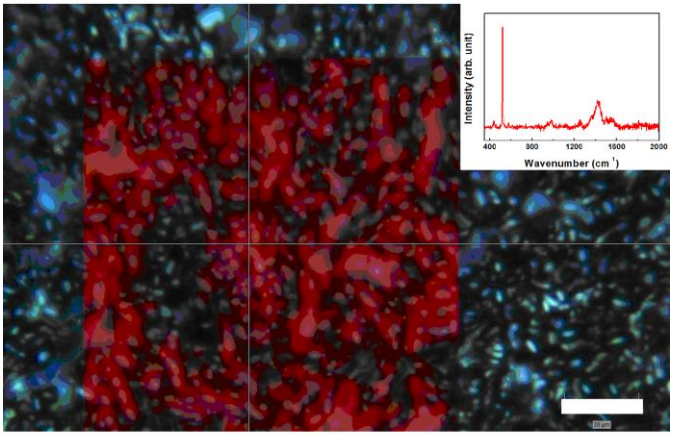


(b)

FIG 4.6 Optical micrograph and 2D Raman map combination of (a) spin-coated and (b) CMD deposited PEDOT:PSS films on high-pressure $H_2O$ treated poly-Si. Inset shows the Raman spectra of film measured at two different regions.

Figure 4.6 shows the in-plane optical micrograph and 2D map of Raman intensity at 1300-1500 $cm^{-1}$ corresponding to C=C bond of PEDOT for 100-nm-thick spin-coated and CMD deposited PEDOT:PSS

films on high-pressure $H_2O$ treated poly-Si. Inset shows the Raman spectra of film measured at two different regions. The distribution of Raman peak for spin-coated PEDOT:PSS was inhomogeneous due to the inhomogeneous film thickness, whereas the CMD PEDOT:PSS was relatively homogeneous. These findings suggest that negatively charged mist mainly contribute to the uniform deposition of film on poly-Si.

The *J*-V characteristics under illumination of AM1.5G 100mW/cm$^2$ simulated solar light spectra at several positions are shown in Fig. 4.7 for the spin-coated and CMD deposited PEDOT:PSS/poly-Si heterojunction devices. The average photovoltaic parameters, i.e., open-circuit voltage $V_{oc}$, short-circuit current density $J_{sc}$, fill factor *FF*, and η are summarized for the devices in Table 4.1.

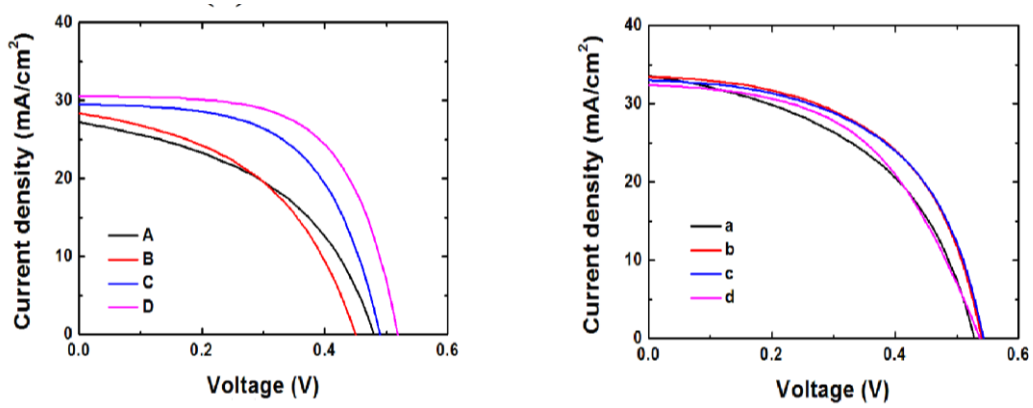


FIG 4.7 The *J*-V characteristics in the dark and under illumination of AM1.5G 100mW/cm$^2$ simulated solar light spectra at several positions for the (left) spin-coated and (right) CMD deposited PEDOT:PSS/poly-Si heterojunction devices

As the results shown, average efficiency of p-Si/PEDOT:PSS hybrid solar cell was been promoted dramatically in case of CMD fabricated samples compare with that of spincoated devices. Especially the short-circuit current density $J_{sc}$ improved from ~30mA/cm$^2$ to 33mA/cm$^2$, which implies the more sufficient carrier collection, due to enhanced uniformly coating (as shown in Fig 4.6) of PEDOT:PSS on p-Si surface and yielded larger PEDOT:PSS/p-Si interface. In addition, higher $V_{oc}$ was observed for CMD devices. These findings imply that the carrier transport at the PEDOT:PSS/poly-Si interface is improved with a high pressure $H_2O$ vapor treatment and the use of CMD.

Band diagrams of p-Si/PEDOT:PSS hybrid solar cells with and without high pressure $H_2O$ vapor treatment are shown in Fig 4.8. As discussed before, FTIR result suggested passivation of defect at grain boundary is formed due to sufficient HP resulted Si-O bonding. Thus, trap states at p-Si/PEDOT:PSS hybrid junction interface should be sufficiently suppressed. This would lead to a lower quasi-Fermi lever which could enhance the built-in filed $\Phi_B$ of the diode. In addition, energy potential of both conduct band and valence band would also been smoothed which is able to promote the e/h transport for enhanced carrier separation.

| Device | $J_{sc}$(mA/cm$^2$) | $V_{oc}$(V) | *F.F.* | Eff (%) |
|---|---|---|---|---|
| CMD a | 33.6 | 0.53 | 0.48 | 8.5 |
| CMD b | 33.5 | 0.54 | 0.53 | 9.7 |
| CMD c | 33.0 | 0.54 | 0.54 | 9.6 |
| CMD d | 32.4 | 0.54 | 0.51 | 8.8 |
| SC a | 27.2 | 0.48 | 0.46 | 5.9 |
| SC b | 28.4 | 0.45 | 0.46 | 5.9 |
| SC c | 39.5 | 0.49 | 0.58 | 8.4 |
| SC d | 30.5 | 0.52 | 0.62 | 9.8 |

TABLE 4.1 Performance details of the spin-coated and CMD deposited PEDOT:PSS/poly-Si heterojunction devices, measured at four different region.

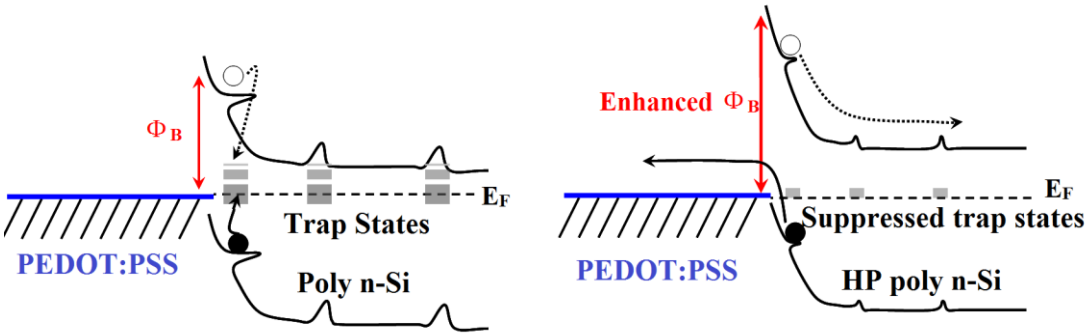


FIG 4.8 Band diagram of p-Si/PEDOT:PSS hybrid solar cell. Left shows the schematic band structure of device with non-HP-treated p-Si substrates, whereas right one means HP-treated samples.

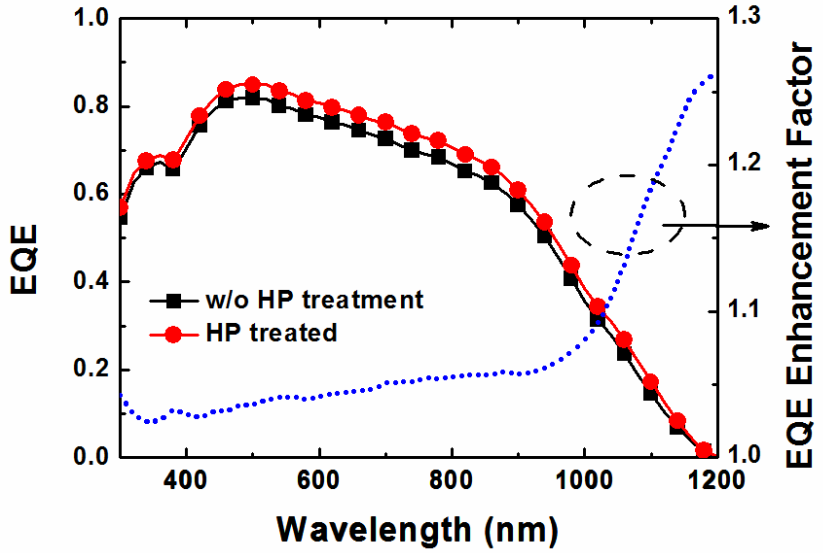


FIG 4.9 EQE spectra of p-Si/PEDOT:PSS hybrid solar cell yielded by p-Si substrates with and without HP treatment. The calculated EQE enhancement factor is shown as well.

Fig 4.9 shows the EQE spectra of p-Si/PEDOT:PSS hybrid solar cell yielded by p-Si substrates with and without HP treatment. The calculated EQE enhancement factor is shown as well. Here, EQE enhancement factor＝$EQE_{wHP}/EQE_{w/oHP}$. It is found photo response of device with HP treatment is been promoted in entire region from 300nm to 1200nm. Nevertheless, as the EQE enhancement factor shows, photo response properties at infrared region is been enhanced dramatically. Such improvement of carrier collection efficiency in infrared region is mainly due to suppressed energy potential of both conduct band and valence band resulted by sufficient passivation of trap states. Thus, e/h transport is been promote which leads to the enhanced carrier collection.

## 4.4 Conclusion

In summary, we have investigated the photovoltaic performance of PEDOT:PSS/n-type poly-Si heterojucntion solar cell devices. The high pressure $H_2O$ vapor treatment of poly-Si prior to the film deposition of organic promoted the reduction of dangling bond defects incorporated into poly-Si, resulting in the enhanced carrier collection efficiency at 850-1100 nm region. The chemical mist deposition of conductive PEDOT:PSS combined with negative DC bias supply improved significantly the adhesion of PEDOT:PSS on hydrophilic poly-Si wafer. As a consequence, a highly efficient PEDOT:PSS/poly-Si heterojunction solar cell was obtained with the highest power conversion efficiency of 9.8% with a $J_{sc}$ of 33 mA/cm$^2$, a $V_{oc}$ of 0.54 V, and a *FF* of 0.55. Such organic/poly-Si heterojunction cells can potentially further deliver high FF and conversion efficiency combining with the creation of ohmic junction at the rear surface.

# Chapter 5

# Conclusions and Future Work

## 5.1 Summary of Results

In this thesis we discussed the use of silicon/organic heterojunctions for photovoltaic applications. Crystalline-silicon based photovoltaics is a high-performance technology but the costs associated with the multiple high-temperature steps and low-throughput equipment makes silicon solar cells expensive to manufacture. Organic semiconductors are purported to be a low-cost alternative to conventional inorganic semiconductors but the performance of organic solar cells is very poor. The goal in this project was to integrate low-cost organic semiconductors on high-performance crystalline silicon to demonstrate low-cost high-performance solar cells. The key contributions of this work are:

a). The uniform coating of PEDOT:PSS thin films on hydrophobic Si substrates

In this work, commercialized highly conductive ink (Clevios PH1000) was used as precursor to form transparent hole transport layers on n-type silicon by simple spin-coating process, and a big problem here is the

uniform coating of aqueous solution on the hydrophobic H-terminated Si surface. We demonstrate the usage of 0.1wt% Zonyl fluorosurfactant (Dupont) as an additive into PEDOT:PSS improved the adhesion of precursor solution on hydrophobic c-Si wafer. The average power conversion efficiency value was 11.3%, which was superior to those of non-treated devices. The Zonyl-treated soluble PEDOT:PSS composite is promising as a hole-transporting transparent conducting layer for c-Si/organic heterojunction(SOH) photovoltaic applications.

b). Optical anisotropy in PEDOT:PSS and its effect on the photovoltaic performance of SOH solar cells

In this topic, we demonstrated the effect of uniaxial optical anisotropy on the photovoltaic performance of c-Si/organic heterojunction solar cells produced by spin coating using either a MeOH solvent or MeOH and EG cosolvents. The systematic study of corresponding samples via spectroscopy ellipsometry implied that the use of the co-solvents led to an increase in extraordinary index of refraction and a reduction in the film thickness which promoted densification of polymer chains network in the resulted PEDOT:PSS thin films. And this improvement of PEDOT:PSS fine structure due to co-solvent addition resulted in an increased hole mobility from 1.23 cm2/V.s to 3.92 cm2/V.s of the resulted samples. A solar cell fabricated using such a film exhibited a relatively high efficiency of 11.23%, with a substantial fill-in factor (FF) value of 0.71.

c). Employment of guest materials for further improvement of SOH solar cells efficiencies

In addition, varieties of functional material like graphene oxide, molybdenum oxide flake sheet, ferroelectric polymer poly(vinyli- dene fluoridetetrafluoroethylene) P(VDF-TeFE) were employed as dopant to improve carrier transport properties in SOH diodes and go advantage the solar cell performance.

d). The photovoltaic performance of PEDOT:PSS/n-type poly-Si heterojucntion solar cell devices have been investigated. The high pressure $H_2O$ vapor treatment of poly-Si prior to the film deposition of organic promoted the reduction of dangling bond defects incorporated into poly-Si, resulting in the enhanced carrier collection efficiency at 850-1100 nm region. The chemical mist deposition of conductive PEDOT:PSS combined with negative DC bias supply improved significantly the adhesion of PEDOT:PSS on hydrophilic poly-Si wafer. As a consequence, a highly efficient PEDOT:PSS/poly-Si heterojunction solar cell was obtained with the highest power conversion efficiency of 9.8% with a $J_{sc}$ of 33 mA/cm$^2$, a $V_{oc}$ of 0.54 V, and a *FF* of 0.55. Such organic/poly-Si heterojunction cells can potentially further deliver high FF and conversion efficiency combining with the creation of ohmic junction at the rear surface.

## 5.2 Future Work

## Improving Efficiency of Silicon/PEDOT:PSS Hybrid Solar Cells

The power conversion efficiency of silicon/organic heterojunction can be further increased by incremental improvements in the design of the present Si/PEDOT:PSS hybrid solar cell. A set of possible approaches are shown as following:

### Improvement of Short-Circuit Current

In case of pristine SOH device, the short-circuit current is around 29 $mA/cm^2$, lower than ~40$mA/cm^2$ achieved in the typical Si p-n junction solar cells. The primary reason for lower $J_{SC}$ is substantial top-surface reflection due to lack of light-trapping – there are no anti-reflection coating or surface texturing. Solution processed AR coatings using commercially available commercialized polymers can be used [106, 107]. However, in case of sufficient AR coating, the effective refraction index of materials should be considered, since its ~1.5 for PEDOT:PSS and ~3.5 for silicon, thus AR materials with refraction index between 1.5 and

3.5 could be employed. Another option is combine textured light-harvesting structure, like plastic films on top of the silicon/organic heterojunction solar cell using optical adhesives, using anisotropic etchants, to increase carrier absorption in silicon [108~110]. Another possibility is improvement of PEDOT:PSS thin film transmittance, which could promote $J_{SC}$ values. On the other hand, to reduce absorption losses in the top electrode, more transparent and more conductive electrodes can be used, like ITO or AZO [111]. However, it is possible the sputtered metal-oxide causes many mechanical damage on the underlying PEDOT:PSS films, in this case, solution-processed ZnO [112, 113] and ITO [114] films could be used. Finally, nanowire metallic meshes can be used to increase the conductivity of top electrode [115], for further improvement of contact resistance.

Secondly, employment of light-trapping like periodical nanoarray structure (Fig 5.1) is also a hopeful approach for enhancing SOH solar cell efficiency. In our recent work, the SOH device with both side textured Si substrate obtained an excellent *J*sc of 38mA/cm$^2$, which is similar with typically produced c-Si based solar cell. Nevertheless, solar cell efficiency was still not sufficient, due to following two items: 1), nonuniform coating of PEDOT:PSS thin films on quite rough textured Si substrates by simple spin-coating process, thus, photo-generated carrier could not been collected efficiently; 2), serious carrier recombination at

Si/PEDOT:PSS interface resulted by enhanced defect density. To overcome the first problem, we tried to employ Chemical Mist Deposition (CMD) technique which is suitable for uniform coating of solution precursor despite of substrates roughness. At present, we need to optimize the mist deposition parameters like substrate temperature, charge mesh bias, transport gas fluid for depositing high quality PEDOT:PSS thin films. Solution for the next issue requests to observe sufficient surface passivation of Si substrates, similar with previous demonstration.

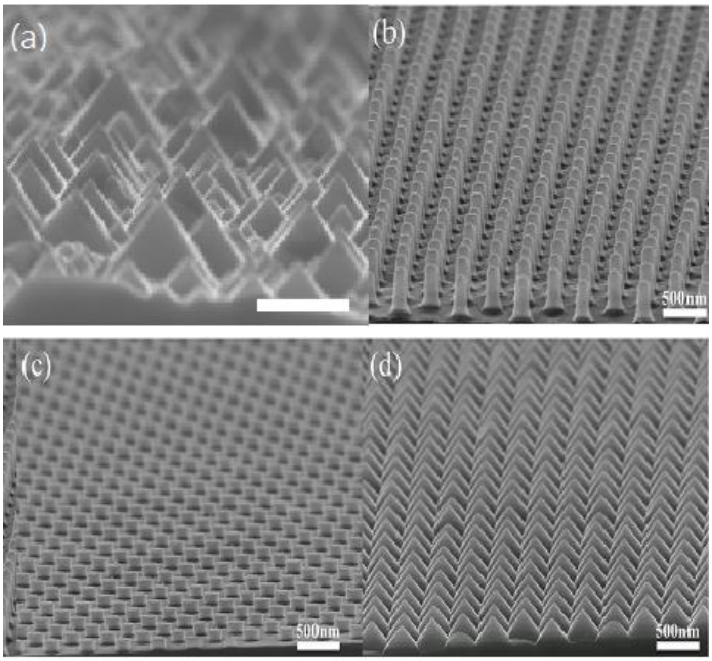


FIG 5.1 SEM images of (a) textured and (b), (c), (d) (cooperation with NCTU) imprinted nano-pyramidal Si substrates (APPLIED PHYSICS LETTERS 103, 133901, 2013).

## Increasing the Fill Factor

The fill factor of pristine silicon/organic heterojunction cell is still around 0.7, which is much smaller than typical Si solar cell, mainly due to the ohmic losses in the organic films and its conduction with electrodes. Additional post solvent dipping treatment like DMSO, $H_2SO_4$, isopropyl alcohol, etc. is a well-known method of promoting PEDOT conductivity [116]. Series resistance can also be reduced by yielding an idea ohmic contact at cathode.

## Increasing the Open-Circuit Voltage

Concerning the band diagram of Si/PEDOT:PSS heterojunction solar cell (Fig 5.2), open circuit voltage of such device is mainly determined by the off-set between PEDOT:PSS work function and Fermi lever of n-type

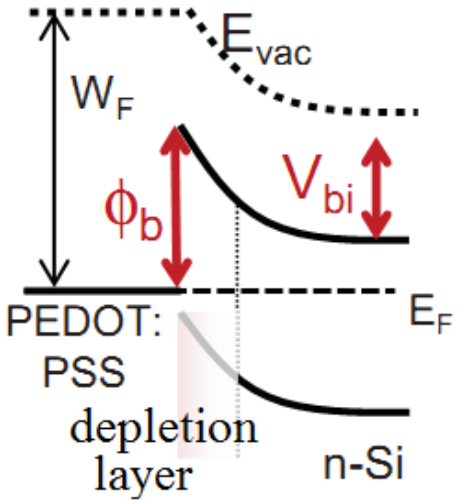


FIG 5.2 Band diagram of Si/PEDOT:PSS hybrid solar cell

Si substrate. According to the C-V measurement, built-in potential of n-Si/PEDOT:PSS heterojunction is about 0.79V, which is quite higher than open circuit voltage of recent solar cell in our lab. These voltages lose mainly contributed in carrier recombination due to varieties of defect at Si/organic interface, such as dangling bond, trap states et al. This implies the further improvement of solar cell efficiency, especially the Voc, can be expected by sufficient surface passivation.

In addition, another approach for higher Voc is band alignment to generate larger built-in potential, just like what researchers wisely did in HIT (heterojunction with an intrinsic thin layer) solar cells. In our work, we are also able to use amorphous silicon (a-Si) thin layer to obtain excited Voc. As a beginning try, we have achieved solar cell with a Voc of 0.75V resulted in the intercalated thin intrinsic a-Si films. However, at this stage the solar cell efficiency was still not sufficient due to relative

poor *FF*, and our next work will focus on how we can optimize the device fabrication process to get sufficient efficiency.

# Appendix A

# Fabrication of SOH Devices

## A.1 PEDOT:PSS Precursor

Poly(3,4-ethylenedioxythiophene) poly(styrenesulfonate) (PEDOT:PSS) is a polymer mixture of two ionomers. One component in this mixture is made up of sodium polystyrene sulfonate which is a sulfonated polystyrene. Part of the sulfonyl groups are deprotonated and carry a negative charge. The other component PEDOT is a conjugated polymer and carries positive charges and is based on polythiophene. Together the charged macromolecules form a macromolecular salt. It is used as a transparent, conductive polymer with high ductility in different applications.[117] For example, AGFA coats 200 million photographic films per year with a thin, extensively-stretched layer of virtually transparent and colorless PEDOT:PSS as an antistatic agent to prevent electrostatic discharges during production and normal film use, independent of humidity condition. Fig. A.1 shows the chemical structure of conventional PEDOT:PSS.

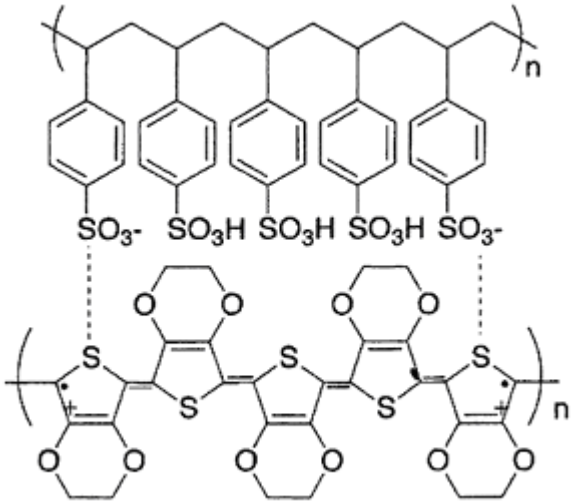


Fig. A.1 Chemical Schematic of PEDOT:PSS

If high boiling solvents like methylpyrrolidone, dimethyl sulfoxide, sorbitol are added conductivity increases many orders of magnitude which makes it also suitable as a transparent electrode, for example in touchscreens, organic light-emitting diodes and electronic paper to replace the traditionally used indium tin oxide.[122-126] Due to the high conductivity (over 1000 S/cm is expectable), it can be used as a cathode material in capacitors replacing manganese dioxide or liquid electrolytes. This compound is generally applied as a dispersion of gelled particles in water. A conductive layer on glass is obtained by spreading a layer of the dispersion on the surface usually by spin coating and driving out the water by heat. Special PEDOT:PSS inks and formulations were developed for different coating and printing processes. Aqueous PEDOT:PSS inks are mainly used in spray-coating, flexography, rotogravure and inkjet printing. If a high viscous paste and gentle drying is required like in case of screen-printing processes, PEDOT:PSS can also

be supplied in high boiling solvents like propanediol et.al. Solid PEDOT:PSS pellets can be produced with a freeze drying method which are redispersable in water and different solvents, for example ethanol, to increase drying speed during printing. Finally, to overcome degradation to ultraviolet light and high temperature/humidity conditions PEDOT:PSS UV-stabilizers are available. Commercially available PEDOT:PSS products are produced by Heraeus with the trade name Clevios ™ and by AGFA with the trade name Orgacon ™. Here, the commersialized Clevios™ PH1000 is used in this study.

## A.2 Cleaning of c-Si substrates

It is well known that there is a native oxide layer on c-Si surface, which will prohibit the carrier transport from n-type c-Si to p-type side in heterojunction solar cells. So the native oxide layer should be removed before p-type materials deposited on n-type c-Si substrate. Meanwhile, the dangling bond on the c-Si surface should be terminated by H or other atoms so that the defect density in interface would be suppressed at a low level. Usually the c-Si wafers are cleaned using standard RCA cleaning process in order to remove the native oxide layer.

The RCA clean processes are presented as following: [127]

(1) RCA1 cleaning at solution of $NH_4OH:H_2O_2$＝5:1 heated at 80℃

for 10 mins;

(2) HF dipping (5%, 1 min);

(3) $RCA_2$ cleaning at solution of HCl: $H_2O_2$＝5:1 heated at 80℃ for 10mins;

(4) HF dipping (5%, 1 min),

(5) Deionized water cleaning for 10 minutes.

It will take too long time over 30 minutes using RCA clean the c-Si wafer. In this study, RCA cleaning process is cut down only dip in HF solution.

## A.3 Deposition Methods

### A.3.1 Spincoating

Spincoating is a procedure used to form uniform thin films on flat substrates. An excess amount of a solution is placed on the substrate, which is then rotated at high speed in order to spread the fluid by centrifugal force. A machine used for spin coating is called a spin coater, or simply spinner. Rotation is continued while the fluid spins off the edges of the substrate, until the desired thickness of the film is achieved. The applied solvent is usually volatile, and simultaneously evaporates. So, the higher the angular speed of spinning, the thinner the film. The thickness of the film also depends on the concentration of the solution

and the solvent. Spin coating is widely used in micro-fabrication, where it can be used to create thin films with thicknesses below 10nm. It is used intensively in photolithography, to deposit layers of photoresist about 1 μm thick. Photoresist is typically spun at 1k to 5k RPM for 30 to 60 seconds. In this study, PEDOT:PSS thin films is deposited by spincoating of precursor solution on RCA-cleaned Si substrates.

## A 3.2 Chemical mist deposition method

The schematic of chemical mist deposition system is shown in figure A.2. The system is composed of solution heating system, gas transportation system and substrate heating system.

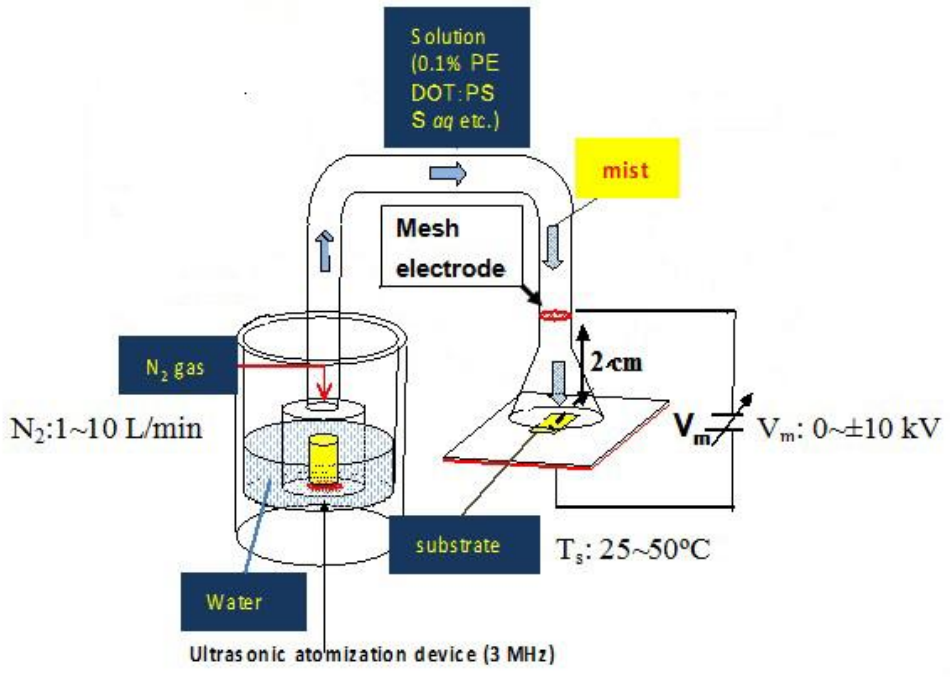


Fig. A.2 Schematics of Chemical Mist Deposition Systerm

In this system, the vaporization of organic solution (such as

PEDOT:PSS, GO etc ) is carried out through heating. The nitrogen ($N_2$), as a carry gas, carries the organic mist to the substrate. A direct current electric field is applied between the tube and substrate, the organic mist is deposited on the c-Si wafer. Then thermal annealing is performed to remove the residual solvent. In the deposition process, some parameters will influence the film deposition rate and uniformity. The influence of deposition time, applied electric field and distance between the anode and cathode on the film deposition rate is investigated. As the result been achieved, it is possible to control the thickness of organic thin film through adjusting the deposition time. The CMD is utilized for deposition of organic thin layer in this study. This technic is employed in chapter 4 to make an uniform deposition of PEDOT:PSS thin films on polycrystalline-Si substrates.

# Appendix B

# Characterization methods

## B.1 Spectroscopic ellipsometry (SE)

Ellipsometry is an optical technique for the investigation of the dielectric properties (complex refractive index or dielectric function) of thin films. It has applications in many different fields, from semiconductor physics to microelectronics and biology, from basic research to industrial applications [128-130]. Ellipsometry is a very sensitive measurement technique and provides unequalled capabilities for thin film metrology. As an optical technique, spectroscopic ellipsometry is non-destructive and contactless. Upon the analysis of the change of polarization of light, which is reflected off a sample, ellipsometry can yield information about layers that are thinner than the wavelength of probing incident, even as a mono atomic layer, Ellipsometry can probe the complex refractive index or dielectric function tensor, which gives access to fundamental physical parameters and is related to a variety of sample properties, including morphology, crystal quality, chemical composition, or electrical conductivity. It is commonly used to

characterize film thickness for monolayer or complex multilayer stacks ranging from a few angstroms or tenths of a nanometer to several micrometers with excellent accuracy. In this study, the SE spectrum is used to analyze the thickness and optical properties of resulted thin films like PEDOT:PSS, $SiO_X$, ferroelectric polymer et.al.

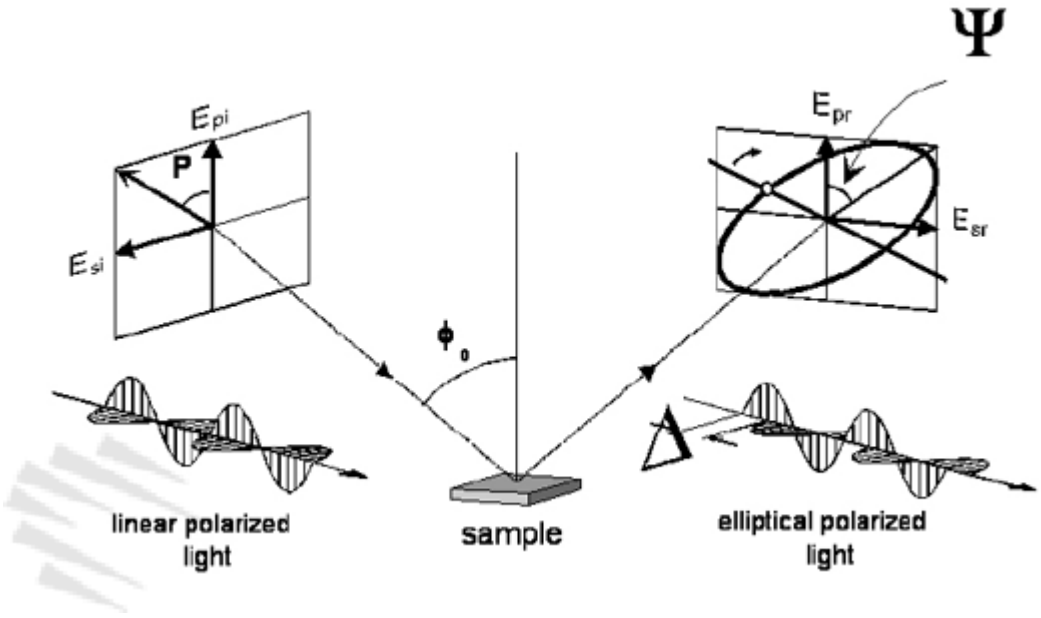


FIG A.3 Schematic setup of a conventional SE

## B.2 Atomic force microscope (AFM)

AFM is a very high-resolution type of scanning probe microscopy, with demonstrated resolution on the order of fractions of a nanometer. As shown in Fig. A.4, the AFM consists of a cantilever with a sharp tip (probe) at its end that is used to scan the sample surface [131]. The

cantilever is typically silicon or silicon nitride with a tip radius of curvature on the order of nanometers. When the tip is brought into proximity of a sample surface, forces between the tip and the sample lead to a deflection of the cantilever according to Hooke's law. Depending on the situation, forces that are measured in AFM include mechanical contact force, van der Waals forces, capillary forces, chemical bonding, electrostatic forces, magnetic forces (see magnetic force microscope, MFM), Casimir forces, solvation forces, etc. Along with force, additional quantities may simultaneously be measured through the use of specialized types of probe (see scanning thermal microscopy, scanning joule expansion microscopy, photothermal microspectroscopy, etc.). Typically, the deflection is measured using a laser spot reflected from the top surface of the cantilever into an array of photodiodes. Other methods that are used include optical interferometry, capacitive sensing or piezoresistive AFM cantilevers. These cantilevers are fabricated with piezoresistive elements that act as a strain gauge. Using a Wheatstone bridge, strain in the AFM cantilever due to deflection can be measured, but this method is not as sensitive as laser deflection or interferometry. Fig. A.4 shows an AFM image for pristine PEDOT:PSS films spin-coated on c-Si substrate. AFM is used to investigate the morphology of organic films. Fig. A.4 shows an AFM image for pristine PEDOT:PSS films spin-coated on c-Si substrate.

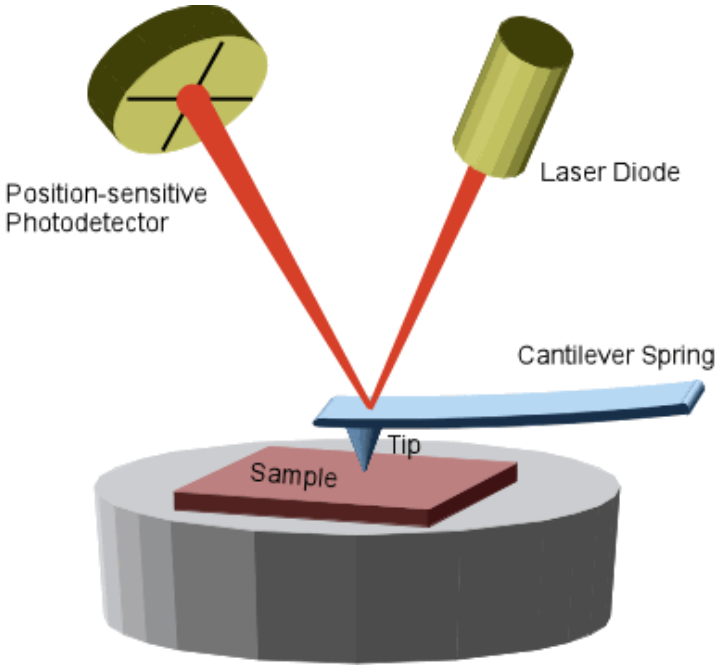


FIG A.4 Schematic of a typical AFM setup

## B.3 Spectrophotometer

Spectrophotometer gives a clear route to calculate the reflection or transmission properties of a material as a function of wavelength. Fig. A.5 shows the schematic of single light spectrophotometer. In this study, the optical transmittance and reflectance of corresponding films are measured by the spectrophotometer (Shimazu UV-2600).

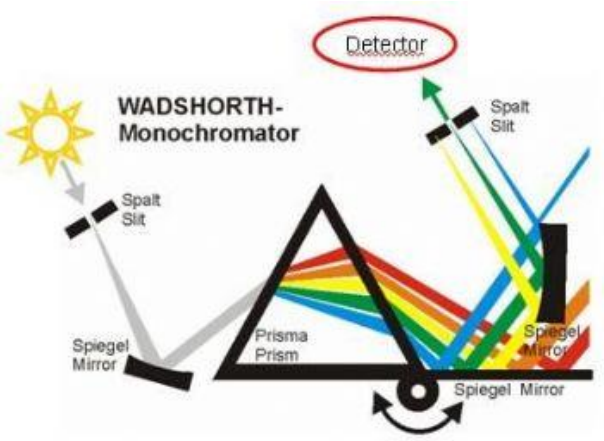


FIG A.5 the schematic of spectrophotometer

## B.4 Solar simulator

The *J*-V characteristics in the dark and under light illumination are measured using simulated solar light (AM1.5G, 100mW/cm$^2$, Bunkoukeiki CEP-25BX). The power conversion efficiency η was calculated as [132, 133]

$$\eta = V_{oc} J_{sc} FF / P_{in},$$

Here, $V_{oc}$ is the open circuit voltage, $J_{sc}$ is the short circuit current density, *FF* is the fill factor, and $P_{in}$ is the incident light power. *FF* is determined as $FF = (V_m J_m)/(V_{oc} J_{sc})$, where $V_m$ and $J_m$ are voltage and current density in the maximum power point of the *J*-V curves in the fourth quadrant (Fig A.6).

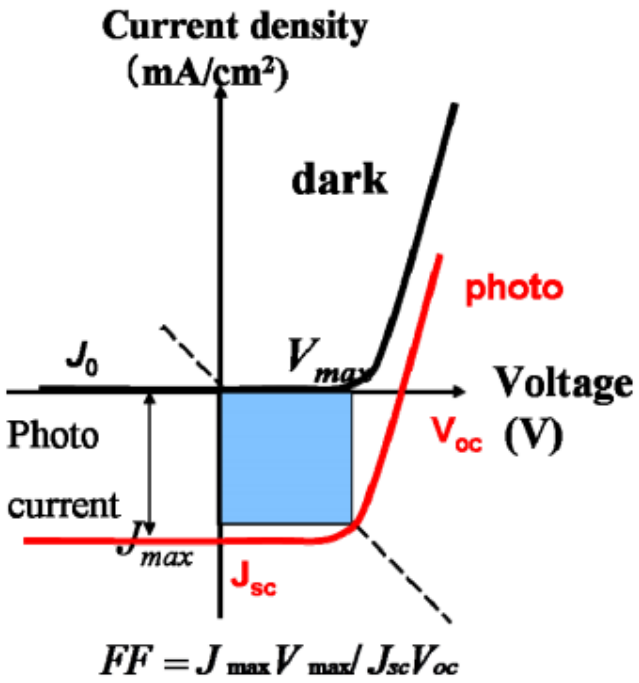


FIG A.6 the principle of J-V characteristics

## B.5 Capacitance-voltage characteristic

Assume the doping densities of p and n regions are $N_a$ and $N_d$, respectively. The capacitance per unit area may be derived from the total space charge Qs per unit area. Thus, we can write [134]:

$$C_j = \frac{dQ_s}{dV} = \frac{d(qN_a x_p)}{dV} = \frac{d(qN_d x_n)}{dV}$$

Assume that Na and Nd are constant and independent of the position, uses the relations $x_p=(N_d/N_a)x_n$ [135] and $W_d=x_n+x_p$ (shown in Fig A.7), then the capacitance can be derived as:

$$C_j = \sqrt{\frac{q\varepsilon_0\varepsilon_s}{2(1/N_d + 1/N_a)(V_{bi} - V)}}$$

For one side abrupt junction diode (i.e., $N_a >> N_d$), we can obtain:

$$C_j = \sqrt{\frac{q\varepsilon_0\varepsilon_s N_d}{2(V_{bi} - V)}}$$

In the same way, the transition capacitance for a linear-graded junction can be expressed by:

$$C_j = [\frac{qa(\varepsilon_0\varepsilon_s)^2}{12(V_{bi} - V)}]^{\frac{1}{3}}$$

Considering the area of the junction, the capacitance of the junction can be obtained:

$$C_j = A\sqrt{\frac{q\varepsilon_0\varepsilon_s N_a}{2(V_{bi} - V)}}$$

$$\text{or} \quad C_j = A[\frac{qa(\varepsilon_0\varepsilon_s)^2}{12(V_{bi} - V)}]^{\frac{1}{3}}$$

The inverse of the capacitance square varies linearly with the applied voltage V:

$$\frac{1}{C_j^{\,2}} = \frac{2}{A^2 q\varepsilon_0\varepsilon_s N_d} V_{bi} - \frac{2}{A^2 q\varepsilon_0\varepsilon_s N_d} V$$

The slope of the straight line yields the doping density, and the

intercept of the $1/C_j^2$ plot on the voltage axis gives the built-in potential $V_{bi}$ [136]:

$$slope = -\frac{2}{A^2 q \varepsilon_0 \varepsilon_s N_a}$$

$$\text{int}\, ercept = \frac{2}{A^2 q \varepsilon_0 \varepsilon_s N_a} V_{bi}$$

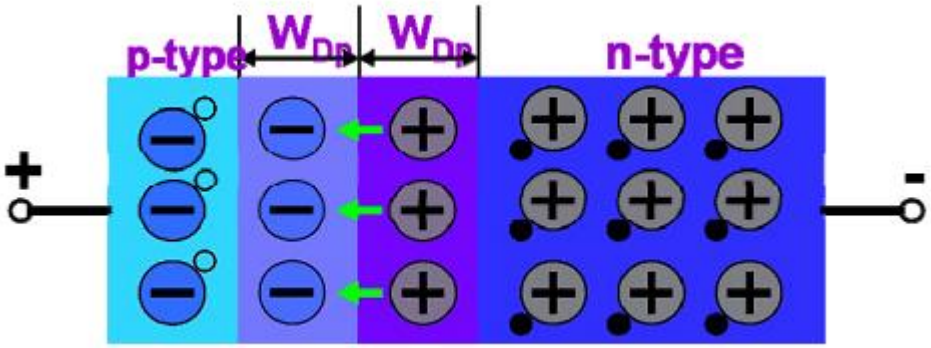


FIG A.7 Schematic of a typical p-n junction

# Publications

## Papers in Journals

1. **Qiming Liu**, Masahiro Ono, Zeguo Tang, Ryo Ishikawa, Keiji Ueno and Hajime Shirai, “Highly efficient crystalline silicon/Zonyl fluorosurfactant-treated organic heterojunction solar cells”, APPLIED PHYSICS LETTERS, 100, 183901, May, 2012

2. **Qiming Liu**, Ishiwor Khatri, Ryo Ishikawa, Keiji Ueno and Hajime Shirai, “Efficient crystalline Si/organic hybrid heterojunction solar cells ”, Physica Status Solidi C 9, No. 10-11, 2101-2106, September, 2012

3. **Qiming Liu**, Fumiya Watanabe, Aya Hoshino, Ryo Ishikawa, Takuya Gotou, Keiji Ueno and Hajime Shirai, “Crystalline Silicon/Graphene Oxide Hybrid Junction Solar Cells”, Japanese Journal of Applied Physics, 51, 10NE22, October, 2012

4. **Qiming Liu**, Ishiwor Khatri, Ryo Ishikawa, Keiji Ueno and Hajime Shirai, “Effects of molybdenum oxide molecular doping on the chemical structure of poly(3,4-ethylenedioxythiophene):poly(stylenesulfonate) and on carrier collection efficiency of silicon/ poly(3,4-ethylenedioxythiophene):poly(stylenesulfonate) heterojunction solar cells”, APPLIED PHYSICS LETTERS, 102, 183503, May, 2013

5. **Qiming Liu**, Takashi Imamura, Taiga Hiyate, Ishiwor Khatri, Zeguo Tang, Ryo Ishikawa, Keiji Ueno and Hajime Shirai, "Optical anisotropy in solvent-modified poly(3,4-ethylenedioxythiophene):poly (styrenesulfonic acid) and its effects on the photovoltaic performance of crystalline silicon/organic heterojunction solar cells", APPLIED PHYSICS LETTERS, 102, 243902, June, 2013

6. **Qiming Liu**, Ishiwor Khatri, Ryo Ishikawa, Atsuhiro Fujimori, Keiji Ueno, Kyohei Manabe, Hitoshi Nishino and Hajime Shirai, "Improved photovoltaic performance of crystalline-Si/organic Schottky junction solar cells using ferroelectric polymers", APPLIED PHYSICS LETTERS, 103, 163503, October, 2013

7. **Qiming Liu**, Tatsuya Ohki, Dequan Liu, Hiromitsu Sugawara, Ryo Ishikawa, Keiji Ueno and Hajime Shirai, "Efficient organic/polycrystalline silicon hybrid solar cells", Nano Energy, 11, 260, January, 2015

8. Ishiwor Khatri, Zeguo Tang, **Qiming Liu**, Ryo Ishikawa, Keiji Ueno and Hajime Shirai, "Green-tea modified multiwalled carbon nanotubes for efficient poly(3,4-ethylenedioxythiophene):poly (stylenesulfonate)/n-silicon hybrid solar cell", APPLIED PHYSICS LETTERS, 102, 063508, February, 2013

9. Tomohisa Ino, Masahiro Ono, Naoto Miyauchi, **Qiming Liu**, Zeguo Tang, Ryo Ishikawa, Keiji Ueno and Hajime Shirai, "Electrospray

Deposition of Poly(3-hexylthiophene) Films for Crystalline Silicon/Organic Hybrid Junction Solar Cells", Japanese Journal of Applied Physics, 51, 061602, June, 2012

10. Ishiwor Khatri, Zeguo Tang, Taiga Hiyate, **Qiming Liu**, Ryo Ishikawa, Keiji Ueno and Hajime Shirai, "Optical and carrier transport properties of graphene oxide based crystalline-Si/organic Schottky junction solar cells", JOURNAL OF APPLIED PHYSICS, 114, 234506, December, 2013

11. Taiga Hiyate, Naoto Miyauchi, **Qiming Liu**, Ryo Ishikawa, Keiji Ueno and Hajime Shirai, "Real-time measurement of optical anisotropy during film growth using a chemical mist deposition of poly(3,4-ethylenedioxythiophene):poly(stylenesulfonate)", JOURNAL OF APPLIED PHYSICS, 115, 123514, March, 2014

12. Ishiwor Khatri, Aya Hoshino, Fumiya Watanabe, **Qiming Liu**, Ryo Ishikawa, Keiji Ueno and Hajime Shirai, "Self-assembled silver nanowires as top electrode for poly(3,4-ethylenedioxythiophene): poly(stylenesulfonate)/n-silicon solar cell", Thin Solid Films, 558, 306, May, 2014

**Conference Presentation**

1. **Qiming Liu**, Tatsuya Ohki, Dequan Liu, Hiromitsu Sugawara, Ryo Ishikawa, Keiji Ueno and Hajime Shirai, "Efficient organic/polycrystalline silicon hybrid solar cells", The 6th World Conference on Photovoltaic Energy Conversion, (WCPEC6) (poster), Kyoto, Japan, Nov. 2014.

2. **Qiming Liu**, Tatsuya Ohki, Ryo Ishikawa, Keiji Ueno and Hajime Shirai, "Efficient organic/silicon heterojunction solar cells", Energy Materials Nanotechnology Open Access Week(EMN) (invited oral), Chengdu, China, Sept. 2014.

3. **Qiming Liu**, Ishwor Khatri, Atsushi Fujimori, Ryo Ishikawa, Keiji Ueno and Hajime Shirai, "Self-assemble Ferroelectric Nanoarray and Its Application to c-Si/PEDOT:PSS Schottky Junction Solar Cells", 23rd Photovoltaic Science and Engineering Conference(PVSEC23) (oral), Taipei, Taiwan, Nov. 2013.

4. **Qiming Liu**, Ishwor Khatri, Ryo Ishikawa, Keiji Ueno and Hajime Shirai, "Effects of molybdenum oxide molecular doping on the chemical structure of PEDOT:PSS and on carrier collection efficiency of c-Si/PEDOT:PSS heterojunction solar cells", 28th European Photovoltaic Solar Energy Conference(28th EU PVSEC) (oral), Paris, France, Oct. 2013.

5. **Qiming Liu**, Kyohei Ishikawa, Taiga Hiate, Keiji Ueno, and Hajime Shirai, “Optical anisotropy in solvent-modified PEDOT:PSS and its effect on photovoltaic performance of c-Si/PEDOT:PSS heterojunction solar cells”, The 6th International Conference on Spectroscopic Ellipsometry(ICSE6) (oral), Kyoto, Janpan, May. 2013

6. **Qiming Liu**, Zeguo Tang, Ishwor Khatri, Ryo Ishikawa, Keiji Ueno and Hajime Shirai, “Efficient c-Si/organic heterojunction solar cells use graphene oxide as a dopant”, 22nd Photovoltaic Science and Engineering Conference(PVSEC22) (oral), Hangzhou, China, Nov. 2012.

In addition, here I simply list the other international and/or domestic conferences I have presented: The 25th International Conference on Amorphous and Nano-crystalline Semiconductors(ICANS25) (1oral and 1poster), Toronto, Canada, Aug. 2013; JSAP- MRS Joint Symposia (oral) in Doshisha Univ. Kyoto, 2013; International Union of Materials Research Societies – International Conference on Electronic Materials(IUMRS-ICEM) (oral) in Yokohama, 2012 and JSAP spring meetings from 2012 to 2014.

# Reference

[1] L. Ma, “Development of Solar photovoltaic industry” [Online]. Available: http://www.csrc.gov.cn/pub/newsite/fxjgb/cybzxyjbg/201203/P020120330324607345098.pdf

[2] “$1/W photovoltaic systems: White paper to explore a grand challenge for electricity from solar,” U.S. Department of Energy, Tech. Rep., 2011.

[3] S. O'Rourke, P. Kim, and H. Polavarapu, “Solar photovoltaic industry -looking through the storm.” [Online]. Available: http://www.columbia.edu/cu/cures/Stephen-Oroukes-presentation2.pdf

[4] “Solar photovoltaic industry 2010 global outlook” [Online]. Available: http://solar.gwu.edu/index/files/Resources/files/SolarPVoutlookFITT8Feb10PDF.pdf

[5] P. Kim and H. Polavarapu, “Solar photovoltaic industry 2011 outlook- FIT cuts in key markets point to over-supply.” [Online]. Available: http://www.strategicsiliconservices.com/wp-content/uploads/2010/07/2011solarpvindustryoutlook.pdf

[6] M. A. Green, K. Emery, Y. Hishikawa, and W. Warta, Progress in Photovoltaics: Research and Applications, vol. 19, pp. 84, 2011.

[7] J. E. Anthony, Angewandte Chemie International Edition, vol. 47, pp. 452, 2008.

[8] J. R. Sheats, Journal of Materials Research, vol. 19, pp. 1974, 2004.

[9] J. Y. Kim, K. Lee, N. E. Coates, D. Moses, T.-Q. Nguyen, M. Dante, and A. J. Heeger, Science, vol. 317, pp. 222, 2007.

[10] F. C. Krebs and K. Norrman, Progress in Photovoltaics: Research and Applications, vol. 15, pp. 697, 2007.

[11] M. Jrgensen, K. Norrman, and F. C. Krebs, Solar Energy Materials and Solar Cells, vol. 92, pp. 686, 2008.

[12] M. J. Sailor, E. J. Ginsburg, C. B. Gorman, A. Kumar, R. H. Grubbs, N. S. Lewis, Science, vol. 249, pp. 1147, 1990.

[13] Q. Liu, Z. Tang, R. Ishikawa, K. Ueno, and H. Shirai, Appl. Phys. Lett. 100, 183901 (2012).

[14] Q. Liu, F. Watanabe, A. Hoshino, R. Ishikawa, T. Gotou, K. Ueno, and H. Shirai, Jpn. J. Appl. Phys., Part 1 51, 10NE22 (2012)..

[15] NASA. [Online]. Available: http://solarsystem.nasa.gov/planets/ pro_le.cfm? Display=Facts&Object=Sun

[16] Standard Tables for Reference Solar Spectral Irradiances: Direct Normal and

Hemispherical on 37°Tilted Surface, American Society for Testing and Materials (ASTM) Std. G173 - 03 (2008), 2008.
[17] G. P. Smestad, F. C. Krebs, C. M. Lampert, C. G. Granqvist, K. Chopra, X. Mathew, and H. Takakura, Solar Energy Materials and Solar Cells, vol. 92, pp. 371, 2008.
[18] J. Zhao, A. Wang, and M. A. Green, Progress in Photovoltaics: Research and Applications, vol. 7, pp. 471, 1999.
[19] D. Pysch, A. Mette, and S. Glunz, Solar Energy Materials and Solar Cells, vol. 91, pp. 1698, 2007.
[20] S. M. Sze, Physics of semiconductor devices, 1st ed. Wiley, New York, 1969.
[21] M. A. Green, Solar Cells: Operating Principles, Technology and Device Applications. Prentice Hall, Englewood Cliffs, NJ., 1982.
[22] M. Green, Electron Devices, IEEE Transactions on, vol. 31, pp. 671, 1984.
[23] C.-T. Sah, R. Noyce, and W. Shockley, Proceedings of the IRE, vol. 45, pp. 1228, 1957.
[24] O. Breitenstein, P. Altermatt, K. Ramspeck, M. Green, J. Zhao, and A. Schenk, "Interpretation of the commonly observed I-V characteristics of c-Si cells having ideality factor larger than two," in Photovoltaic Energy Conversion, Conference Record of the 2006 IEEE 4th World Conference on, vol. 1, 2006, pp. 879.
[25] A. S. H. van der Heide, A. Schnecker, J. H. Bultman, and W. C. Sinke, Progress in Photovoltaics: Research and Applications, vol. 13, pp. 3,2005.
[26] Y. Tsunomura, Y. Yoshimine, M. Taguchi, T. Baba, T. Kinoshita, H. Kanno, H. Sakata, E. Maruyama, and M. Tanaka, Sol. Energy Mater. Sol. Cells 93, 670 (2009).
[27] Q. Wang, M. R. Page, E. Iwanicko, Y. Xu, L. Royabal, R. Bauer, B. To, H. -C. Yuan, A. Duda, F. Hasioon, Y. F. Yan, D. Levi, D. Meier, H. M. Branz, and T. H. Wang, Appl. Phys. Lett. 96, 013507 (2010).
[28] M. Ono, Z. Tang, R. Ishikawa, T. Gotou, K. Ueno, and H. Shirai, Appl. Phys. Express 50, 032301 (2012).
[29] T. Ino, M. Ono, N. Miyauchi, Q. Liu, Z. Tang, R. Ishikawa, K. Ueno, and H. Shirai, Jpn. J. Appl. Phys. 51, 061602 (2012).
[30] D. J. Lipomi, J. A. Lee, M. Vosgueritchian, B. C.-K. Tee, J. Bolander, and Z. Bao, Chem. Mater. 25, 373 (2012).
[31] M. Vosgueritchian, D. J. Lipomi, and Z. Bao, Adv. Funct. Mater. 22, 421 (2012).
[32] T. Unold, M. Ro ̈sch, and G. H. Bauer, J. Non-Cryst. Solids 266–269, 1033 (2000).
[33] S. Avasthi, S. Lee, Y.-L. Loo, and J. C. Sturm, Adc. Mater. 23, 5672 (201).
[34] S. M. Sze, Physics of Semiconductor Device (Wiley, New York, 1969), p. 643.
[35] L. A. A. Pettersson, F. Carlsson, O. Ingana ̈s, and H. Arwin, Thin Solid Films 313–314, 356 (1998).

[36] X. Shen, B. Sun, D. Liu, and S.-T. Lee, J. Am. Chem. Soc. 133, 19408 (2011).
[37] F. Zhang, B. Sun, T. Song, X. Zhu, and S. Lee, Chem. Mater. 23, 2084 (2011).
[38] X. Shen, B. Sun, F. Yan, J. Zhao, F. Zhang, S. Wang, X. Zhu, and S. Lee, ACS Nano 4, 5869 (2010).
[39] L. He, C. Jiang, H. Wang, D. Lai, and Rusli, Appl. Phys. Lett. 100, 073503 (2012).
[40] A. Elschner, S. Kirchmeyer, W. L€ovenich, U. Merker, and K. Reuter, PEDOT - Principle and Applications of an Intrinsically Conductive Polymer (CRC Press/Taylor and Francis Group, New York, 2011).
[41] Y. Xia and J. Ouyang, J. Mater. Chem. 21, 4927 (2011).
[42] F. Jonas and G. Heywang, Electrochim. Acta 39, 1345 (1994).
[43] D. P. Asberg and O. Inagan€as, Synth. Met. 137, 1403 (2003).
[44] B. L. Groenendaal, F. Jonas, D. Freitag, H. Pielartzik, and J. R. Reynolds, Adv. Mater. 12, 481 (2000).
[45] M. Ono, Z. Tang, R. Ishikawa, T. Gotou, K. Ueno, and H. Shirai, Appl. Phys. Express 5, 032301 (2012).
[46] Y.-J. Lin and Y.-C. Su, J. Appl. Phys. 111, 073712 (2012).
[47] B. Yin, Q. Liu, L. Yang, X. Wu, Z. Liu, Y. Hua, S. Yin, and Y. Chen, J. Nanosci. Nanotechnol. 10, 1934 (2010).
[48] T. J. Wang, Y. Q. Qi, J. K. Xu, X. J. Hu, and P. Chen, Appl. Surf. Sci. 250, 188 (2005).
[49] X. Crispin, S. Marciniak, W. Osikowicz, G. Zotti, A. W. D. Van Der Gon, F. Louwet, M. Fahlman, L. Groenendaal, F. D. Schryver, and W. R. Salaneck, J. Polym. Sci. B, Polym. Phys. 41, 2561 (2003).
[50] M. Yamashita, C. Otani, M. Shimizu, and H. Okuzaki, Appl. Phys. Lett. 99, 143307 (2011).
[51] L. A. A. Pettersson, F. Carlsson, O. Ingan€as, and H. Arwin, Thin Solid Films 313–314, 356 (1998).
[52] L. A. A. Pettersson, S. Ghosh, and O. Ingan€as, Org. Electron. 3, 143 (2002).
[53] Q. Liu, M. Ono, Z. Tang, R. Ishikawa, K. Uneo, and H. Shirai, Appl. Phys. Lett. 100, 183901 (2012).
[54] L. He, C. Jiang, H. Wang, D. Lai, and Rusli, Appl. Phys. Lett. 100, 073503 (2012).
[55] W. G. Haines and R. H. Bube, J. Appl. Phys. 49, 304 (1978).
[56] E. Kauer, Philips Tech. Rev. 26, 33 (1965).
[57] K. E. Aasmundtveit, E. J. Samuelsen, L. A. A. Pettersson, O. Ingan€as, T. Johansson, and R. Feidenhans'l, Synth. Met. 101, 561 (1999).
[58] H. Okuzaki, Y. Harashina, and H. Yan, Eur. Polym. J. 45, 256 (2009).
[59] X. Crispin, F. L. E. Jakobsson, A. Crispin, P. C. M. Grim, P. Andersson, A.

Volodin, C. van Haesendonck, M. Van der Auweraer, W. R. Salaneck, and M. Berggren, Chem. Mater. 18, 4354 (2006).
[60] H. Fujiwara and M. Kondo, Phys. Rev. B 71, 075109 (2005).
[61] E. Shanthi, V. Dutta, A. Banerjee, and K. L. Chopra, J. Appl. Phys. 51, 6243 (1980).
[62] N. S. Lewis, Science 315, 798 (2007).
[63] A. G. Pattantyus-Abraham, I. J. Kramer, A. R. Barkhouse, X. Wang, G. Konstantatos, R. Debanth, L. Levina, I. Raabe, M. K. Nazeeeruddin, M. Gratzel, and E. H. Sargent, ACS Nano 4, 3374 (2010).
[64] I. Gur, N. A. Fromer, M. L. Geier, A. P. Alivisatos, Science 310, 462 (2005).
[65] B. Tian, X. Zheng, T. J. Kempa. Y. Fang, N. Yu, G. Yu, J. Huang, and C. M. Lieber, Nature 449, 885 (2007).
[66] V. Sivakaov, G. Andra, A. Gawlik, A. Berger, J. Plentz, F. Falk, and S. H. Christiansen, Nano Lett. 9, 1549 (2009).
[66] S. W. Boettcher, J. M. Spurgeon, M. C. Putnam, E. L. Warren, D. B. Turner-Evans, M. D. Kelzenberg, J. R. Maiolo, H. A. Atwater, and N. S. Lewis, Science 327, 185 (2010).
[67] Y. B. Tang, Z. H. Chen, H. S. Song, C. S. Lee, H. T. Cong, H. M. Cheng, W. J. Zhang, I. Bello, and S. T. Lee, Nano Lett. 8, 4191 (2008).
[68] W. Wei, X.-Y. Bao, C. Soci, Y. Ding, Z.-L. Wang, and D. Wang, Nano Lett. 9, 2926 (2009).
[69] M. B. Tzolov, T.-F. Kuo, D. A. Straus, A. Yin, and J. Xu, J. Phys. Chem. C 111, 5800 (2007).
[70] J.-H. Lin, J.-J. Zeng, Y.-C. Su, and Y.-J. Lin, Appl. Phys. Lett. 100, 153509 (2012).
[71] Y.-J. Lin and Y.-C. Su, J. Appl. Phys. 111, 073712 (2012).
[72] B. Yin, Q. Liu, X. Wu, Z. Liu. Y. Hua, S. Yin, and Y. Chen, J. Nanosci. Nanotechnol. 10, 1934 (2010).
[73] I. Khatri, Q. Liu, R. Ishikawa, K. Ueno, and H. Shirai, Phys. Status Solidi C 9, 2134–2137 (2012).
[74] S. Kato, R. Ishikawa, Y. Kubo, H. Shirai, and K. Ueno, Jpn. J. Appl. Phys., Part 1 50, 071604 (2011).
[75] Q. Liu, F. Watanabe, A. Hoshino, R. Ishikawa, T. Gotou, K. Ueno, and H. Shirai, Jpn. J. Appl. Phys., Part 1 51, 10NE22 (2012).
[76] L. He, C. Jiang, H. Wang, D. Lai, and Rusli, Appl. Phys. Lett. 100, 073503 (2012).
[77] Q. Liu, H. Ono, Z. Tang, R. Ishikawa, K. Ueno, and H. Shirai, Appl. Phys. Lett. 100, 183901 (2012).
[78] B. Hoex, J. J. H. Gielis, M. C. M. van de Sanden, and W. M. M. Kessels, J. Appl.

Phys. 104, 113703 (2008).
[79] B. Hoex, J. J. H. Gielis, M. C. M. van de Sanden, and W. M. M. Kessels, Appl. Phys. Lett. 89, 042112 (2006).
[80] A. S. Erickson, N. K. Kedem, A. E. Haji-Yahia, and D. Cahen, Appl. Phys. Lett. 101, 233901 (2012).
[81] T. A. Kerr, H. Wu, and L. F. Nazar, Chem Mater. 8, 2005 (1996).
[82] A. M. Nardes, M. Kemerink, R. A. J. Janssen, J. A. M. Bastiaansen, N. M. M. Kiggen, B. M. W. Langeveld, A. J. J. M. van Breemen, and M. M. De Kok, Adv. Mater. 19, 1196 (2007).
[83] J.Maeng,M. Jo, S. J. Kang,M.K.Kwon,G. Jo, T.W.Kim, J. Seo,H. Hwang, D. Y. Kim, S. J. Park, and T. Lee, Appl. Phys. Lett. 93, 123109 (2008).
[84] M. Yamashita, C. Otani, M. Shimizu, and H. Okuzaki, Appl. Phys. Lett. 99, 143307 (2011).
[85] Q. Liu, I. Khatri, R. Ishikawa, K. Ueno, and H. Shirai, Appl. Phys. Lett. 102, 183503 (2013).
[86] Y. B. Tang, Z. H. Chen, H. S. Song, C. S. Lee, H. T. Cong, H. M. Cheng, W. J. Zhang, I. Bello, and S. T. Lee, Nano Lett. 8, 4191 (2008).
[87] W. Wei, X.-Y. Bao, C. Soci, Y. Ding, Z.-L. Wang, and D. Wang, Nano Lett. 9, 2926 (2009).
[88] M. B. Tzolov, T.-F. Kuo, D. A. Straus, A. Yin, and J. Xu, J. Phys. Chem. C 111, 5800 (2007).
[89] Y.-J. Lin and Y.-C. Su, J. Appl. Phys. 111, 073712 (2012).
[90] X. Miao, S. Tongay, M. K. Petterson, K. Berke, A. G. Rinzler, B. R. Appleton, and A. F. Hebard, Nano Lett. 12, 2745 (2012).
[91] Q. Liu, T. Imamura, T. Hiate, I. Khatri, Z. Tang, R. Ishikawa, K. Ueno, and H. Shirai, Appl. Phys. Lett. 102, 243902 (2013).
[92] L. He, C. Jiang, H. Wang, D. Lai, and Rusil, Appl. Phys. Lett. 100, 073503 (2012).
[93] Q. Liu, Z. Tang, R. Ishikawa, K. Ueno, and H. Shirai, Appl. Phys. Lett. 100, 183901 (2012).
[94] M. Pietsch, M. Bashouti, and S. Christiansen, J. Phys. Chem. C 117, 9049 (2013).
[95] Q. Liu, I. Khatri, R. Ishikawa, K. Ueno, and H. Shirai, Appl. Phys. Lett. 102, 183503 (2013).
[96] S. Avasthi, S. Lee, Y.-L. Leo, and J. C. Sturm, Adv. Mater. 23, 572 (2011).
[97] Z. Tang, Q. Liu, I. Khatri, R. Ishikawa, K. Ueno, and H. Shirai, Phys. Status Solidi 9, 2134 (2012).
[98] Y. Zhu, T. Song, F. Zhang, S.-T. Lee, and B. Sun, Appl. Phys. Lett. 102, 113504 (2013).

[99] M. Tanaka, M. Taguchi, T. Matsuyama, T. Sawada, S. Tsuda, S. Nakano, H. Hanafusa, and Y. Kuwano, Jpn. J. Appl. Phys., Part 1 31, 3518 (1992).
[100] Y. Tsunomura, Y. Yoshimine, M. Taguchi, T. Baba, T. Kinoshita, H. Kanno, H. Sakata, E. Maruyama, and M. Tanaka, Sol. Energy Mater. Sol. Cells 93, 670 (2009).
[101] Y. Yuan, T. J. Reece, P. Sharma, S. Poddar, S. Ducharme, A. Gruverman, Y. Yang, and J. Huang, Nature Mater. 10, 296 (2011).
[102] Y. Yuan, P. Sharma, Z. Xiao, S. Poddar, A. Gruverman, S. Ducharme, and J. Huang, Energy Environ. Sci. 5, 8558 (2012).
[103] A. V. Bune, V. M. Fridkin, S. Ducharme, L. M. Blinov, S. P. Palto, A. V. Sorokin, S. G. Yudin, and A. Zlatkin, Nature 391, 874 (1998).
[104] K. Tashiro and M. Kobayashi, Polym. Prep. Jpn. 38, 1004 (1989).
[105] K. Tashiro and M. Kobayashi, Phase Transitions 18, 213 (1989).
[106] "New conducting and semiconducting polymers for plastic electronics," DuPont, Tech. Rep., 2011. [Online]. Available: http://dupont.t2h.yet2.com/t2h/page/techpak?id=47662&sid=20
[107] "New conducting and semiconducting polymers for plastic electronics," Du Pont, Tech. Rep., 2011. [Online]. Available: http://www2.dupont.com/Di_use_Light_Reectors/en_US/assets/downloads/ NOW801 AR Sell Sheet me05-21.pdf
[108] M. Tao, W. Zhou, H. Yang, and L. Chen, Applied Physics Letters, vol. 91, p. 081118, 2007.
[109] K. Forberich, G. Dennler, M. C. Scharber, K. Hingerl, T. Fromherz and C. J. Brabec, Thin Solid Films, vol. 516, pp. 7167, 2008, proceedings on Advanced Materials and Concepts for Photovoltaics EMRS 2007 Conference, Strasbourg, France.
[110] D. King and M. Buck, "Experimental optimization of an anisotropic etchingprocess for random texturization of silicon solar cells," in Photovoltaic Specialists Conference, 1991., Conference Record of the Twenty Second IEEE, oct 1991, pp. 303, vol.1.
[111] T. Minami, H. Nanto, and S. Takata, Japanese Journal of Applied Physics, vol. 23, no. Part 2, pp. L280, 1984.
[112] T. Kuwabara, Y. Kawahara, T. Yamaguchi, and K. Takahashi, ACS Applied Materials & Interfaces, vol. 1, pp. 2107, 2009, pMID: 20355841.
[113] J.-C. Wang, W.-T. Weng, M.-Y. Tsai, M.-K. Lee, S.-F. Horng, T.-P. Perng, C.-C. Kei, C.-C. Yu, and H.-F. Meng, J. Mater. Chem., vol. 20, pp. 862, 2010.
[114] J.-W. Kim, J. Choi, S.-J. Hong, J.-I. Han, and Y.-S. Kim, Journal of Korean Physical Society, vol. 57, p. 1794, Dec. 2010.
[115] J.-Y. Lee, S. T. Connor, Y. Cui, and P. Peumans, Nano Letters, vol. 8, pp. 689, 2008.

[116] J. Yeo, J. Yu, D. Kim, S. Kim, S. Na, Solar Energy Materials & Solar Cells, vol. 114, p. 104, 2013
[117] Michael Vosgueritchian, Darren J. Lipomi, Zhenan Bao, Advanced Functional Materials, 22 (2012) 421
[118] A.M. Nardes, M. Kemerink, M.M. de Kok, E. Vinken, K. Maturova, J. Janssen, Organic Electronics, 9 (2008) 727–734
[119] L. Bert Groenendaal, Friedrich Jonas, Dieter Freitag, Harald Pielartzik, and John R. Reynolds, Adv. Mate. 12 (2000) 481
[120] S. K. M. Jo ̈nsson et al. Synth. Met. 139 (2003) 1.
[121] B. Yin et al.: J. Nanosci. Nanotechnol. 10 (2010) 1934.
[122] S.-I. Na et al.: J. Mater. Chem. 19 (2009) 9045.
[123] Werner Kern, RCA Critical Cleaning Process
[124] J.N. Hilfiker, R.A. Synowicki, H.G. Tompkins, 51st Annual Technical Conference Proceedings, Chicago, IL, April 19–24, 2008 ISSN: 0737-5921
[125] [Online]. Available: http://www.jawoollam.com/tutorial_1.html
[126] Hiroyuki Fujiwara, Spectroscopic Ellipsometry: Principles and
Application s, Weily, March 20, 2007
[127] [Online]. Available: http://www.nanoscience.com/education/afm.html
[128] S.R. Wenham, M.A. Green, M.E. Watt, R. Corkish, APPLIED PHOTOVOLTAICS (Second Edition)
[129] Antonio Luque, Steven Hegedus, Handbook of Photovoltaic Science and Engineering, John Wiley & Sons Ltd, 2003
[130] Park, S.; Cho, E.; Song, D.; Conibeer, G.; Green, M.A. Energy Mater. Sol. Cells 2009, 93, 684-690.
[131] Sze, S. M.; Ng, K. K. Physics of Semiconductor Devices, John Wiley & Sons, Inc. 2007, P81.
[132] Miao, X.; Tongay, S.; Petterson, M.K.; Berke, K.; Rinzler, A.G.; Appleton, B. R.; Hebard, A.F. Nano Lett., 2012, 12, 2745–2750.
* Special notice that Introduction and Appendix parts referred following PhD dissertation: Z. Tang, “Optical and carrier transport properties of Graphene Oxide based crystalline-Si/PEDOT:PSS heterojunction solar cells”, 2013 and S. Avasthi, “Crystalline-Si/Organic Heterojunction for Solar Photovoltaics”, 2011.